

Utah State University

DigitalCommons@USU

All Graduate Theses and Dissertations

Graduate Studies

12-2017

Water Surface Impact and Ricochet of Deformable Elastomeric Spheres

Randy Craig Hurd
Utah State University

Follow this and additional works at: <https://digitalcommons.usu.edu/etd>



Part of the [Mechanical Engineering Commons](#)

Recommended Citation

Hurd, Randy Craig, "Water Surface Impact and Ricochet of Deformable Elastomeric Spheres" (2017). *All Graduate Theses and Dissertations*. 6893.

<https://digitalcommons.usu.edu/etd/6893>

This Dissertation is brought to you for free and open access by the Graduate Studies at DigitalCommons@USU. It has been accepted for inclusion in All Graduate Theses and Dissertations by an authorized administrator of DigitalCommons@USU. For more information, please contact digitalcommons@usu.edu.



WATER SURFACE IMPACT AND RICOCHET OF DEFORMABLE

ELASTOMERIC SPHERES

by

Randy C. Hurd

A dissertation submitted in partial fulfillment
of the requirements for the degree

of

DOCTOR OF PHILOSOPHY

in

Mechanical Engineering

Approved:

Tadd Truscott, Ph.D.
Major Professor

Barton Smith, Ph.D.
Committee Member

Ryan Berke, Ph.D.
Committee Member

Robert Spall, Ph.D.
Committee Member

Jesse Belden, Ph.D.
Committee Member

David Peak, Ph.D.
Committee Member

Mark R. McLellan, Ph.D.
Vice President for Research and
Dean of the School of Graduate Studies

UTAH STATE UNIVERSITY
Logan, Utah

2017

Copyright © Randy Craig Hurd 2017

All Rights Reserved

ABSTRACT

Water surface impact and ricochet of
deformable elastomeric spheres

by

Randy Craig Hurd, Doctor of Philosophy

Utah State University, 2017

Major Professor: Tadd T. Truscott, PhD
Department: Mechanical and Aerospace Engineering

Elastomeric silicone rubber spheres ricochet from a water surface when rigid spheres and disks (or skipping stones) cannot. This dissertation investigates why these objects are able to skip so successfully. High speed cameras allow us to see that these unique spheres deform significantly as they impact the water surface, flattening into oblate shapes with greater cross-sectional area. Though the water entry behavior of deformable spheres deviates from that of rigid spheres, our research shows that if this deformation is accounted for, their behavior can be predicted from previously established methods. Soft spheres skip more easily because they deform significantly when impacting the water surface. We present a regime diagram which enables the prediction ricochet from sphere impact conditions. Experiments and mathematical models of the sphere skipping both show that these deformable spheres skip more readily because deformation momentarily increases cross-sectional area and produces an attack angle with the water which is favorable to skipping. Predictions from our mathematical model agree strongly with observations from experiments. Even when a sphere was allowed to skip multiple times in the laboratory, the mathematical model showed good agreement with measured impact conditions through subsequent skipping events. While studying multiple impact events in an outdoor setting, we discovered a

previously unidentified means of skipping, which is unique to deformable spheres. This new skipping occurs when a relatively soft sphere hits the water at a high speed and low impact angle and the sphere begins to rotate very quickly. This large angular velocity causes the sphere to stretch into and maintain a disk-like shape with an oval cross section. The sphere is observed to move nearly parallel with the water surface with the tips of the major axis of the spheroid dipping into the water as it rotates with the sides passing just over the surface. This sequence of rapid impact events give the impression that the sphere is walking across the water surface.

(128 pages)

PUBLIC ABSTRACT

Water surface impact and ricochet of
deformable elastomeric spheres

Randy Craig Hurd

Soft and deformable silicone rubber spheres ricochet from a water surface when rigid spheres and disks (or skipping stones) cannot. This dissertation investigates why these objects are able to skip so successfully. High speed cameras allow us to see that these unique spheres deform significantly as they impact the water surface, flattening into pancake-like shapes with greater area. Though the water entry behavior of deformable spheres deviates from that of rigid spheres, our research shows that if this deformation is accounted for, their behavior can be predicted from previously established methods. Soft spheres skip more easily because they deform significantly when impacting the water surface. We present a diagram which enables the prediction of a ricochet from sphere impact conditions such as speed and angle. Experiments and mathematical representations of the sphere skipping both show that these deformable spheres skip more readily because deformation momentarily increases sphere area and produces an attack angle with the water which is favorable to skipping. Predictions from our mathematical representation of sphere skipping agree strongly with observations from experiments. Even when a sphere was allowed to skip multiple times in the laboratory, the mathematical predictions show good agreement with measured impact conditions through subsequent skipping events. While studying multiple impact events in an outdoor setting, we discovered a previously unidentified means of skipping, which is unique to deformable spheres. This new skipping occurs when a relatively soft sphere first hits the water at a high speed and low impact angle and the sphere begins to rotate very quickly. This quick rotation causes the sphere to stretch into a shape similar to an American football and maintain this shape while it spins. The sphere

is observed to move nearly parallel with the water surface with the tips of this “football” dipping into the water as it rotates and the sides passing just over the surface. This sequence of rapid impact events give the impression that the sphere is walking across the water surface.

To my favorite teachers.

William Bird
Dean Hurd
Julie Brett
Katherine Oyler
Eugene Clark
Tadd Truscott
Jesse Belden

ACKNOWLEDGMENTS

Tadd Truscott has been an incredible inspiration, mentor and friend during this grueling and thrilling process. It is because of his passion that I decided to take this path and he has supported me every step of the way. Jesse Belden was a tremendous help and resource during my graduate education. I would not have been able to come this far without his patience and mentorship.

It is said that it takes a village to raise a child, and I feel the same is true of an education. So many great teachers and mentors have helped and encouraged me in pursuing this goal. I must acknowledge my friend and mentor Bruce Roundy, whose example and counsel helped me to choose this educational path. I have experienced tremendous help and support from students and instructors at Utah State University, members of the Splash Lab and from scientists and engineers at the Naval Undersea Warfare Center in Newport, Rhode Island. I am also tremendously grateful for Maria Medeiros and the Naval Undersea Research Program for their confidence and funding for this research.

Randy C. Hurd

CONTENTS

	Page
ABSTRACT	iii
PUBLIC ABSTRACT	v
ACKNOWLEDGMENTS	viii
LIST OF TABLES	xi
LIST OF FIGURES	xii
1 INTRODUCTION	1
1.1 Background	2
1.2 Summary	7
2 WATER ENTRY OF DEFORMABLE SPHERES	12
2.1 Prologue	12
2.2 Abstract	12
2.3 Introduction	13
2.4 Methods	15
2.5 Results	16
2.6 Conclusion	28
2.7 Supplement 1: Viscoelastic model	29
2.7.1 Describing the sphere deformation	29
2.7.2 Material model theory	30
2.7.3 Dynamics	32
2.7.4 Material model calibration	34
2.8 Supplement 2: Added mass	38
2.9 Acknowledgements	38
3 ELASTIC SPHERES CAN WALK ON WATER	43
3.1 Prologue	43
3.2 Abstract	43
3.3 Results	45
3.3.1 Elastic sphere skipping phenomena	45
3.3.2 Sphere deformation modes	46
3.3.3 Skip-enhancing mechanisms	46
3.3.4 Skipping regimes	52
3.3.5 Skipping sphere rebound	56
3.4 Discussion	58
3.5 Methods	58
3.5.1 Sphere fabrication and material properties	61
3.5.2 Sphere skipping experiments and data processing	62

3.5.3	Abaqus numerical model	62
3.5.4	Analytical model of elastic sphere skipping	63
3.5.5	Scaling analysis	67
3.6	Supplement 1: Analytical model of elastic sphere skipping	67
3.7	Supplement 2: Typical values and scaling analysis	80
3.8	Supplement 3: Small stiffness limit in which surface tension is important.	83
3.9	Acknowledgements	83
4	WATER WALKING: A NEW MODE OF FREE SURFACE SKIPPING	89
4.1	Prologue	89
4.2	Abstract	89
4.3	Background	90
4.4	Methods	92
4.5	Results	93
4.5.1	Multiple skip phenomena	93
4.5.2	Modeling multiple skip events	96
4.5.3	Investigating water walking	101
4.6	Conclusion	104
4.7	Acknowledgements	105
5	CONCLUSIONS	109
	CURRICULUM VITAE	113

LIST OF TABLES

Table	Page
2.1 Summary of material properties for the silicone spheres studied	35

LIST OF FIGURES

Figure	Page
1.1 Diagram of skipping cannonballs from a 16th century naval text	3
1.2 Photographs of the “bouncing bomb” designed by Barnes Wallis	4
2.1 A photo comparison of the water entry of rigid and elastomeric spheres . .	14
2.2 Experimental setup for water entry experiment	17
2.3 Visualizing sphere deformation upon free surface impact	19
2.4 Scaling for sphere deformation and oscillation	21
2.5 Mosaic of experimental results with varying impact conditions	23
2.6 Scaling for time to pinch-off	24
2.7 Position and velocity of spheres during water entry	25
2.8 Cycle-averaged force coefficients for deformable spheres upon entry	27
2.9 Nominal deformation of the sphere into an axisymmetric ellipsoid	30
2.10 Visual representation of the 3-parameter Maxwell model	32
2.11 Results from sphere material testing on an Instron machine	36
2.12 Experimental results for an elastomeric sphere impacting a rigid surface . .	37
3.1 Elasticity alters sphere skipping dynamics	47
3.2 Fluid-structure coupling through sphere deformation modes	48
3.3 Description of sphere deformation during impact	51
3.4 The effect of material stiffness on skipping behaviour	53
3.5 Matryoshka cavities depend on two timescales	55
3.6 Classification of impact phenomena for single and multiple skip events . . .	57
3.7 Restitution coefficients of elastic spheres skipping on water	59

3.8	An elastic sphere experiences several modes in a multiple skip event	60
3.9	Elastic spheres skip at much larger impact angles than rigid spheres	80
3.10	The wave time is linked to the rate of change of attack angle	82
3.11	Limiting case when surface tension becomes important	84
4.1	Historical observation of water surface skipping	90
4.2	Traditional skipping compared to water walking	93
4.3	Diagram of experimental setup at Bear Lake	95
4.4	High speed images of traditional skipping and water walking	97
4.5	Representation of sphere skipping model	98
4.6	Measured and modeled acceleration upon impact	100
4.7	Visualizing multi-skip events in terms of impact conditions	101
4.8	Angular velocity and water walking	103
4.9	Water walking exhibits two types of skipping	104
4.10	Correlation between number of skips and distance travelled	105

CHAPTER 1

INTRODUCTION

*“The people along the sand
All turn and look one way.
They turn their back on the land.
They look at the sea all day...*

*The land may vary more;
But wherever the truth may be-
The water comes ashore,
And the people look at the sea...”*

-Robert Frost

Humans share a universal interest in coastline. Nearly as ubiquitous as this instinct to “look at the sea all day,” is the urge to toss something into it – or, better yet – to propel a smooth stone, sidearm, across the glassy surface.

Stone skipping surely predates recorded history; though it seems to have first appeared in the written record in the late 16th century, as a game called “duckes and drakes.” Soon after, people began to grasp its practical implications. As early as 1587, naval gunners began skipping cannonballs across the ocean surface [14]. A skipping cannonball simplified the task of targeting enemy ships by allowing a shot to engage any target along a straight line rather than only a single point. In more recent years, skipping projectiles have been used to great tactical effect. British engineer Barnes Wallis designed “bouncing bombs” to skip across the water surface, avoiding torpedo nets placed in front of strategic hydroelectric dams. These skipping projectiles enabled the breach of the Eder and Möhne dams in Germany in 1943 [6]. Water ricochet continues to be investigated in light of Naval application.

Most readers have likely skipped a flat stone across a still lake; likely fewer have had the

opportunity to skip a Waboba® across a water surface. The Waboba ball is an aquatic toy that consists of a homogeneous elastomeric sphere covered with a lycra cloth skin. The ball skips effortlessly across the water surface, requiring less attention to detail when compared to skipping stones.

This research addresses the water impact dynamics of soft, elastomeric silicone rubber spheres inspired by the Waboba ball. This work addresses how the water entry characteristics of elastomeric spheres differ from rigid spheres, and primarily, how elastomeric spheres skip more readily than their rigid counterparts. The results provide means for predicting and modeling the water entry and skipping behavior of highly deformable elastomeric spheres.

1.1 Background

Though it may be difficult for the reader to imagine a 25 kg cannon ball skimming across the ocean surface like a skipping stone, this practice was used for hundreds of years to increase the odds of engaging an enemy vessel. The first known reference to this practice comes from a book on naval gunnery published in 1578 entitled: *The Arte of Shooting in Great Ordaunce*. The author, William Bourne, provides some insight into this event sharing that, “looke by what proportion the shotte doth strike or hitte the ground or water, by that proportion the shotte shall rise againe, although that it flyeth not so farre in that proportion...” Bourne observes that a sphere impacting the water surface at an oblique angle will rebound at a similar angle, but loses velocity due to the impact event. Bourne’s text highlights that the distance between skips decreases with each impact event, and that skipping behavior is only observed at relatively low impact angles [5]. Though these observations are strictly qualitative, they provide the first-known recorded insight into water-skipping projectiles.

The practice of skipping cannonballs is mentioned in multiple military manuals during the 17th century, but descriptions of the event remain qualitative [9, 23]. The first experimental work on the subject appears in “Treatise on Naval Gunnery,” published in 1855. The book includes tables listing the number of skips recorded for several shot sizes fired

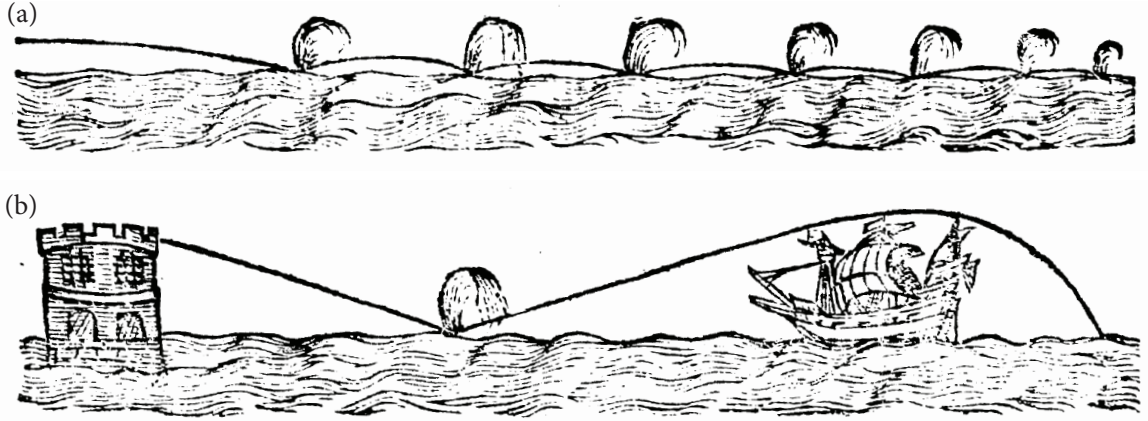


Fig. 1.1: Hand-drawn diagram of a skipping cannonball from the 1587 text, *The Arte of Shooting in Great Ordaunce*, by William Bourne. (a) Bourne states: “If you shoote any peece of Ordaunce towards the water, and lay the peece at the poynte blanke, and the peece be but little higher than the water, then shall the shotte runne grazing in this forme, to rise againe by that proportion that it doth hitte the water, and so to runne, till that the great force be decayed, as this example doth shew [5].” (b) A depiction of a shot glancing off the water surface to accompany Bourne’s description of using this method when targeting another ship.

with varying amounts of charge, showing that more powder tends to increase the number of skipping events [10]. Findings published in 1883 by de Jonquières first established a critical impact angle (above which ricochet will not occur), and established a correlation between this angle and the specific gravity (SG) of the projectile ($\theta_c = 18/\sqrt{SG}$). From this relationship he established that the critical skipping angle for steel spheres is approximately seven degrees [8]. When the British engineer Barnes Wallis began researching means for skipping large projectiles across the water surface, he mentioned that the sole piece of scientific information he possessed was that steel spheres can ricochet off the water at impact angles of seven degrees or less [14].

Perhaps the most well known implementation of skipping dynamics came during World War II when Barnes Wallis designed his famous “dam buster” or “bouncing bomb”. In 1943 these cylindrical bombs were dropped with high rates of backspin, enabling them to generate sufficient lift upon impact to skip across the water surface and avoid subsurface torpedo nets protecting dams. Upon reaching the dam, the charges sank until triggered by hydrostatic fuses. These bombs were employed by the British during the war to successfully breach both

the Möhne and Eder dams in Germany [6]. Images from testing can be seen in figure 1.2.

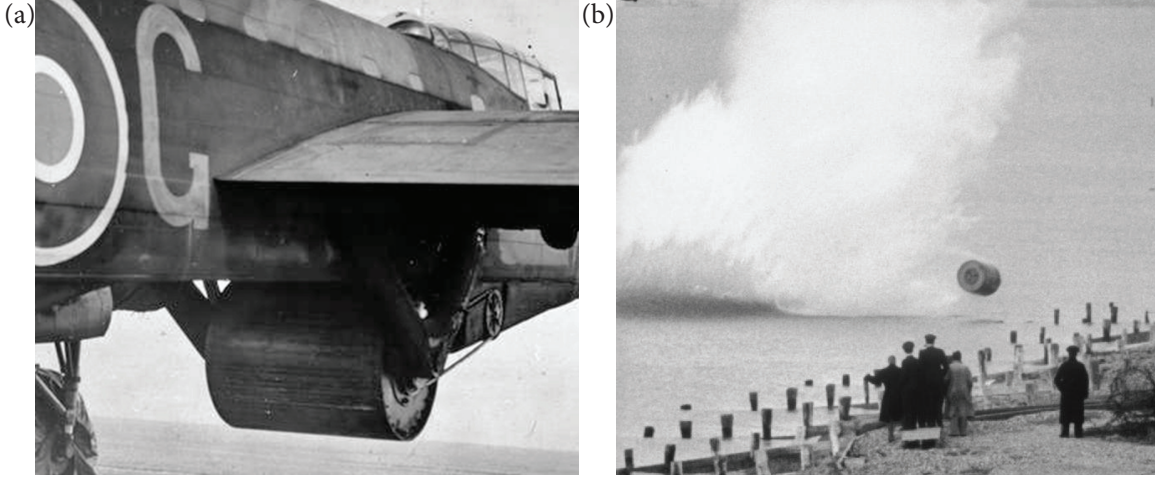


Fig. 1.2: (a) A 4200 kg “bouncing bomb” mounted under a Lancaster B III bombing plane. A mechanical chain runs to the mounting device to induce the backspin necessary for skipping. (b) Barnes Wallis and others watch from the shore as a “bouncing bomb” skips off the water surface.

The first analytical investigation of an oblique free surface impact appears to be Von Karman’s 1929 publication on the impact of seaplanes during landing. Von Karman developed a model for estimating the maximum fluid pressure generated during a landing as a function of impact velocity, impact angle and fluid density [28]. In the 1940s Birkhoff et al. and Richardson began to investigate the ricochet of rigid objects from a water surface. Birkhoff et al. developed a theoretical explanation for the dependence of the critical skipping angle on sphere specific gravity, but with many assumptions [3]. Richardson implemented high speed photography to study the skipping event and gather a great deal of experimental data. He made qualitative observations regarding the generated cavity and noted that the lift generated from the impact results in part from the slanted cavity walls [22].

In 1975 Johnson and Reid revisited the theoretical model established by Birkhoff et al. and compared it with experimental data. They established that Richardson’s experimental data, rough as it is by modern standards, supports the claims of Birkhoff et al. that $\theta_c = 18/\sqrt{SG}$. However, they pointed out that this expression does not express the minor,

yet noticeable, Froude number dependence of the critical skipping angle [16]. A year later in 1976, Hutchings also revisited Birkhoff’s model citing its over-simplified approach for predicting the pressure distribution on the impacting body. To remedy this, Hutchings used a pressure formula presented by Rayleigh which also expands this impact model to allow for rotation, which Barnes Wallis demonstrated is capable of enhancing lift force [13] [21] [15]. In the same year Soliman et al. performed an experimental study analyzing the critical impact angle of projectiles impacting water and sand. While their results support previous findings, they do show that critical skipping angle is not completely dependent on density ratio, but that there is some dependence on impact velocity and angular velocity, which merit further investigation [25]. Additionally, in 1982 Johnson et al. extended their own skipping research to cylindrical projectiles [17].

In 1991, Miloh and Shukron reexamined the free surface ricochet problem and numerically evaluated a more complex skipping model. They formulated Kelvin-Kirchoff-Lagrange equations of motion in terms of various time dependent added mass coefficients and their derivatives. These equations were then numerically integrated to estimate the trajectory of various sphere impact scenarios. Miloh and Shukron specifically investigated the Froude number dependence of the critical angle calculation and showed that $(\theta_c = 18/\sqrt{SG})$ represents a bounding asymptote as the Froude Number approaches infinity. This asymptote is generally a reasonable estimation as most skipping events only occur at relatively high Froude Numbers [18]. Nashida et al. showed that this critical angle formula also applies for granular material and represents an upper bound where projectile radius is significantly larger than particle radii. However, as these two values get closer, experimental results begin to deviate from this empirical model. [20]

More recently, skipping behavior has been studied in reference to skipping stones. In 2003, Bocquet presented a model for stone skipping which he used to theoretically estimate the maximum number of skips that can be achieved with a skipping stone [4]. Clanet *et al.* published an experimental investigation in 2004 which shows optimal values for both impact angle and attack angle [7]. The model for stone skipping was refined in light of

experimental results by Rosellini *et al.* [24]. In 2005 Nagahiro and Hayakawa performed a three-dimensional simulation of stone skipping which produced results in agreement with those discovered by Clanet *et al.* [19].

In 2012 Truscott *et al.* investigated the skipping dynamics of highly deformable elastomeric spheres, which are marketed as an easy-to-skip aquatic toy under the brand name Waboba [27]. Their data showed that these highly deformable spheres skip more readily and with less attention to impact conditions than is required for traditional stone skipping. Because an elastomeric spheres deforms rapidly in a direction corresponding to its trajectory, the feat of skipping becomes orientation independent and does not require angular velocity for gyroscopic stabilization. Impact velocity and impact angle thus become the key parameters in predicting free surface rebound [26]. In 2013 Belden *et. al* provided a more detailed investigation into the skipping mechanisms and pointed out the dependence on relative timescales for skip success. They also mentioned the need to more accurately determine the scaling for these critical timescales [2].

Under the mentorship of Dr. Tadd Truscott and Dr. Jesse Belden, I conducted a large-scale experimental study concerning the water skipping characteristics of elastomeric spheres. This work deviated from previous research in that it employed custom-made silicone rubber spheres rather than commercially available Waboba balls, allowing me to more carefully control size and material properties. The experiment was very large in scale, involving over 1,000 experimental runs, spanning a large range of material shear modulus, sphere diameter, impact velocity and impact angle. The results of this data set, a detailed description of the experimental methods, as well as a preliminary analytical model were published as my Master’s Thesis at Brigham Young University [11]. The results show that spheres skip more readily with lower values of shear modulus, and when impacting at higher velocities and smaller angles with the free surface. This work identified a helpful dimensionless number $G/\rho U^2$, where G is the material shear modulus, ρ is the liquid density and U is the impact velocity. This term, which is effectively a ratio of the material forces to the hydrodynamic forces on impact, provides an effective prediction of free surface ricochet

along with impact angle. The presented analytical model provided a favorable agreement for predicting the success and failure of skipping events.

1.2 Summary

All the research I have performed after my master's thesis is presented in this dissertation, which is organized in a multi-paper format divided into five chapters. To suit this format, bibliographies are found at the end of each chapter. This first chapter has summarized and discussed the history of scientific literature concerning water surface skipping. The purpose of this dissertation is to address and discuss the research objectives of this project, which are:

1. Understand the physics of the water surface skipping of elastomeric bodies.
2. Investigate how elasticity affects object-water energy transfer.
3. Understand the water entry characteristics of elastomeric bodies.
4. Understand how these principles transfer to successive skipping events.
5. Define optimal material properties and impact conditions for skipping.

In order to ensure that I was not neglecting any fundamental dynamics at the onset of my doctorate research, I studied the normal impact of elastomeric spheres with the free surface. My work shows that the deformation and oscillation resulting from this impact can be predicted. One might intuitively expect this deformation, and resulting increase in cross sectional area, to affect parameters such as sphere velocity, drag and time to cavity pinch-off. My research shows how these deviations may be predicted in light predicted sphere deformation and previous knowledge of water entry. The results from this study were published in *The Journal of Fluid Mechanics* and comprise Chapter 2 [12].

Upon further analysis of the data collected for my master's thesis, it was found that this data set was incomplete and required additional experimental tests to more accurately predict boundaries between impact types, as well as the minimal velocity necessary for

skipping. Additionally, I was curious if the trends observed would hold over subsequent impact events. Additional data were collected and analyzed, and the analytical model defined previously was updated in light of these new findings. These results are presented in Chapter 3 and were published in *Nature Communications* [1].

Finally, I wanted to study the skipping of elastomeric spheres in a more realistic setting where the sphere was able to skip indefinitely until losing the kinetic energy necessary for ricochet. Previously, this skipping behavior had been limited by lab space; as a result, this final experiment was performed outdoors along the coast of Bear Lake in Utah. This work shows that the skipping model provided previously, does accurately estimate impact conditions for multiple impact skipping events, and reasonably predicts number of skips and distance traveled, with some limitation. This work also introduced the existence of a previously undiscovered skipping mode in which the sphere travels nearly parallel to the water surface, striking the water rapidly. The findings from this study are presented in Chapter 4.

Chapter 5 summarizes the results from the studies presented in light of the project research objectives previously listed.

REFERENCES

- [1] J. Belden, R. C. Hurd, M. A. Jandron, A. F. Bower, and T. T. Truscott. Elastic spheres can walk on water. *Nature communications*, 7, 2016.
- [2] J. Belden, M. Jandron, and T. T. Truscott. Physics of elastic spheres skipping on water. *Physics of Sports*, 2013.
- [3] G. Birkhoff, G. D. Birkhoff, W. E. Bleik, E. H. Handler, F. D. Murnaghan, and T. L. Smith. Ricochet off water. *A.M.P. Memo*, (42.4M), 1944.
- [4] Lydéric Bocquet. The physics of stone skipping. *American journal of physics*, 71(2):150–155, 2003.
- [5] W. Bourne. *The Arte of Shooting in Great Ordnance*. Number 117. Theatrum Orbis Terrarum, 1969.
- [6] P. Brickhill. *The Dam Busters*. Ballantine Books, New York, NY, 1951.
- [7] C. Clanet, F. Hersen, and Bocquet L. Secrets of successful stone-skipping. *Nature*, 427:29, 2004.
- [8] E. de Jonquieres. On the ricochet of spherical projectiles on the surface of the water (translated to english). *Comptes Rendus*, 97:1278, 1883.
- [9] S. L. P. de Vauban. *Le directeur général des fortifications*. Chez Henri van Bulderen, marchand libraire, in de Pooten, à l’Enseigne de Mezeray, 1725.
- [10] H. Douglas. *Treatise on Naval Gunnery (1855)*. Naval & Military Press, 2003.
- [11] R. C. Hurd. On the free surface skipping characteristics of highly deformable elastic spheres. Master’s thesis, Brigham Young University, 2015.

- [12] R. C. Hurd, J. Belden, M. A. Jandron, D. T. Fanning, A. F. Bower, and T. T. Truscott. Water entry of deformable spheres. *Journal of Fluid Mechanics*, 824:912–930, 2017.
- [13] I. M. Hutchings. The ricochet of spheres and cylinders from the surface of water. *Int. J. Mech. Sci.*, 18:243–247, 1976.
- [14] W. Johnson. Ricochet of non-spinning projectiles, mainly from water. part i: some historical contributions. *Int. J. Impact Engng.*, 21:15–24, 1998.
- [15] W. Johnson. Ricochet of non-spinning projectiles, mainly from water. part ii:. *Int. J. Impact Engng.*, 21(1-2):25–34, 1998.
- [16] W. Johnson and S. R. Reid. Ricochet of spheres off water. *J. Mech. Engning. Science*, 17:71–81, 1975.
- [17] W. Johnson, A.K. Sengupta, and S.K. Ghosh. High velocity oblique impact and ricochet mainly of long rod projectiles: an overview. *Int. J. Mech. Sci.*, 24(7):425–436, 1982.
- [18] T. Miloh and Y. Shukron. Ricochet off water of spherical projectiles. *J. Ship Research*, 35:91–100, 1991.
- [19] S. Nagahiro and Y. Hayakawa. Theoretical and numerical approach to ”magic angle” of stone skipping. *Phys. Rev. Lett.*, 94:174501, May 2005.
- [20] M. Nishida, M. Okumura, and K. Tanaka. Effects of density ratio and diameter ratio on critical incident angles of projectiles impacting granular media. *Granular Matter*, (12):337–344, 2010.
- [21] Lord Rayleigh. On the resistance of fluids. *The Philosophical Magazine*, 2(13):430–441, 1876.
- [22] E. G. Richardson. The impact of a solid on a liquid surface. *Proc. Phys. Soc.*, 61:352–367, 1948.
- [23] E. Robins. *New principles of Gunnery*. 1742.

- [24] L. Rosellini, F. Hersen, C. Clanet, and L. Bocquet. Skipping stones. *J. Fluid Mechanics*, 543:137–146, 2004.
- [25] A. S. Soliman, S. R. Reid, and W. Johnson. The effect of spherical projectile speed in ricochet off water and sand. *Int. J. Mechanical Science*, 18:279–284, 1976.
- [26] T. T. Truscott, M. M. Wright, K. R. Langley, and J. Belden. Holy balls! balls that walk on water. *Phys. Fluids*, 24:091103, 2013.
- [27] J. Von Heland. Ball suitable for water games. Technical Report Publication Number. US7559862 B2. PCT Number. PCT/SE2005/000749., 2005.
- [28] T. Von Karman. The impact of seaplanes during landing. *NACA Tech Note*, (321), 1929.

CHAPTER 2

WATER ENTRY OF DEFORMABLE SPHERES

2.1 Prologue

In order to gain an increased understanding of the water impact behavior of elastomeric spheres, it seemed most logical to begin with the most fundamental form of the event, water entry perpendicular to the free surface. The data for this study were collected and processed at Utah State University. Analysis and modeling occurred at Utah State University and at the Naval Undersea Warfare Center in Newport, Rhode Island. The study was published in the Journal of Fluid Mechanics on 10 August 2017 under the title “The water entry of deformable spheres.” The authors listed are: Randy C. Hurd, Jesse Belden, Michael A. Jandron, D. Tate Fanning, Allan F. Bower and Tadd T. Truscott. The article in its entirety is presented below.

2.2 Abstract

When a rigid body collides with a liquid surface with sufficient velocity, it creates a splash curtain above the surface and entrains air behind the sphere, creating a cavity below the surface. While cavity dynamics have been studied for over a century, this work focuses on the water entry characteristics of deformable elastomeric spheres, which has not been studied. Upon free surface impact, elastomeric sphere deform significantly, resulting in large-scale material oscillations within the sphere, resulting in unique nested cavities. We study these phenomena experimentally with high speed imaging and image processing techniques. The water entry behavior of deformable spheres differs from rigid spheres because of the pronounced deformation caused at impact as well as the subsequent material vibration. Our results show that this deformation and vibration can be predicted from material properties and impact conditions. Additionally, by accounting for the sphere deformation in

an effective diameter term, we recover previously reported characteristics for time to cavity pinch-off and hydrodynamic force coefficients for rigid spheres. Our results also show that velocity change over the first oscillation period scales with a dimensionless ratio of material shear modulus to impact hydrodynamic pressure. Therefore we are able to describe the water entry characteristics of deformable spheres in terms of material properties and impact conditions.

2.3 Introduction

Water entry has been studied for over 100 years, with the earliest images taken by Worthington at the turn of the century [25], and much of the foundational work performed in the 1950s and 60s with military application in mind [16, 17, 19]. The topic of water entry is still of interest today with several significant research papers published in the last 20 years, investigating topics such as cavity physics, projectile dynamics and even ricochet off the water surface [2, 5, 11, 12, 20, 21], respectively.

Cavity characteristics vary with Froude Number, Bond Number, Capillary Number and by varying object geometry, rotation and wetting angle [21]. For example, low speed impact events with sufficiently small capillary numbers will not form subsurface cavities [12]. When a cavity forms it is often described by the manner in which the cavity collapses (or pinches-off). Cavities are categorized according to the depth at which pinch-off occurs, and these categories include: surface seal, deep seal, shallow seal and quasi-static seal [2, 3]. The results herein occur within the high Bond number parameter space ($Bo > 300$), where surface tension is negligible and only deep seal type pinch-off events have been observed. Previous studies provide theoretical predictions for pinch-off time and depth which produce good agreement with experiments employing steel spheres (high solid-liquid density ratio) where deceleration can be neglected. [4] revealed that a small mass ratio associated with a decelerating sphere can reduce the depth of pinch-off, but does not alter pinch-off time.

Beyond revealing scaling for pinch-off depth and time, several studies have explored the effect of unique impact conditions on cavity physics and body dynamics. Simply changing the geometry of the projectile generates a cavity with a cross-section resembling the outer

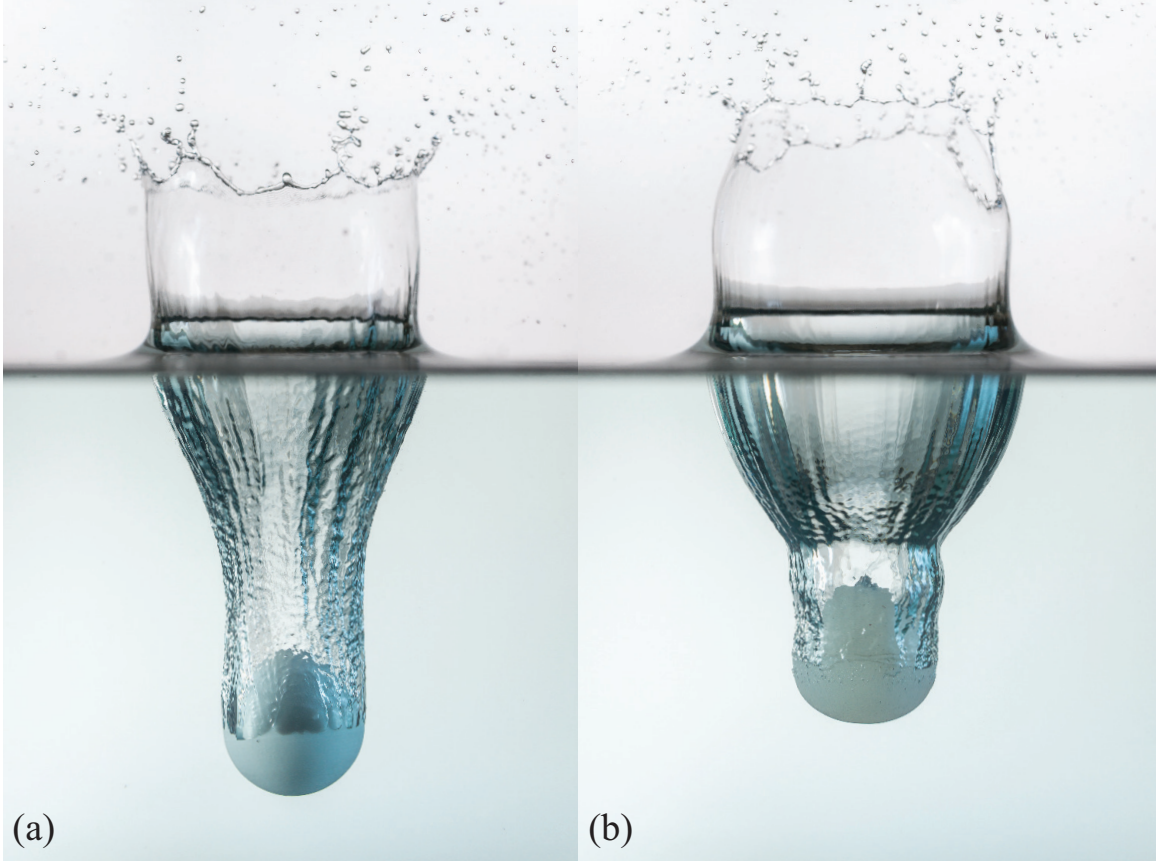


Fig. 2.1: Two spheres with shear moduli G_∞ differing by four orders of magnitude, experience very different water entry dynamics. (a) A rigid sphere ($G_\infty = 5.66 \times 10^5$ kPa), with a solid-liquid density ratio near unity, impacts the free surface forming a canonical subsurface cavity. (b) A deformable sphere ($G_\infty = 12.69$ kPa), with otherwise nearly identical properties and impact conditions as (a), forms an altered subsurface cavity due to relatively large deformations and material oscillation. Images were taken at the same time after impact. (Photo credit Chris Mabey.)

profile of the impacting body [13]. For slender-bodies it has been shown that even nose shape and entry angle can greatly alter cavity form and dynamics [7, 16]. Spinning the projectile perpendicular to the free surface prior to impact creates asymmetrical cavities and generates unbalanced forces [23]. Similar findings have resulted from covering half of a hydrophilic sphere with a hydrophobic coating [24]. Both of these methods generate asymmetrical cavities and cause the impacting body to veer from the primary axis of travel. Some groups have extended the work to biological organisms, for instance, [9] experimentally investigated plunge-diving birds using a simplified model. Their experiment involved an elastic beam attached to a rigid cone (representing the bird neck and head, respectively), and focused specifically on when buckling occurs as it relates to possible physical damage, as opposed to how significant deformations affect cavity shape and entry dynamics as discussed herein.

Recently, the authors investigated deformable spheres impacting a water surface at an oblique angle, primarily concerned with the effect of deformability on ricochet [5]. It was shown that induced vibrations interact with the cavity in unique ways resulting in nested cavities, but also inefficient skipping. However, we are not aware of any research addressing the normal entry behavior of deformable elastomeric spheres. Figure 2.1 presents two high resolution photographs which qualitatively display some of the differences between the water entry of rigid and highly deformable spheres, including differences in cavity shape and sphere deceleration. In this paper, we use an experimental approach to investigate the unique phenomena associated with water entry of highly deformable spheres.

2.4 Methods

We investigated the water entry characteristics of elastomeric spheres experimentally by varying sphere impact velocity U_0 , diameter D and material stiffness, as characterized by the neo-Hookean shear modulus G_∞ . Spheres were made from an incompressible platinum-cure silicone rubber called Dragon Skin[®], which is produced by Smooth-On, Inc. Shear modulus was varied by adding a silicone thinner to the mixture to produce three discrete values ($G_\infty = 1.12, 6.70$ & 70.2 kPa), which were determined by sphere compression tests (see Supplement 1). The constituents of the silicone rubber were measured by mass ratio,

mixed, then placed in a vacuum chamber to remove entrained air. Mixtures were poured into aluminum molds to form spheres with two different diameters ($D = 51$ & 100 mm). Spheres had a density of $\rho_s = 1070$ kg/m³, and the density of water is represented by ρ_w . The water entry of rigid spheres with identical $\rho_s = 1070$ kg/m³ were also investigated for comparison.

The experimental setup is summarized in Fig 2.2a. Spheres were dropped from three discrete heights (0.53, 1.53 & 2.27 m) into a 0.81×0.81 m² glass tank filled to ~ 1 m with water. The entry event was filmed using two Photron SA3 high speed cameras at 2000 frames per second with diffuse back lighting. The scalar λ represents the deviation of the deformed sphere from the initial diameter. Before splash curtain dome over, the changing diameter λD of the sphere was measured by fitting a circle (cyan) to the top view of the sphere as shown in figure 2.2(b). After dome over, λD was measured below the free surface (side view figure 2.2(c)). The lowest point of the sphere y_b (red cross figure 2.2(c)) was also measured directly from the images. The separation line at the air-water-sphere interface is marked by a green horizontal line. An ellipse was then fitted to the edge of the sphere below the separation line (yellow outline). Because the sphere deformation is assumed to be symmetric about the y -axis, measurements of λ from the side and top camera views are assumed to represent the same quantity.

2.5 Results

Figure 2.1 displays high resolution images of two spheres with nearly identical impact conditions ($U_0 = 2.4$ m/s, $D = 51$ mm), except that the sphere in (a) has shear modulus $G_\infty = 5.66 \times 10^5$ kPa (rigid) while the sphere in (b) has shear modulus $G_\infty = 12.7$ kPa. The cavity formed by the deformable projectile differs in the oscillatory profile of the cavity walls, in addition to being shallower and wider. Because the cavity physics and projectile dynamics are evidently different for a deformable sphere, characterizing the initial deformation and resulting material oscillation in the sphere is critical to understanding water entry physics for deformable objects.

Figure 2.3(a)&(b) lends additional insight into why a cavity produced by a deformable

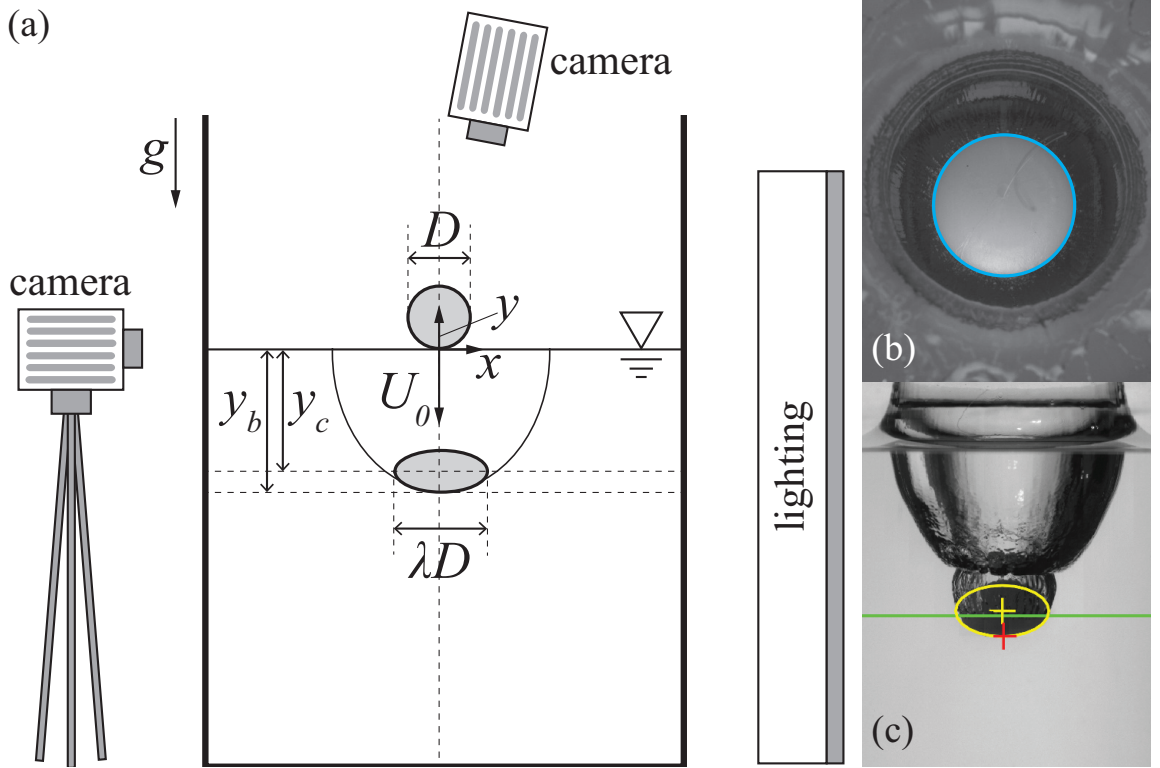


Fig. 2.2: (a) Spheres falling into a water-filled tank were filmed using high speed cameras and diffuse back lighting. The event is described by the parameters: sphere diameter D , impact velocity U_0 , a scalar defining sphere deformation λ , and the depth below the free surface of the sphere's lowest point y_b and the sphere center y_c . (b) Image processing was used to measure λD prior to dome over. (c) Image processing was used to locate y_b throughout the entry event (red cross). A curve was fitted to the edge of the sphere below the air-water-sphere interface (green line). A corresponding ellipsoid, with an assumed symmetry about the y -axis and a volume constrained by the undeformed sphere, was applied (yellow outline).

sphere deviates from that formed by a rigid sphere. At 12 ms after impact, the sphere has deformed significantly into an oblate spheroid, creating a wider cavity than a rigid sphere. Elastic forces cause the sphere to rebound from this initial deformation into a prolate spheroid with its major axis aligned with the vertical ($t = 29$ ms). The continually oscillating sphere now proceeds to a second radial expansion that penetrates through the cavity wall, forming a smaller cavity within the first ($t = 43$ ms), resulting in a so-called matryoshka cavity [5], [15]. For this case pinch-off occurs within the second cavity ($t = 96$ ms).

For each experimental test, the position of the bottom of the sphere y_b was tracked through a series of high speed images. In figure 2.3(c), y_b/D is plotted as a function of dimensionless time t/t_p (t_p : time to pinch-off), in which the sphere oscillation is evident. Figure 2.3(d) shows the measured value of λ , which reaches an initial large peak due to the impact event ($t = 12$ ms), and then decays throughout the water entry. This decay in λ is typical for all deformable sphere water entry events studied.

Figure 2.4(a) presents a simplified description of the sphere oscillation in which the sphere deforms into an oblate spheroid with symmetry about the y -axis. Here, λ represents the principal stretch in the x and z directions, and by conservation of volume the principal stretch in the y direction is $\lambda_y = 1/\lambda^2$. Defining λ in this way is based on the observation that the primary mode of deformation in the sphere during water entry is equi-biaxial tension, and λ is a measure of the principal stretch in the sphere. The parameter λ_{pN} represents the maximum stretch of the sphere in the x - z plane for the N^{th} deformation period.

Based on the decaying behaviour of λ during water entry, we aim to address if the source of damping is in the sphere material, water or both. First, we isolate the response of the sphere by performing a series of tests in which the spheres are dropped onto horizontal rigid surfaces (Supplement 1, figure 2.12). Impact with the rigid surface results in an initially large sphere deformation that decays in time. Based on these observations, we apply a viscoelastic model to the sphere material [6] as summarized in Supplement 1. The

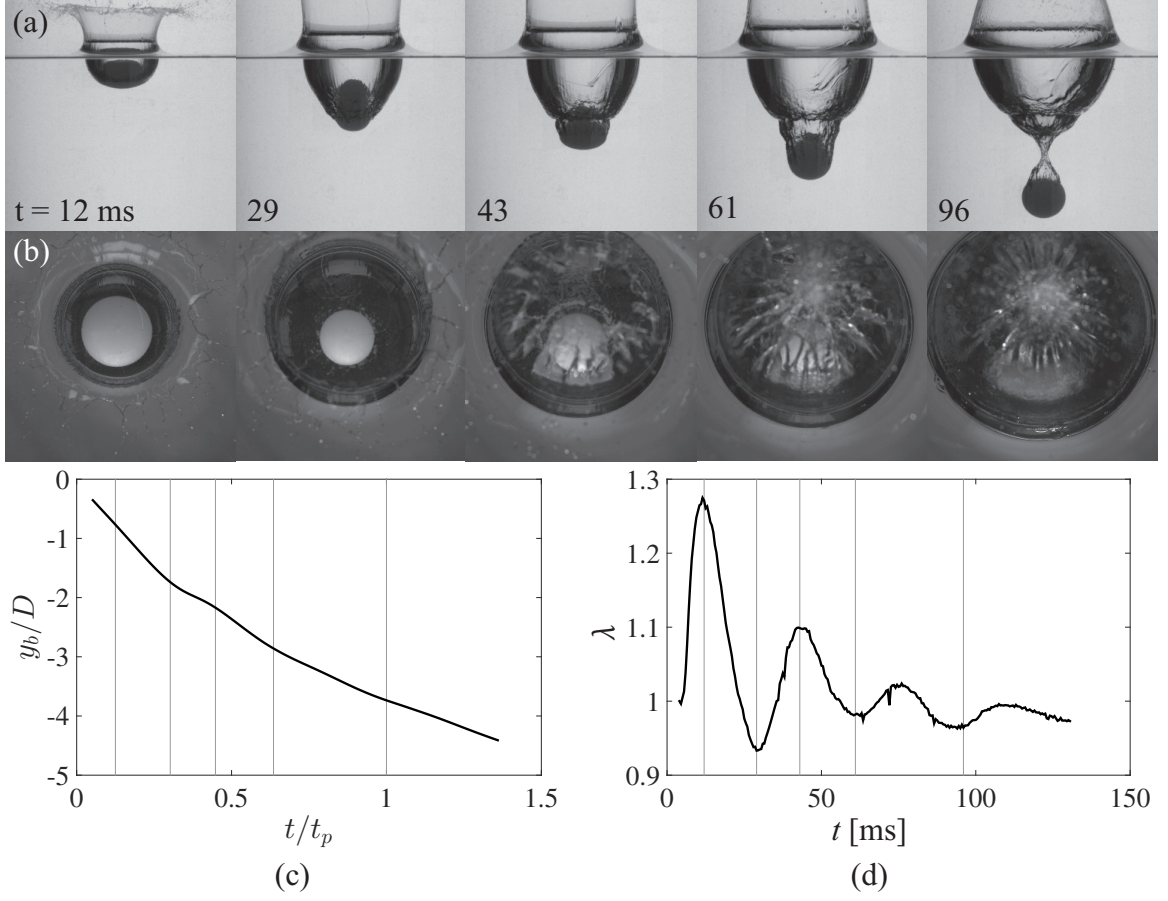


Fig. 2.3: (a) A sphere deforms significantly as it impacts and enters the water ($G_\infty = 6.70$ kPa, $D = 51$ mm and $U_0 = 5.3$ m/s); after the initial deformation the sphere oscillates between oblate and prolate shapes, creating a second cavity within the first. Pinch-off occurs within this second, smaller cavity ($t = 96$ ms). (b) The water entry event captured from a top view highlights the changing diameter and splash curtain dome over event. (c) The measured position of y_b is plotted against dimensionless time where vertical lines correspond to the images above. (d) Plotting the parameter λ as a function of time portrays a decaying sinusoid.

model includes parameters to account for viscous damping, but the equilibrium stress is still governed by the hyperelastic neo-Hookean model (parameterized by shear modulus G_∞). The rigid surface impact data is used to calibrate the dynamic parameters of the viscoelastic model. Second, to see if the damping in the material model can explain the decay observed in the water entry events, we construct a simplified model of the sphere oscillation (derived in Supplement 1). The sphere is prescribed an initial stretch $\lambda_0 = \lambda_{p1}$ at $t = t_0$ and allowed to oscillate freely for $t > t_0$. The analysis is performed for all experimental cases and the results are summarized in figure 2.4.

Figure 2.4(b) shows that the oscillation period predicted by the model is slightly less than that observed in the experiments. Because the viscoelastic model parameters were calibrated to an experimental test isolated from the water, we suggest the observed lower frequency (longer period) of the sphere in water is attributable to the added mass experienced by the sphere. Some mass of water has to be accelerated during portions of the sphere oscillation period (e.g., between $t = 3T/4$ and $t = 5T/4$ in figure 2.4(a)). However, if we scale the response in time by a ratio of experimental to modeled periods, $T_{\text{exp}}/T_{\text{model}}$, then the predicted oscillations show good agreement with the experiments. Despite the difference in period, the magnitude of the predicted peaks in λ are consistent with experiments (figure 2.4(c)&(d)), suggesting that the dominant source of damping is in fact in the sphere material. We note that the model agrees more accurately at the peaks than the valleys because an oscillating sphere complies with the idealization of the model (ellipsoidal assumption) more closely in its oblate shape than its prolate shape as is observed in figure 2.5(d).

Figure 2.5(a)-(d) show the cavity growth and pinch-off resulting from the impact of four spheres ($D = 51$ mm, $U_0 = 6.5$ m/s) with G_∞ decreasing from 5.66×10^5 kPa (a) to 1.12 kPa (d). The cavity in image sequence (b) is created by a sphere with a shear modulus of $G_\infty = 70.2$ kPa. The resulting cavity and pinch-off strongly resemble those created by the rigid sphere in (a), except for the presence of small-scale undulations on the cavity walls due to sphere vibration. The sphere in (c) has a shear modulus an order of magnitude smaller

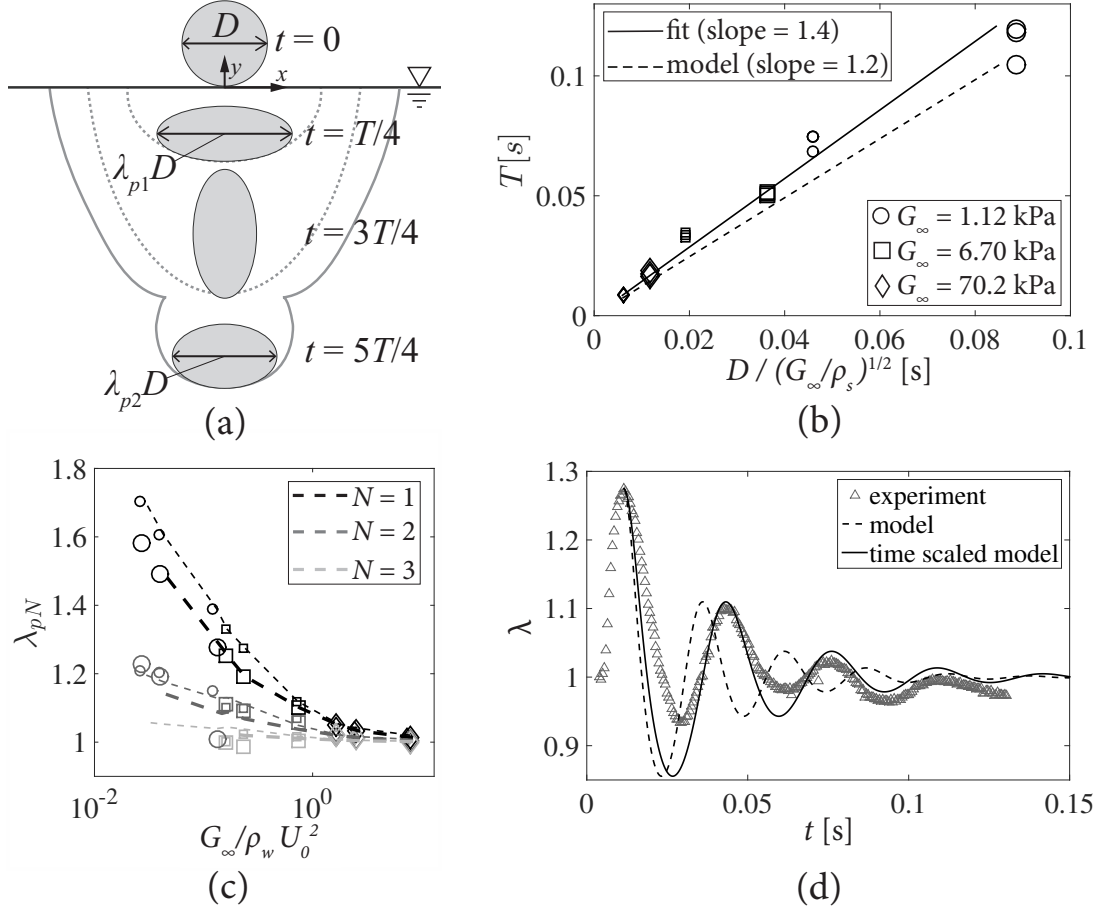


Fig. 2.4: (a) When a deformable sphere impacts the water surface it flattens into an oblate spheroid with an increased cross-sectional diameter at $t = T/4$ ($\lambda_{p1}D$) before rebounding back into a sphere at $T/2$. The sphere then forms a prolate spheroid at $3T/4$, then returns to a spherical shape in a single period T (not shown). The principal stretch λ defines the deviation of the sphere from its un-stretched diameter D . The subscript pN refers to the maximum value of λ within the N^{th} period. (b) The oscillation period of λ scales with $D/\sqrt{G_\infty/\rho_s}$ (the slope of the linear fit is 1.4). The analytical model predicts a slightly smaller slope (1.2). Large data points represent large spheres ($D = 100$ mm) and small data points represent small spheres ($D = 51$ mm). (c) The peak value of λ for a given period and given sphere radius appears to depend only on $G_\infty/\rho_w U_0^2$. Shading denotes period number (N) as indicated in the legend. Symbols represent experimental data and lines represent model prediction. Thin lines represent small spheres ($D = 51$ mm) and thick lines represent large spheres ($D = 100$ mm). (d) The measured values of λ in time are represented by grey triangles. The behavior predicated by the analytical model is represented by a dashed line. The solid line portrays a time-adjusted model with frequency shifted to correspond with the scaling in (b).

than that in (b); it deforms significantly upon impact creating a much wider cavity and shallower pinch-off event. The smaller G_∞ results in higher magnitude but lower frequency oscillations, creating a second impact-like event within the first cavity. Deformations are even more pronounced in sequence (d). Pinch-off occurs within the second cavity formed for image sequences (c) and (d). Spheres with lower values of G_∞ are often observed to decelerate so rapidly that they occupy the space where a deep seal would normally occur as seen in figure 2.5(e). In this instance the contact line of the second cavity recedes up the surface of the sphere and pinches-off at the top.

Water entry events are often classified by cavity characteristics, with a common parameter being time to pinch-off (t_p). The dimensionless time $t_p U_0 / D$ is plotted against Froude number ($Fr = U_0 / \sqrt{gD}$) in figure 2.6(a) for all tested cases, which is the same non-dimensionalization employed by Aristoff *et al.* for decelerating rigid spheres (dashed line) [4]. However, the scaling does not provide an effective data collapse for deformable elastomeric spheres. Instead we normalize using a new term $D_{\text{eff}} = \lambda_{pN} D$, which represents the maximum deformed diameter that the sphere assumes within the cavity in which pinch-off occurs. For example, in the case seen in figure 2.5(d), pinch-off occurred within the second cavity resulting in $D_{\text{eff}} = \lambda_{p2} D$. This adjustment provides a more convincing data collapse as can be seen in figure 2.6(b), where the solid line is a fit to the data (slope = 1.3).

We have described the effects of elastomeric sphere deformation on the global features of water entry, and now turn attention to sphere dynamics. Based on the description of the sphere as an ellipsoid (figure 2.4(a)), the position of the center of mass is defined as

$$y_c = y_b + \frac{R}{\lambda^2}, \quad (2.1)$$

where, as already discussed, y_b is tracked from images (figure 2.3(c)). Any noise in measurements of λ would be amplified in Eq. 2.1; therefore, we use the time-scaled results of the model simulations to define λ . The velocity and acceleration of the center of mass, \dot{y}_c and \ddot{y}_c , are computed from derivatives of smoothing splines fit to y_c , as was done in [22].

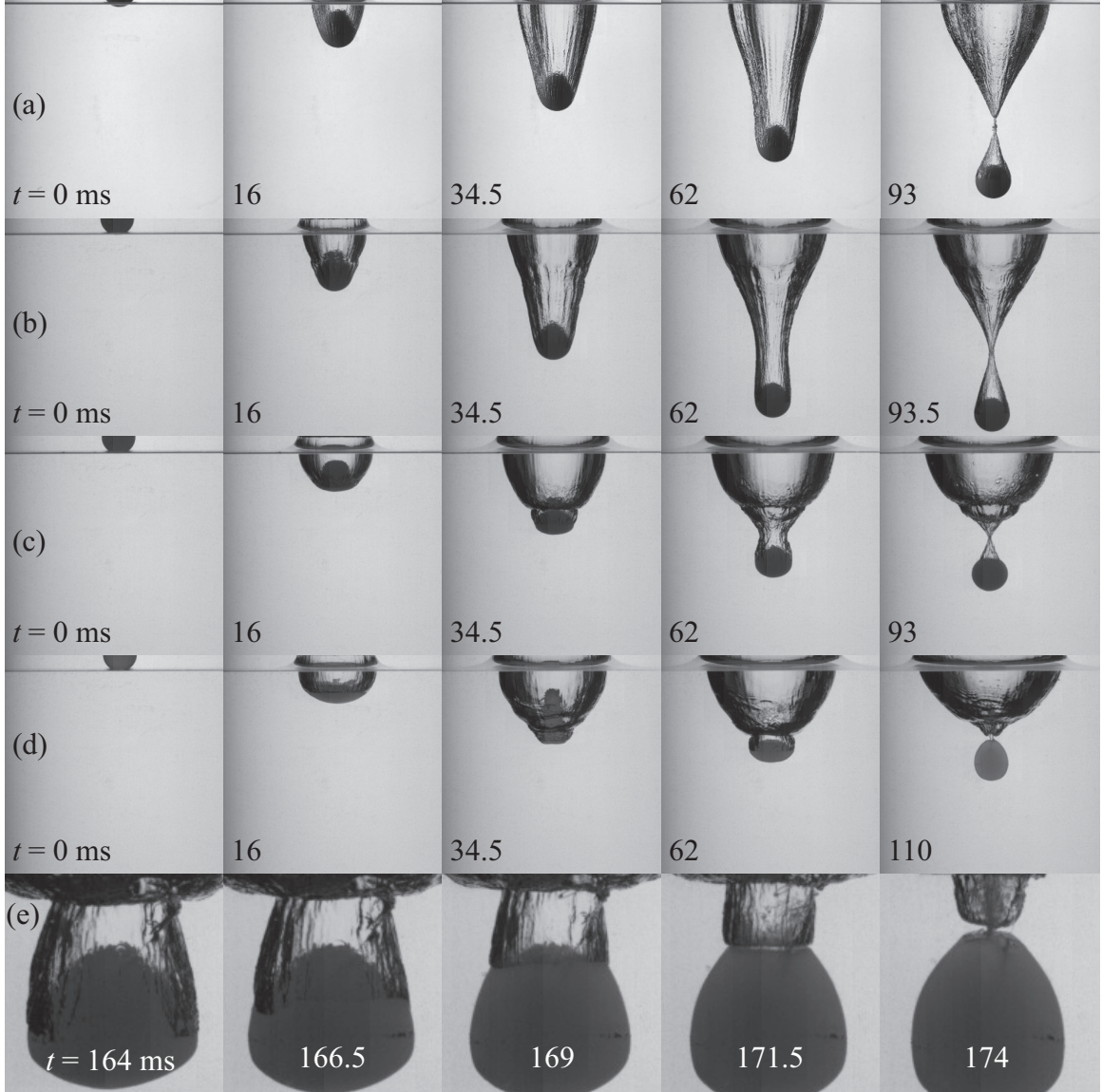


Fig. 2.5: (a)-(d) The water entry of four spheres with identical diameter ($D = 51$ mm), density ($\rho_s = 1070$ kg/m³) and impact velocity ($U_0 = 6.5$ m/s) but varying shear moduli: (a) $G_\infty = 5.66 \times 10^5$ kPa, (b) $G_\infty = 70.2$ kPa, (c) $G_\infty = 6.70$ kPa, (d) $G_\infty = 1.12$ kPa. (e) For the largest and most compliant spheres tested ($D = 100$ mm, $U_0 = 6.5$ m/s and $G_\infty = 1.12$ kPa) spheres decelerate more rapidly, occupying the space where pinch-off would occur. The attached cavity recedes upward along the sphere, pinching at the top of.

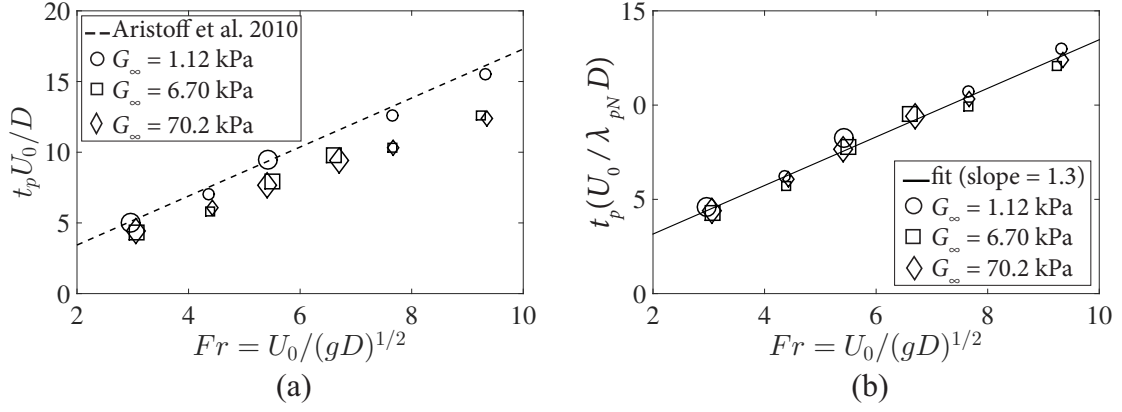


Fig. 2.6: (a) Dimensionless pinch-off plotted against Fr does not produce a convincing collapse as was the case with rigid spheres in the study by Aristoff *et al.* [4]. The dashed line represents the theoretical scaling proposed in the same study. (b) Rather a more accurate scaling is achieved by a dimensionless pinch-off time scaled by $D_{\text{eff}} = \lambda_{pN} D$, which represents the maximum deformed diameter that the sphere assumes within the cavity in which pinch-off occurs (slope of linear fit = 1.3).

Figure 2.7(a)-(c) displays \dot{y}_c as a function of dimensionless time for all values of shear modulus G_∞ , where $D = 51$ mm and U_0 ranges from 3.0 - 6.5 m/s. The values of \dot{y}_c for rigid spheres ($G_\infty = 5.66 \times 10^5$) are plotted as blue curves. The vertical lines indicate the end of the first oscillation period for the elastomeric spheres (corresponding grey shades match the legend in (a)). Elastomeric spheres experience a greater deceleration than the rigid spheres as λD increases. However, the deformable spheres quickly transition to a deceleration rate similar to that of a rigid sphere as the magnitude of λ decreases (compare slopes of grey curves to blue curve after the first oscillation period marked by the vertical lines). Finally, after pinch-off ($t/t_p > 1$), a steady state is reached and spheres fall at nearly constant velocity ($\lambda \rightarrow 1$). Notice that in (c) the softest spheres (lightest grey) lose nearly all of their velocity during the first deformation cycle, whereas more rigid spheres lose a significantly smaller portion.

We perform a scaling analysis of the water entry event to gain insight into the sphere deceleration over the first deformation period. For simplicity, added mass is neglected and thus the dominant forces include drag, gravity and buoyancy. Because the spheres are nearly neutrally buoyant, gravitational and buoyant terms cancel and a simple equation of

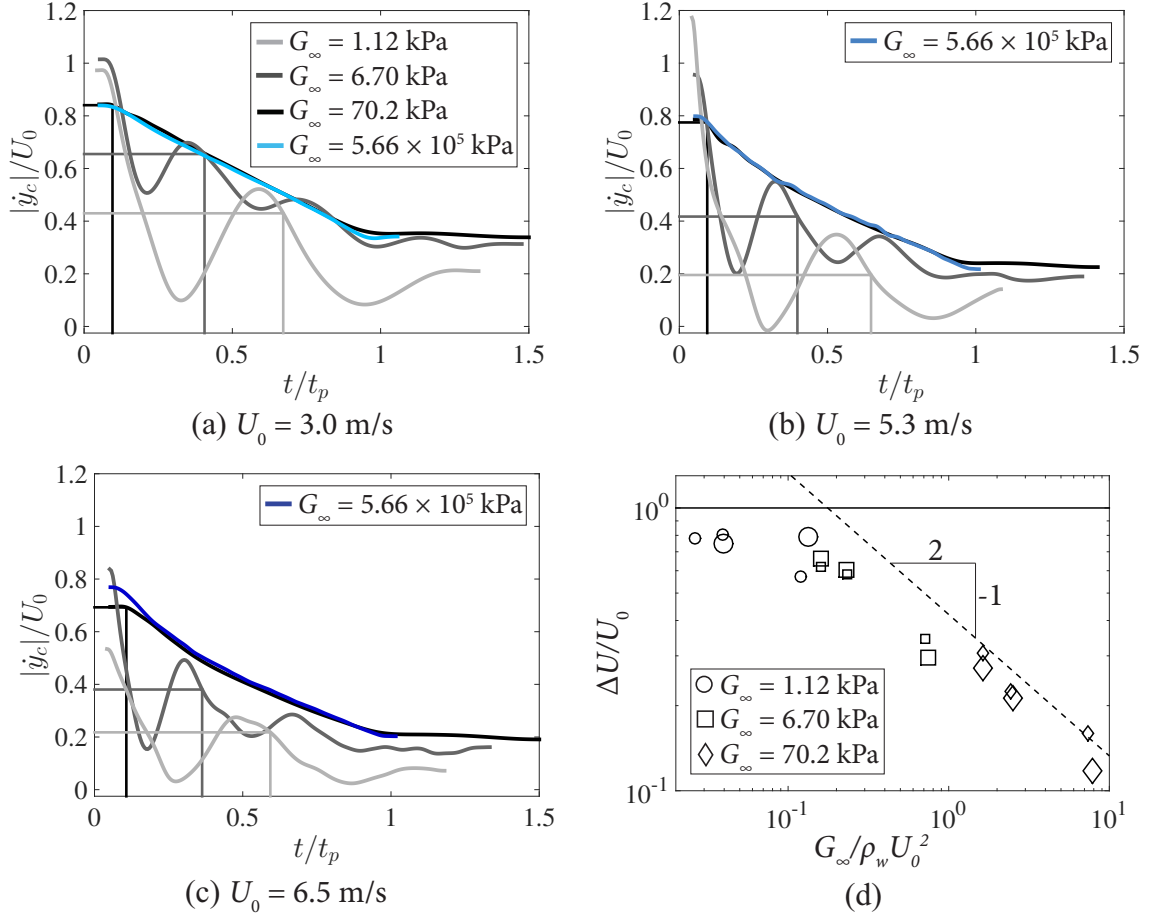


Fig. 2.7: Dimensionless velocity ($|\dot{y}_c|/U_0$) is plotted against dimensionless time (t/t_p) for spheres impacting with three different velocities: (a) $U_0 = 3.0$ m/s, (b) $U_0 = 5.3$ m/s and (c) $U_0 = 6.5$ m/s. Compared to rigid spheres (blue curves), deformable spheres experience a larger deceleration rate after impact over the first cycle of sphere deformation. After the first oscillation period, deformable spheres follow a deceleration similar to rigid spheres, and then transition to a nearly constant velocity after pinch-off. (d) The large initial change in velocity is investigated by plotting $\Delta U = U_1 - U_0$, where U_1 is the velocity of the sphere center of mass after one oscillation period, against $G_\infty/\rho_w U_0^2$. For $G_\infty/\rho_w U_0^2 \gtrsim 0.2$, $\Delta U/U_0$ scales with $(G_\infty/\rho_w U_0^2)^{-1/2}$, as predicted by a scaling analysis from the equation of motion for the sphere. For $G_\infty/\rho_w U_0^2 \lesssim 0.2$, $\Delta U/U_0$ asymptotes to the limit of 1, with nearly all of U_0 being lost over the first period of oscillation.

motion for the impacting sphere can be expressed as

$$\rho_s \forall \ddot{y}_c = \frac{1}{2} \rho_w A U^2 C_D, \quad (2.2)$$

where \forall represents the volume of the sphere, A the cross-sectional area, U the velocity of the center of mass and C_D the coefficient of drag. We simplify this expression by defining a characteristic acceleration $(U_1 - U_0)/T = \Delta U/T$, where U_1 denotes the velocity of the sphere center of mass after the first deformation period. By noting that $\forall \sim D^3$, $A \sim D^2$ and $C_D \sim 1$, we can approximate Eq. 2.2 as

$$\frac{\Delta U}{T} \approx \frac{\rho_w}{\rho_s} \frac{U_0^2}{D}. \quad (2.3)$$

We previously showed that $T \sim D/\sqrt{G_\infty/\rho_s}$ (figure 2.4(b)), and for tested spheres $\rho_w/\rho_s \sim 1$. This allows us to rearrange Eq. 2.3 to

$$\frac{\Delta U}{U_0} \approx \left(\frac{G_\infty}{\rho_w U_0^2} \right)^{-1/2}. \quad (2.4)$$

The velocity $\Delta U/U_0$ is plotted against $G_\infty/\rho_w U_0^2$ in figure 2.7(d). This dimensionless number, which is a ratio of material shear modulus to impact hydrodynamic pressure, collapses the data. For $G_\infty/\rho_w U_0^2 \gtrsim 0.2$, the data follow the scaling predicted by Equation 2.4. However, in the limit of small G_∞ and large U_0 spheres deform significantly, and the argument $A \sim D^2$ no longer holds as there is a more complicated dependence of λ on the material properties and impact conditions. Furthermore, it is likely that added mass plays a more significant role as $G_\infty/\rho_w U_0^2 \rightarrow 0$ (see Supplement 2). When $G_\infty/\rho_w U_0^2 < 0.2$, we find $\Delta U \rightarrow U_0$ within the first oscillation period. Nonetheless, the experimental data follow the proposed scaling well, and this allows us to predict how the impact dynamics of deformable spheres will differ from their rigid counterparts based on material properties and impact conditions.

At this point, it is worth commenting on the expected role of added mass during the water entry event. Prior research on rigid sphere water entry has shown that forces arising

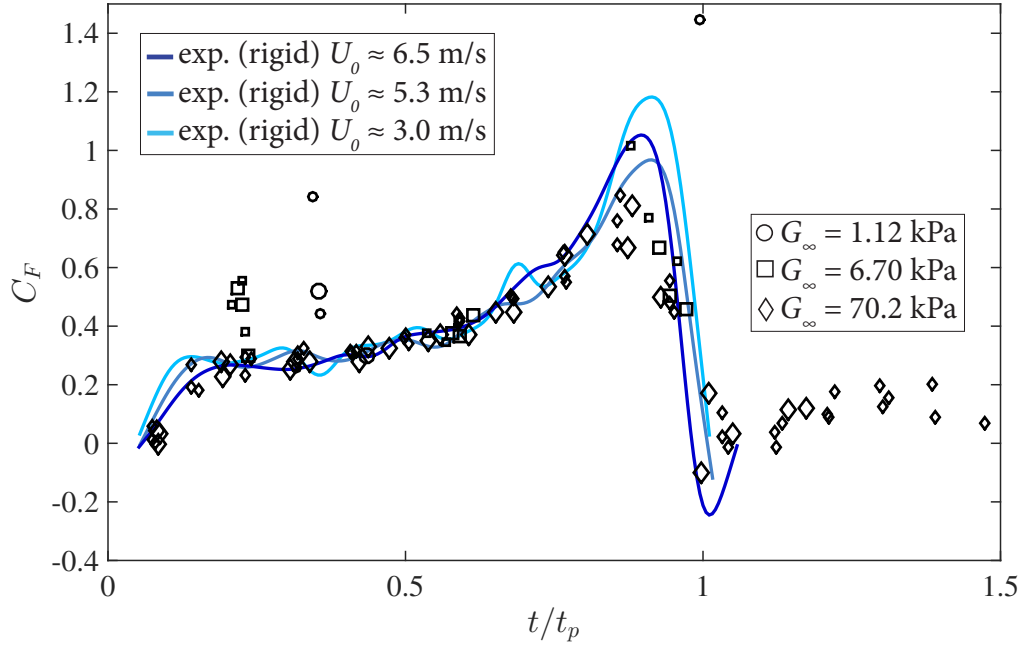


Fig. 2.8: Force coefficients for deformable spheres (\overline{C}_F) calculated by averaging over each deformation period (y -direction) are plotted as a function of dimensionless time (black symbols). The data encompass all sphere diameters, shear moduli and impact velocities tested. Force coefficients (C_F) for rigid spheres entering the free surface with the same specific gravity as the deformable spheres are plotted as a function of dimensionless time (blue curves). The period averaged values for deformable spheres \overline{C}_F follow the instantaneous values for rigid spheres C_F , except during the first sphere deformation period in which deformable spheres experience larger drag from increased λD .

from added mass are significant in the early moments of impact, primarily at times before the entire sphere has passed the free-surface [14, 21, 22]. As discussed earlier, it is likely that the added fluid mass is responsible for the longer oscillation period of the spheres in water. This added mass would be expected to resist sphere acceleration in the direction of travel as the sphere oscillates. While added mass undoubtedly affects the physics of deformable sphere water impact, we argue that it is unlikely to significantly affect the trends in $\Delta U/U_0$ for $G_\infty/\rho_w U_o^2 \gtrsim 0.2$ (see Supplement 2 for more details). This is supported by the good agreement between the experimental data and the predicted trend in figure 2.7(d).

To further investigate how the water entry of a deformable elastomeric sphere differs from that of a rigid sphere, we calculate the total force coefficient acting on the sphere in the y -direction as a function of time. The oscillating behavior of the sphere results in a

varying instantaneous force coefficient C_F . Therefore, we calculate a period-averaged force coefficient,

$$\overline{C}_F = \frac{\rho_s \nabla \overline{\dot{y}}_c}{\frac{1}{2} \rho_w \overline{\dot{y}}_b^2 \pi \left(\frac{\lambda_{pN} D}{2} \right)^2}, \quad (2.5)$$

where $\overline{\dot{y}}_c$ and $\overline{\dot{y}}_b$ are the acceleration and velocity of the center of mass and sphere bottom averaged over a single oscillation period, respectively. Using Eq. 2.5, values for \overline{C}_F are plotted in figure 2.8 as a function of dimensionless time t/t_p for all experimental cases. The period-averaged values \overline{C}_F follow the instantaneous experimental values C_F for three cases of rigid sphere water entry (blue curves). This trend holds except for the first sphere deformation period ($t/t_p \approx 0.2$ to 0.4 depending on G_∞), for which the deformable spheres experience larger drag from increased λD . Over this period, the spheres deform into ellipsoids with a large aspect ratio and thus we expect the force coefficient to be larger. For example, for an ellipsoid with $\lambda = 1.3$, we expect the force coefficient to be between 3-7 times larger than that of a sphere, depending on Reynolds number [10].

2.6 Conclusion

We have shown that deformable elastomeric spheres form cavities that differ from those formed by rigid spheres by being shallower, wider and having undulatory cavity walls. These differences stem from the sphere flattening upon surface impact followed by material oscillation. We describe the deformation and oscillation in terms of both material properties and impact conditions. This allows us to define an effective diameter, which accounts for the deformation and provides effective scaling for time to pinch-off and a period-averaged force coefficient. The large sphere deformation, particularly over the first period, is responsible for the increased loss in velocity as compared to rigid spheres. We have shown how this reduction in velocity scales with the ratio of material shear modulus to impact hydrodynamic pressure ($G_\infty/\rho_w U_0^2$). Surprisingly, we find that except for the unique initial deceleration and altered cavity dynamics, which we have quantified in terms of stiffness and impact velocity, the dynamics for the water entry of deformable elastomeric spheres mirror that of rigid spheres.

2.7 Supplement 1: Viscoelastic model

2.7.1 Describing the sphere deformation

The model of sphere deformation is shown in figure 2.9. The deformation is described by assuming a volume preserving stretch that deforms the sphere into an ellipsoid, with semi axes $(\lambda R, \lambda R, \lambda_3 R)$ aligned with the $\mathbf{e}_1 - \mathbf{e}_2 - \mathbf{e}_3$ coordinate system. The incompressibility condition requires that $\lambda_3 = 1/\lambda^2$. The total deformation gradient can be expressed as

$$\mathbf{F} = \lambda (\mathbf{e}_1 \otimes \mathbf{e}_1 + \mathbf{e}_2 \otimes \mathbf{e}_2) + \frac{1}{\lambda^2} \mathbf{e}_3 \otimes \mathbf{e}_3, \quad (2.6)$$

where \otimes denotes the tensor product of two vectors.

We suppose that the solid can be idealized as a linear viscoelastic Bergstrom-Boyce material [6]. In this model, the total deformation gradient is decomposed into elastic and plastic parts $\mathbf{F} = \mathbf{F}^e \mathbf{F}^p$. For the simple deformation here, both \mathbf{F}^e and \mathbf{F}^p are volume preserving stretches parallel to the basis vectors, so we can write

$$\mathbf{F}^p = \lambda_p (\mathbf{e}_1 \otimes \mathbf{e}_1 + \mathbf{e}_2 \otimes \mathbf{e}_2) + \frac{1}{\lambda_p^2} \mathbf{e}_3 \otimes \mathbf{e}_3 \quad (2.7)$$

$$\mathbf{F}^e = \lambda_e (\mathbf{e}_1 \otimes \mathbf{e}_1 + \mathbf{e}_2 \otimes \mathbf{e}_2) + \frac{1}{\lambda_e^2} \mathbf{e}_3 \otimes \mathbf{e}_3, \quad (2.8)$$

where

$$\lambda = \lambda_e \lambda_p. \quad (2.9)$$

This allows us to calculate the Left Cauchy-Green deformation tensor for the total and elastic deformation gradients

$$\mathbf{B} = \mathbf{F} \mathbf{F}^T = \lambda^2 (\mathbf{e}_1 \otimes \mathbf{e}_1 + \mathbf{e}_2 \otimes \mathbf{e}_2) + \frac{1}{\lambda^4} \mathbf{e}_3 \otimes \mathbf{e}_3 \quad (2.10)$$

$$\mathbf{B}^e = \mathbf{F}^e \mathbf{F}^{eT} = \lambda_e^2 (\mathbf{e}_1 \otimes \mathbf{e}_1 + \mathbf{e}_2 \otimes \mathbf{e}_2) + \frac{1}{\lambda_e^4} \mathbf{e}_3 \otimes \mathbf{e}_3. \quad (2.11)$$

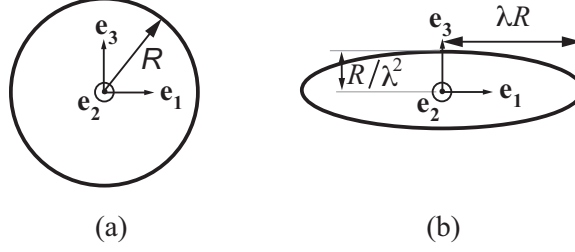


Fig. 2.9: Nominal deformation of the sphere into an axisymmetric ellipsoid.

The invariants of the tensors are

$$I_1 = \text{tr}(\mathbf{B}) = 2\lambda^2 + \frac{1}{\lambda^4} \quad (2.12)$$

$$I_2 = \frac{1}{2}(I_1^2 - \mathbf{B} : \mathbf{B}) = \frac{1}{2} \left[\left(2\lambda^2 + \frac{1}{\lambda^4} \right)^2 - \left(2\lambda^4 + \frac{1}{\lambda^8} \right) \right] \quad (2.13)$$

$$I_1^e = \text{tr}(\mathbf{B}^e) = 2\lambda_e^2 + \frac{1}{\lambda_e^4} \quad (2.14)$$

$$I_2^e = \frac{1}{2}(I_1^{e2} - \mathbf{B} : \mathbf{B}) = \frac{1}{2} \left[\left(2\lambda_e^2 + \frac{1}{\lambda_e^4} \right)^2 - \left(2\lambda_e^4 + \frac{1}{\lambda_e^8} \right) \right]. \quad (2.15)$$

We also need measures of total, elastic and plastic strain rates. We use the symmetric part of the velocity gradient as the strain rate measure

$$\mathbf{D} = \text{sym}(\dot{\mathbf{F}}\mathbf{F}^{-1}) = \mathbf{D}^e + \mathbf{D}^p \quad (2.16)$$

$$\mathbf{D}^e = \text{sym}(\dot{\mathbf{F}}^e\mathbf{F}^{e-1}) \quad (2.17)$$

$$\mathbf{D}^p = \text{sym}(\mathbf{F}^e\dot{\mathbf{F}}^p\mathbf{F}^{p-1}\mathbf{F}^{e-1}). \quad (2.18)$$

For the simple stretch considered here, we get

$$\mathbf{D}^p = \frac{\dot{\lambda}_p}{\lambda_p} (\mathbf{e}_1 \otimes \mathbf{e}_1 + \mathbf{e}_2 \otimes \mathbf{e}_2) - 2\frac{\dot{\lambda}_p}{\lambda_p} \mathbf{e}_3 \otimes \mathbf{e}_3. \quad (2.19)$$

2.7.2 Material model theory

For the special case of an incompressible material, the Bergstrom-Boyce model assumes that the stress can be derived from an elastic strain energy of the form

$$U(I_1, I_2, I_1^e, I_2^e) = U_\infty(I_1, I_2) + U_T(I_1^e, I_2^e). \quad (2.20)$$

We can regard this as a nonlinear version of the 3-parameter Maxwell model (figure 2.10), in which U_T represents the energy in spring k_1 (this energy eventually relaxes to zero if a constant strain is applied to the material) and U_∞ represents the energy in spring k_2 .

The stresses are related to the derivatives of the strain energy in the usual way, giving

$$\sigma = 2 \left[\left(\frac{\partial U_\infty}{\partial I_1} + I_1 \frac{\partial U_\infty}{\partial I_2} \right) \mathbf{B} - \frac{\partial U_\infty}{\partial I_2} \mathbf{B}^2 \right] + 2 \left[\left(\frac{\partial U_T}{\partial I_1^e} + I_1^e \frac{\partial U_T}{\partial I_2^e} \right) \mathbf{B}^e - \frac{\partial U_T}{\partial I_2^e} \mathbf{B}^{e^2} \right] + p \mathbf{1}. \quad (2.21)$$

To model the material used for the spheres presented in this paper, we choose U_∞ and U_T to be the incompressible Neo-Hookean potential

$$U_\infty = \frac{G_\infty}{2} (I_1 - 3) \quad (2.22)$$

$$U_T = \frac{G_T}{2} (I_1^e - 3). \quad (2.23)$$

For this choice, we get

$$\sigma = G_\infty \mathbf{B} + G_T \mathbf{B}^e + p \mathbf{1}. \quad (2.24)$$

We also need an evolution equation for the plastic part of the stretch \mathbf{F}^p . Bergstrom-Boyce suggest the following equation:

$$\mathbf{D}^p = \dot{\epsilon}_0 \left(\sqrt{I_1^p} - \sqrt{3} + \xi \right)^n \left(\frac{\tau_e}{\tau_0} \right)^m \frac{3}{2} \frac{\boldsymbol{\tau}}{\tau_e}, \quad (2.25)$$

where $\dot{\epsilon}_0$, m , n , τ_0 are material properties, ξ is a constant, $\boldsymbol{\tau} = G_T (\mathbf{B}^e - \frac{1}{3} \text{tr}(\mathbf{B}^e) \mathbf{1})$ is the deviatoric part of the ‘dynamic’ stress, and $\tau_e = \sqrt{3 \boldsymbol{\tau} : \boldsymbol{\tau} / 2}$ is the Von Mises uniaxial equivalent dynamic stress. For the volume preserving stretching deformation considered here,

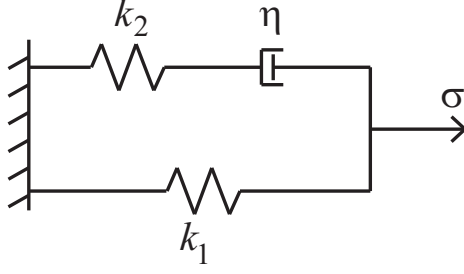


Fig. 2.10: Nonlinear version of the 3-parameter Maxwell model that provides the framework for describing the stress in the Bergstrom-Boyce model.

$$\begin{aligned}
 \frac{\boldsymbol{\tau}}{G_T} &= \lambda_e^2 (\mathbf{e}_1 \otimes \mathbf{e}_1 + \mathbf{e}_2 \otimes \mathbf{e}_2) + \frac{1}{\lambda_e^4} \mathbf{e}_3 \otimes \mathbf{e}_3 - \frac{1}{3} \left(2\lambda_e^2 + \frac{1}{\lambda_e^4} \right) (\mathbf{e}_1 \otimes \mathbf{e}_1 + \mathbf{e}_2 \otimes \mathbf{e}_2 + \mathbf{e}_3 \otimes \mathbf{e}_3) \\
 &= \frac{1}{3} \left(\lambda_e^2 - \frac{1}{\lambda_e^4} \right) (\mathbf{e}_1 \otimes \mathbf{e}_1 + \mathbf{e}_2 \otimes \mathbf{e}_2 - 2\mathbf{e}_3 \otimes \mathbf{e}_3),
 \end{aligned} \tag{2.26}$$

and

$$\tau_e = G_T \left| \lambda_e^2 - \frac{1}{\lambda_e^4} \right|. \tag{2.27}$$

Invoking Eq. 2.19 in Eq. 2.25 we get

$$\frac{\dot{\lambda}_p}{\lambda_p} = \frac{1}{2} \dot{\epsilon}_0 \left(\sqrt{I_1^p} - \sqrt{3} + \xi \right)^n \left(\frac{\tau_e}{\tau_0} \right)^m \text{sign} \left(\lambda_e^2 - \frac{1}{\lambda_e^4} \right), \tag{2.28}$$

where

$$I_1^p = 2\lambda_p^2 + \frac{1}{\lambda_p^4} \tag{2.29}$$

2.7.3 Dynamics

Finally, we need the equation of motion for λ , which will be obtained from the principle of virtual work [8]

$$\int_V (\boldsymbol{\sigma} : \delta \mathbf{D}) dV + \int_V \rho_s (\mathbf{a} \cdot \delta \mathbf{v}) dV + \int_V \rho_s (\mathbf{b} \cdot \delta \mathbf{v}) dV - \int_A (\mathbf{t} \cdot \delta \mathbf{v}) dA = 0, \tag{2.30}$$

where $\delta \mathbf{v} = \delta \dot{\mathbf{V}} \mathbf{x}$ is a virtual velocity field, \mathbf{x} denote the coordinates of a material particle before deformation and

$$\delta \dot{\mathbf{V}} = \delta \dot{\lambda} (\mathbf{e}_1 \otimes \mathbf{e}_1 + \mathbf{e}_2 \otimes \mathbf{e}_2) - \frac{2\delta \dot{\lambda}}{\lambda} \mathbf{e}_3 \otimes \mathbf{e}_3. \quad (2.31)$$

In this analysis, we neglect the effects of gravity and assume there are no external tractions; thus the third and fourth terms in Eq. 3.31 vanish. Invoking Eqs. 2.10-2.11 & 2.24, the first term in Eq. 3.31 becomes

$$\int_V (\boldsymbol{\sigma} : \delta \mathbf{D}) dV = \frac{4}{3} \pi R^3 \left[2G_\infty \left(\lambda - \frac{1}{\lambda^5} \right) + 2G_T \frac{1}{\lambda} \left(\lambda_e^2 - \frac{1}{\lambda_e^4} \right) \right] \delta \dot{\lambda}. \quad (2.32)$$

To evaluate the remaining terms, the following identities are useful

$$\begin{aligned}\int_{V_0} dV_0 &= \frac{4\pi}{3}R^3 \\ \int_{V_0} x_i dV_0 &= 0 \\ \int_{V_0} x_i x_j dV_0 &= \frac{4\pi}{15}R^5 \delta_{ij}\end{aligned}\tag{2.33}$$

where x_i denote the coordinates of a material particle with respect to the center of the sphere and the integrals are evaluated over the undeformed sphere. The inertia term (second term in Eq. 3.31) can be expressed as

$$\begin{aligned}\int_V \rho_s (\mathbf{a} \cdot \delta \mathbf{v}) dV &= \int_V \rho_s [\ddot{\mathbf{F}} \mathbf{x}] \cdot [\delta \dot{\mathbf{V}} \mathbf{x}] dV = \frac{4\pi}{15} \rho_s R^5 [\ddot{\mathbf{F}} \mathbf{F} : \delta \dot{\mathbf{V}} \mathbf{F}^{-T}] \\ &= 2 \left(\ddot{\lambda} - \frac{6\dot{\lambda}^2 - 2\lambda\ddot{\lambda}}{\lambda^7} \right) \delta \dot{\lambda}.\end{aligned}\tag{2.34}$$

Collecting terms gives

$$\frac{4}{3}\pi R^3 \left[2G_\infty \left(\lambda - \frac{1}{\lambda^5} \right) + 2G_T \frac{1}{\lambda} \left(\lambda_e^2 - \frac{1}{\lambda_e^4} \right) \right] + \frac{8\pi}{15} \rho_s R^5 \left(\ddot{\lambda} - \frac{6\dot{\lambda}^2 - 2\lambda\ddot{\lambda}}{\lambda^7} \right) = 0. \tag{2.35}$$

Equations 2.9, 2.27-2.29 & 2.35 are solved in Matlab to resolve the stretch $\lambda(t)$ given initial conditions $\lambda(0) = \lambda_0$, $\lambda_p(0) = 1$ and $\dot{\lambda} = \dot{\lambda}_e = \dot{\lambda}_p = 0$.

2.7.4 Material model calibration

The material model is defined by 7 parameters: G_∞ , G_T , ϵ_0 , m , n , τ_0 and ξ . Without access to the material testing facilities that would be required to fully characterize the silicone materials used in this paper, we adopt a two-part approach to estimate parameters. First, the long time modulus G_∞ is estimated from quasi-static testing in which the actual spheres used in the water entry experiments are compressed on an Instron machine.

This test setup was then numerically modeled using the finite element software Abaqus

Table 2.1: Summary of material properties for the silicone spheres studied.

Sphere radius, R (m)	G_∞ (Pa)	G_T (Pa)	ξ	τ_0	m	n	$\dot{\epsilon}_0$
0.025	74690	74690	0.0866	1.0	1.0	-0.2481	0.0049
0.025	6900	6900	0.0866	1.0	1.0	-0.1902	0.021
0.025	1235	1235	0.0866	1.0	1.0	-1.0	0.0056
0.0487	74690	74690	0.0866	1.0	1.0	-0.2402	0.0024
0.0487	6900	6900	0.0866	1.0	1.0	-0.488	0.0041
0.0487	1235	1235	0.0866	1.0	1.0	-0.50	0.0066

where the sphere was modeled as an axisymmetric solid compressed between two rigid planes accounting for large deformation and frictionless contact. Commanding a displacement profile to match the experimental values, the resulting force is observed. Minimizing the difference in force between the numerical and experimental results is achieved by varying the neo-Hookean shear modulus, G_∞ . The assumption here is that the response is slow enough that the behavior is quasi-static and all rate effects can be neglected, thus we only need to calibrate one parameter [1]. This is consistent with the strain energy defined in Eq. 2.23. We then varied G_∞ to find the value that produced the best fit between the numerically simulated and experimentally measured force-displacement curves. The results of these tests and numerical simulations are shown in figure 2.11.

To estimate the ‘dynamic’ parameters of the material model, we perform an experiment in which all 6 spheres used in the water entry tests are dropped from 3 heights each onto a rigid horizontal surface. The maximum stretch in the plane of the image is measured, as shown in figure 2.12. The sphere response is then simulated using the dynamic model defined in Eqs. 2.9, 2.27-2.29 & 2.35 with the initial stretch λ_0 set to the peak value measured in the experiment. We allow two parameters of the material model to be free - $\dot{\epsilon}_0$, n - and perform a nonlinear least-squares minimization to find the parameters that yield the best fit to the sphere stretch measurements. The material model parameters are summarized in Table 2.1. The simulation results using these material parameters to model the sphere response following impact with the rigid surface are shown in figure 2.12. In modeling the sphere response during water entry, these material parameters are used and the simulations is initialized with λ_0 measured from the experiments.

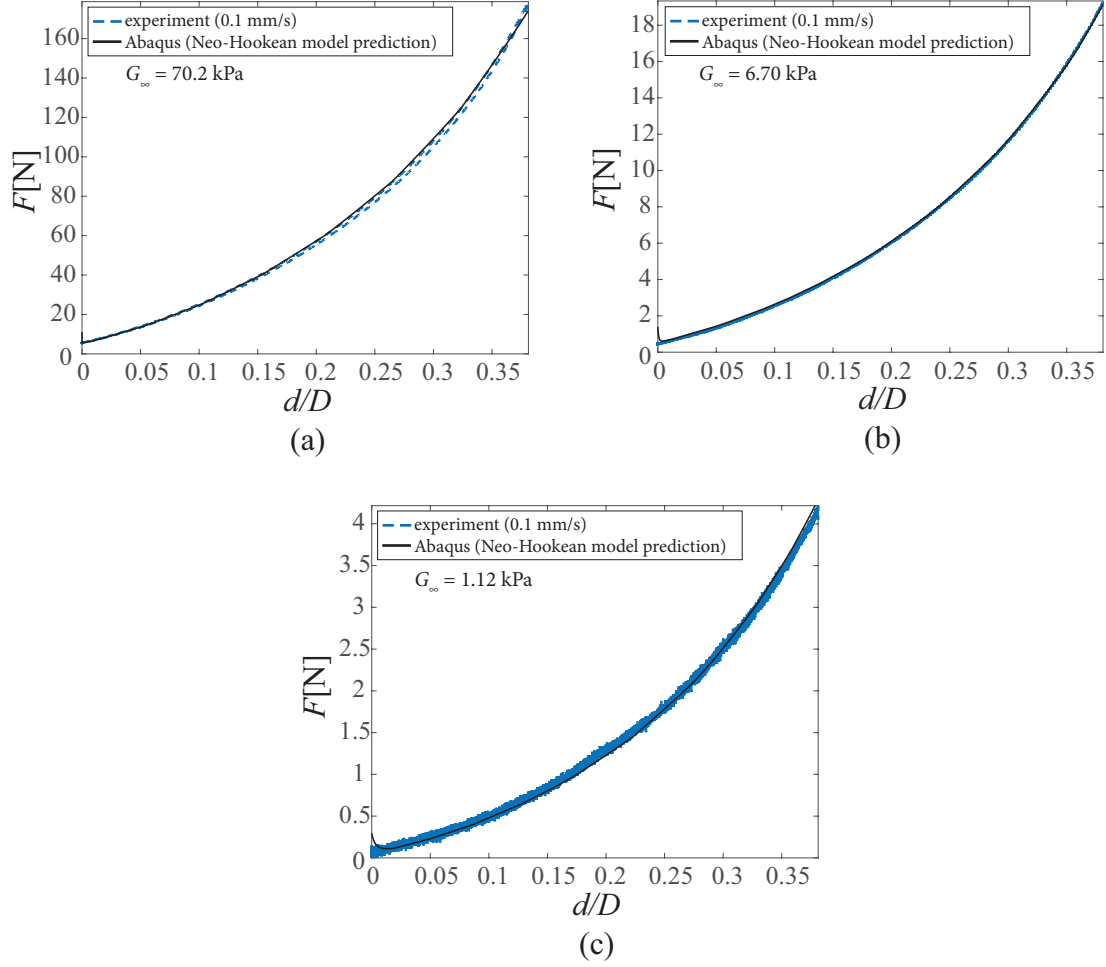


Fig. 2.11: Results from quasi-static testing in which the actual spheres used in the water entry experiments are compressed on an Instron machine at a rate of 0.1 mm/s. The dashed blue lines show the experiments measurements of force as a function of normalized displacement d/D . The solid black lines are predictions from an Abaqus simulation using a hyperelastic neo-Hookean model. The shear modulus G_∞ was adjusted to find the best fit between the simulation and experiment. The three plots correspond to the three stiffness values: (a) $G_\infty = 70.2$ kPa, (b) $G_\infty = 6.70$ kPa and (c) $G_\infty = 1.12$ kPa

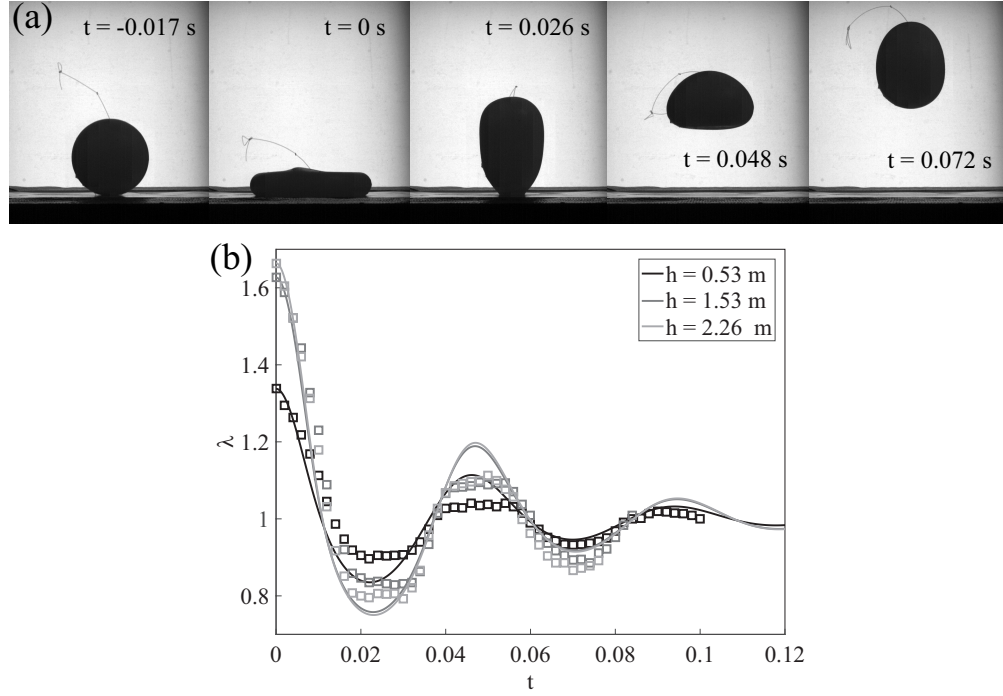


Fig. 2.12: Experiments of the spheres impacting with a rigid horizontal surface were used to calibrate the viscoelastic material model. Results are shown for a sphere with diameter $D = 100$ mm and $G_{\infty} = 6.70$ kPa. (a) Sample high speed images from the $h = 1.53$ m test. (b) The sphere is dropped from three heights above the table and the stretch λ is measured from high speed images (squares). The viscoelastic parameters are found by simultaneously finding the best fit between simulations (lines) of $\lambda(t)$ and the experimental data for all drop heights for a given sphere. Shading indicates the height the spheres were dropped from.

2.8 Supplement 2: Added mass

The scaling analysis outlined in Eqs. 2.2-2.4 neglected the effect of added mass. Here we include an added mass term in the equation of motion for y_c to evaluate the affect on the scaling arguments. Equation 2.2 becomes

$$\rho_s \forall \ddot{y}_c = -\rho_w \forall C_m \ddot{y}_c + \frac{1}{2} \rho_w U^2 C_D A, \quad (2.36)$$

where C_m is an added mass coefficient. Solving for \ddot{y}_c gives

$$\ddot{y}_c = \frac{\rho_w}{2\forall(\rho_s + C_m \rho_w)} U^2 C_D A. \quad (2.37)$$

Using the same scales as used in deriving Eq. 2.4 gives

$$\frac{\Delta U}{U_0} \approx \frac{\rho_w}{\rho_s + C_m \rho_w} \frac{U_0}{\sqrt{G_\infty / \rho_s}}, \quad (2.38)$$

and since for the spheres studied herein $\rho_s \approx \rho_w$, we find

$$\frac{\Delta U}{U_0} \approx \frac{1}{1 + C_m} \left(\frac{G_\infty}{\rho_w U_0^2} \right)^{-1/2}, \quad (2.39)$$

which differs from Eq. 2.4 only by the pre-factor. Based on values of C_m for fully submerged ellipsoids [18], we estimate a representative range of this prefactor as 0.35-0.86 corresponding a range of $\lambda = 1.5$ -0.74. Therefore, as λ becomes larger, which occurs as $G_\infty / \rho_w U_0^2$ gets small, the added mass has a more profound affect on the relationship between $\Delta U / U_0$ and $G_\infty / \rho_w U_0^2$. However, for larger values of $G_\infty / \rho_w U_0^2$, Eq. 2.39 approaches Eq. 2.4. Indeed, for $G_\infty / \rho_w U_0^2 \gtrsim 0.2$ the data in figure 2.7(d) follow the trend predicted by the scaling analysis that excludes added mass.

2.9 Acknowledgements

J.B., T.T.T. and R.C.H. acknowledge funding from the Office of Naval Research, Navy Undersea Research Program (grant N0001414WX00811), monitored by Ms. Maria

Medeiros. J.B. and M.A.J. acknowledge funding from the Naval Undersea Warfare Center In-House Lab Independent Research program, monitored by Mr. Neil Dubois.

REFERENCES

- [1] Abaqus. Abaqus reference manual, 2016.
- [2] J. M. Aristoff and J. W. M. Bush. Water entry of small hydrophobic spheres. *J. Fluid Mech.*, 619:45–78, 2009.
- [3] J. M. Aristoff, T. T. Truscott, A. H. Techet, and J. W. M. Bush. The water-entry cavity formed by low bond number impacts. *Phys. Fluids*, 20(091111), 2008.
- [4] J. M. Aristoff, T. T. Truscott, A. H. Techet, and J. W. M. Bush. The water entry of decelerating spheres. *Phys. Fluids*, 22(032102), 2010.
- [5] J. Belden, R. C. Hurd, M. A. Jandron, A. F. Bower, and T. T. Truscott. Elastic spheres can walk on water. *Nature Communications*, 7(10551), 2016.
- [6] J. S. Bergström and M. C. Boyce. Constitutive modeling of the large strain time-dependent behavior of elastomers. *Journal of the Mechanics and Physics of Solids*, 46.5:931–954, 1998.
- [7] K. G. Bodily, S. J. Carlson, and T. T. Truscott. The water entry of slender axisymmetric bodies. *Phys. Fluids*, 26(072108), July 2014.
- [8] A. F. Bower. *Applied Mechanics of Solids*. CRC Press, 2009.
- [9] B. Chang, M. Croson, L. Straker, S. Gart, C. Dove, J. Gerwin, and S. Jung. How seabirds plunge-dive without injuries. *PNAS*, 113(43):12006–12011, October 2016.
- [10] R. L. Daugherty and J. B. Franzini. *Fluid mechanics with engineering applications*, volume 1. McGraw-Hill, 1977.
- [11] V. Duclaux, F. Caille, C. Duez, C. Ybert, L. Bocquet, and C. Clanet. Dynamics of transient cavities. *J. Fluid Mech.*, 591:1–19, 2007.

- [12] C. Duez, C. Ybert, C. Clanet, and L. Bocquet. Making a splash with water repellency. *Nat. Phys.*, 3:180–183, 2007.
- [13] O. R. Enriquez, I. R. Peters, S. Gekle, L. E. Schmidt, D. Lohse, and D. van der Meer. Collapse and pinch-off of a non-axisymmetric impact-created air cavity in water. *J. Fluid Mech.*, 701:40–58, 2012.
- [14] O. M. Faltinsen and R. Zhao. Water entry of ship sections and axisymmetric bodies. *AGARD Q2 FDP and Ukraine Institute of Hydrodynamics Workshop on High Speed Body Motion in Water*, 24(11), 1998.
- [15] R. Hurd, T. Fanning, Z. Pan, C. Mabey, K. Bodily, K. Hacking, N. Speirs, and T. Truscott. Matryoshka cavity. *Phys. Fluids*, 27(091104), 2015.
- [16] A. May. Vertical entry of missiles into water. *J. Appl. Phys.*, 23, 1952.
- [17] A. May and J. C. Woodhull. Drag coefficients of steel spheres entering water vertically. *J. Appl. Phys.*, 19(1109), 1948.
- [18] J. N. Newman. *Marine Hydrodynamics*. MIT press, 1977.
- [19] E. G. Richardson. The impact of a solid on a liquid surface. *Proc. Phys. Soc.*, 61:352–367, 1948.
- [20] C. M. Seddon and M. Moatamedi. Review of water entry with applications to aerospace structures. *Int. J. Impact Eng.*, 32(1045), 2006.
- [21] T. T. Truscott, B. P. Epps, and J. Belden. Water entry of projectiles. *Annu. Rev. Fluid Mech.*, 46:355–378, 2014.
- [22] T. T. Truscott, B. P. Epps, and A. H. Techet. Unsteady forces on spheres during free-surface water entry. *J. Fluid Mech.*, 704:173–210, 2012.
- [23] T. T. Truscott and A. H. Techet. A spin on cavity formation during water entry of hydrophobic and hydrophilic spheres. *Phys. Fluids*, 21(121703), 2009.

- [24] T. T. Truscott and A. H. Techet. Water entry of spinning spheres. *J. Fluid Mech.*, 625:135–165, 2009.
- [25] A. M. Worthington. *A Study of Splashes*. Longmans, Green, and Company, 1908.

CHAPTER 3

ELASTIC SPHERES CAN WALK ON WATER

3.1 Prologue

The next step in understanding the water impact and skipping characteristics of deformable elastomeric spheres is to consider an oblique, single-impact event. This study was conducted in part at Utah State University and the Naval Undersea Warfare Center in Newport, Rhode Island. The study was published in *Nature Communications* on 4 February 2016 under the title “Elastic spheres can walk on water.” The authors listed are: Jesse Belden, Randy C. Hurd, Michael A. Jandron, Allan F. Bower and Tadd T. Truscott. Though Randy Hurd is not listed as the first author for this paper, it is included in this dissertation because of his significant contribution to the paper. The article in its entirety is presented below.

3.2 Abstract

Incited by public fascination and engineering application, water-skipping of rigid stones and spheres has received considerable study. While these objects can be coaxed to ricochet, elastic spheres demonstrate superior water-skipping ability, but little is known about the effect of large material compliance on water impact physics. Here we show that upon water impact, very compliant spheres naturally assume a disk-like geometry and dynamic orientation that are favorable for water-skipping. Experiments and numerical modeling reveal that the initial spherical shape evolves as elastic waves propagate through the material. We find that the skipping dynamics are governed by the wave propagation speed and by the ratio of material shear modulus to hydrodynamic pressure. With these insights, we explain why softer spheres skip more easily than stiffer ones. Our results advance understanding of fluid-elastic body interaction during water impact, which could benefit inflatable craft

modeling and, more playfully, design of elastic aquatic toys.

Water-skipping has been studied for centuries with diverse motivations including: the ancient art of stone skipping [3, 6, 25, 28], naval application [7, 8, 18–20, 27], water surface craft [13, 31], and biological [5, 12] and biomimetic [10] water-walking. While water-ricochet of rigid objects has been well studied, the physics underlying the water impact of highly deformable elastic solids remains poorly understood [9, 13, 21]. Compliant bodies such as inflatable boats [13] and elastic aquatic toys [30] exhibit behaviour that is not readily explained within the traditional framework for rigid objects. For such elastic bodies, an understanding of the coupling between the material response and hydrodynamic loading is essential to unraveling the overall dynamics.

An object obliquely impacting a water surface with sufficient inertia will carve a cavity on the air-water interface [29] and experience a pressure-driven hydrodynamic force dependent on object velocity, geometry and orientation [2, 20, 22, 24, 28]. Water-skipping occurs when the upward vertical component of this force is large enough to lift the object off the water surface [20]. Studies born from naval applications ranging from cannonball skipping tactics [8, 20] to the dam-busting Wallis bomb [19] have revealed an upper bound on the impact angle β_o (angle between the free-surface and object velocity vector) below which rigid spheres will skip on water [2, 19, 20, 27]. Disk-shaped stones are more amenable to skipping, particularly if one orients the stone at just the right angle [6]. Further research has revealed more details regarding the oblique water impact of these and other canonical rigid body geometries [14, 15, 23, 24]. The referenced ricochet events are dominated by inertia, with negligible contributions from viscous and surface tension forces [28, 29]. In this regime, the physics of water-skipping also generalize to the water-walking ability of basilisk lizards [5, 12] and some birds [5, 32], and to surface craft slamming [31].

In this work, we investigate the skipping of deformable elastic solid spheres on water. We observe that elastic spheres can skip for impact angles nearly three times larger than predicted for rigid spheres. Experiments and numerical modeling show that the spheres deform throughout impact in response to elastic waves propagating in the material. In

some cases these elastic waves actually interact with the air-water interface to create nested cavities. We determine how the deformed geometry scales with material properties and initial impact kinematics. Using an analytical model to relate deformation to the hydrodynamic lift force, we identify the mechanisms by which elastic spheres skip so readily on water. Furthermore, we compute the normal and tangential restitution coefficients and find, surprisingly, that they display analogous behaviour to liquid droplets bouncing on inclined liquid films [11]. Based on our findings about single impact events, we explain how elastic spheres are able to achieve multiple successive skips on water.

3.3 Results

3.3.1 Elastic sphere skipping phenomena

Prior research has reported an upper bound on the impact angle of $\beta_{o\max} = 18^\circ / \sqrt{\rho_s / \rho_w}$ below which rigid spheres (density ρ_s) will skip on water (density ρ_w) [2, 19, 20, 27]. We have found that elastic spheres skip at much larger values of β_o , raising the question of how the elastic response enables this enhanced skipping behaviour. To investigate the mechanisms underlying elastic sphere skipping, we film the water impact of custom-made elastomeric spheres with a high-speed camera viewing from the side. Rigid and elastic spheres having nearly the same radius R and density ρ_s are shown experimentally impacting the water in figure 1(a), (b). Each sphere strikes with approximately the same speed U_o and impact angle β_o , but the elastic sphere has a shear modulus G that is four orders of magnitude smaller than that of the rigid sphere material. Within a few milliseconds after impact, the elastic sphere deforms dramatically and rides along the front of a cavity on the air-water interface before lifting off the surface. By the time the elastic sphere is two diameters above the surface ($t \approx 25$ ms), the rigid sphere has plunged nearly the same distance below it. The elastic sphere evidently experiences a larger upward vertical force from the water.

The extreme sphere deformation is more evident in figure. 1(c), which shows that the water-contacting surface assumes the shape of a disk with a larger radius than that of the undeformed sphere. The disk is oriented at an attack angle α that, unlike for skipping

stones [28], changes in time throughout the impact. Large amplitude oscillations excited by the impact can persist in the sphere after lifting off the surface (figure 1(b)) or even while the sphere is still in contact with the water (figure 1(d)). In the latter case, the sphere vibrations form a group of nested cavities, or a so-called matryoshka cavity [16], named after Russian nesting dolls (figure 1(d)). This phenomenon is in contrast to rigid sphere skipping, for which the cavity is asymmetric, but smooth (figure 1(e)).

3.3.2 Sphere deformation modes

To examine the sphere deformations more thoroughly, we implement a fully-coupled numerical finite element model in Abaqus [17] (see Methods). Figure 2(a) shows the results of a numerical simulation carried out with the same sphere material properties (R , G , ρ_s) and impact conditions (U_o , β_o) as the experimental test shown in Figure 2(b). The numerics reveal an elastic wave propagating around the circumference of the sphere in a counter-clockwise direction. We classify this type of wave propagation, depicted in the line drawing of Figure 2(c), as vibration mode 1^- . In some cases this elastic wave impacts the air-water interface at time t_w , thus initiating a matryoshka cavity (as seen numerically and experimentally in figure 2(a), (b)). While tempting to attribute these kinematics to rigid body rotation, we find that the elastic wave propagation time t_w is typically much smaller than the measured period of rigid rotation (see Methods).

The Abaqus numerical model predicts two additional vibration modes, generally occurring with increasing impact speed and/or decreasing shear modulus. In mode 2 (figure 2(d)), the sphere assumes an ellipsoidal shape with oscillating major and minor axes. In mode 1^+ (figure 2(e)) an elastic wave again propagates around the circumference of the sphere, but in the clockwise direction. Finally, we observe that the attack angle α of the deformed water-contacting face evolves as a result of the elastic wave propagation (figure 2(a), (f)).

3.3.3 Skip-enhancing mechanisms

Based on our experimental observations and numerical simulations (figure (1), (2)), we

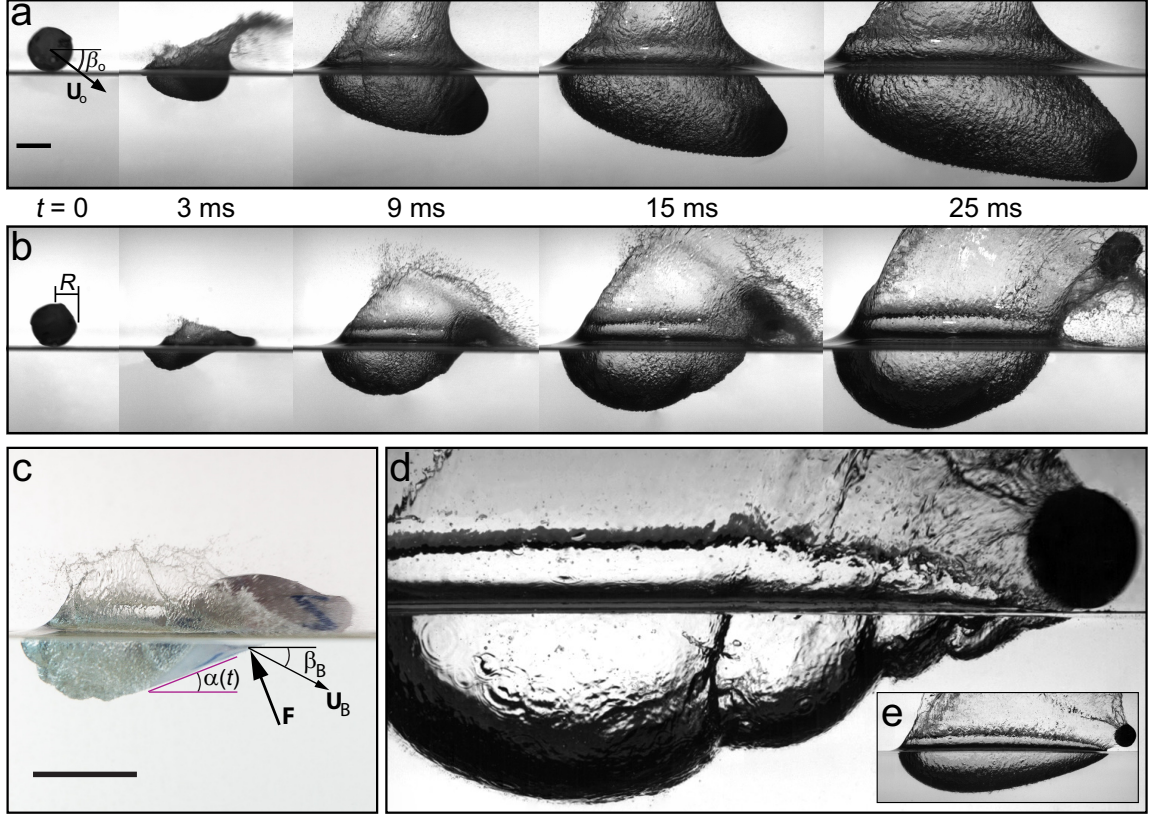


Fig. 3.1: Elasticity alters sphere skipping dynamics. (a) High-speed images of an oblique impact show a rigid sphere carving an air cavity into the water as it dives below the surface ($U_o = 24.3 \text{ m s}^{-1}$; $\beta_o = 29.6^\circ$; $G = 5.66 \times 10^5 \text{ kPa}$; $R = 25.8 \text{ mm}$; $\rho^* = \rho_s/\rho_w = 0.959$). Scale bar, 40 mm. (b) A highly compliant elastic sphere significantly deforms upon impact and skips off the surface ($U_o = 22.0 \text{ m s}^{-1}$; $\beta_o = 32.0^\circ$; $G = 12.3 \text{ kPa}$; $R = 26.2 \text{ mm}$; $\rho^* = 0.937$). (c) The deformed sphere resembles a disk-shaped stone oriented at a dynamic attack angle α . An inertia-dominated hydrodynamic force \mathbf{F} acts on the flattened face, which moves with velocity described by \mathbf{U}_B and β_B . Scale bar, 40 mm. (d) A surprising consequence of the interaction of sphere vibrations with the liquid interface is the formation of nested air cavities (i.e., a matryoshka cavity). (e) A rigid sphere can skip if the impact angle does not exceed $\beta_{o\text{max}} = 18^\circ/\sqrt{\rho^*}$, leaving a smooth, asymmetric cavity on the surface ($\beta_o = 17.3^\circ$ for sphere shown).

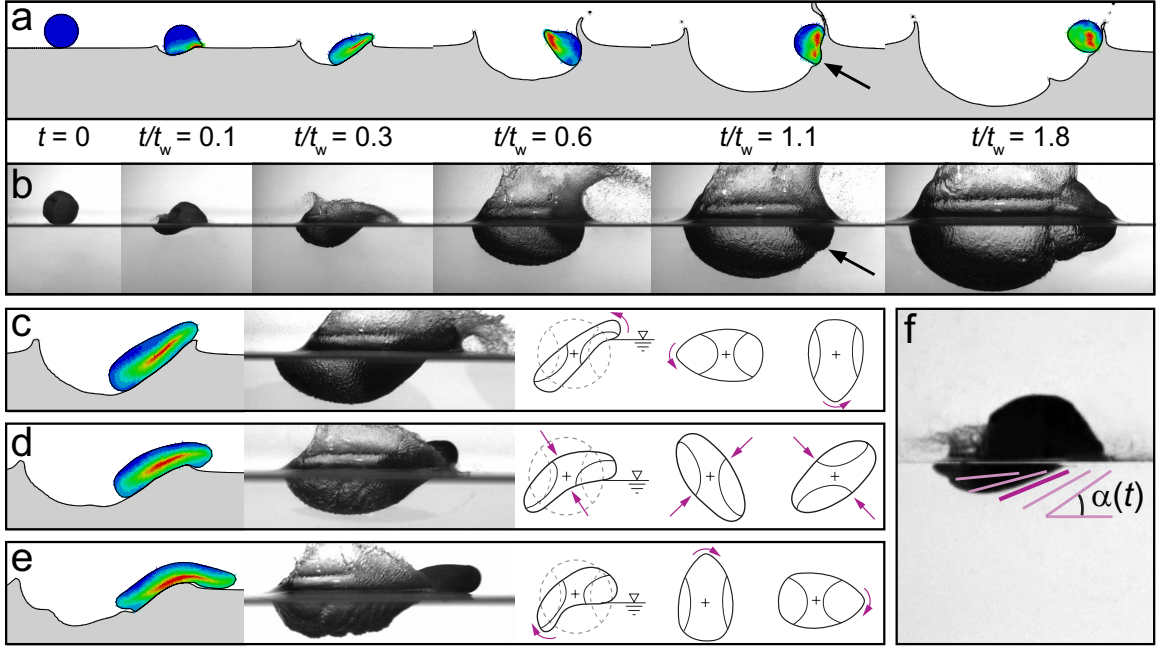


Fig. 3.2: Fluid-structure coupling through sphere deformation modes. (a) An Abaqus numerical model captures the skipping behaviour and reveals the local relative strain in the sphere (colour contours). (b) Under the same conditions as simulated in (a), an experiment shows the formation of a nested cavity (or so-called matryoshka cavity), as also shown by the model. (a) & (c) The model reveals an elastic wave that propagates in a counter-clockwise direction around the sphere (classified as deformation mode 1^-). At time t_w , the elastic wave strikes the air-water interface. Two other deformation modes are observed; (d) mode 2: the sphere assumes an ellipsoidal shape with oscillating major and minor axes; (e) mode 1^+ : an elastic wave propagates in the clockwise direction. (f) The attack angle α evolves in time in response to the elastic wave propagation (deformation mode 1^- is pictured). The purple lines are experimental measurements of α taken at 1.33 ms intervals.

hypothesize that the elastic response of the sphere enhances skipping through two mechanisms: (1) by taking on the shape of a flat disk with an increased wetted area and (2) by acquiring a favorable attack angle.

To connect the suggested skip-enhancing mechanisms to the vertical force acting on the sphere, we propose an analytical model of the coupled fluid-structure interaction. The sphere is idealized as an incompressible, neo-Hookean hyperelastic solid [4] with shear modulus G , radius R and density ρ_s . During water impact, the sphere deforms into a disk-shaped ellipsoid inclined at attack angle $\alpha(t)$ to the water surface (figure 3(a)). A set of equations can then be written for the motion of the center of mass and sphere deformation in terms of general forces and tractions acting on the body (see Methods section).

To couple the sphere response to the fluid loading, we extend an existing hydrodynamic force model for circular disk-shaped skipping stones [28] by approximating the water-contacting face as a circular disk with radius $\lambda_{\text{eq}}R$, where λ_{eq} approximates the sphere deformation (see figure 3(a) and Methods section). The force is modeled as

$$\mathbf{F} = \frac{1}{2}\rho_w|\mathbf{U}_B|^2S_w\sin(\alpha + \beta_B)\mathbf{m}_2 \quad (3.1)$$

where \mathbf{U}_B and β_B describe the velocity of the water-contacting face and the wetted area S_w is proportional to $(\lambda_{\text{eq}}R)^2$. The equation for the vertical motion of the center of mass is then

$$\ddot{d}_2 = \frac{3}{8\pi R^3}\frac{\rho_w}{\rho_s}|\mathbf{U}_B|^2S_w\sin(\alpha + \beta_B)\cos\alpha - g \quad (3.2)$$

where d_2 is the vertical coordinate of the center of mass and g is gravity. We can now predict how the hypothesized mechanisms relate to skipping. First, a larger area S_w increases the magnitude of the hydrodynamic force term in equation 3.59. For a neo-Hookean material, S_w increases with decreasing shear modulus G for a given applied compressive stress [4]. Second, a smaller attack angle increases $\cos\alpha$ thereby increasing the vertical force component that lifts the sphere off the surface. We note that the governing equations for the sphere deformation predict a steady-state solution in which the attack angle evolves

as $\alpha(t) = \frac{1}{R}\sqrt{\frac{5G}{2\rho_s}}t$ in response to a circumferential wave propagating in mode 1^- (see Supplement 1). While the sphere deformation during impact is not steady-state, we nonetheless expect α to be governed by the speed of elastic waves propagating in the sphere through the characteristic distance R such that $\alpha(t) \propto \frac{1}{R}\sqrt{\frac{G}{\rho_s}}t$. Therefore, we predict that a more compliant sphere (smaller G) will assume a smaller rate of change of α , thereby increasing the upward vertical force that enables skipping.

Numerical simulations verify the expected dependence of these two mechanisms on G . Measurements from the Abaqus results show that the rate of change of the attack angle scales as $\dot{\alpha} \propto \frac{1}{R}\sqrt{\frac{G}{\rho_s}}$ for mode 1^- deformations (figure 3(b)). Additionally, we find that the maximum value of λ_{eq} achieved during impact, which we call λ_{max} , increases with a decrease in the dimensionless term $G/\rho_w U_o^2$ (figure 3(c)), which is the ratio of material stiffness to hydrodynamic pressure. Therefore, a smaller G yields a larger stretch and larger wetted area, as well as a smaller rate of change of α , as predicted.

To confirm that these mechanisms indeed enhance skipping, we perform experiments and simulations over a range of impact conditions and sphere properties and measure the minimum impact speed required to skip U_{min} , as a function of G (figure 4). Above a certain value of G ($\approx 10^3 - 10^4$ kPa, depending on β_o), we recover the rigid skipping regime, in which U_{min} is independent of shear modulus but is very sensitive to β_o . For rigid spheres impacting above $\beta_{o\text{max}} = 18^\circ/\sqrt{\rho^*}$, where $\rho^* = \rho_s/\rho_w$, prior research suggests spheres may broach (i.e., become completely submerged before exiting), but not skip [20] (figure 4(f)). For stiffness values below the rigid regime, the elasticity of the sphere becomes important and U_{min} decreases monotonically with decreasing shear modulus. Our analytical model accurately predicts the experimental and numerical results in this regime. The minimum speed is also much less sensitive to β_o in the elastic skipping regime and as a result we observe skipping at impact angles nearly three times larger than predicted for rigid spheres (figure 4 and figure 9 in Supplement 1).

While our results show that reducing shear modulus has the predicted effect on wetted area and attack angle (figure 3(b), (c)), it is unclear whether one or both of these mechanisms

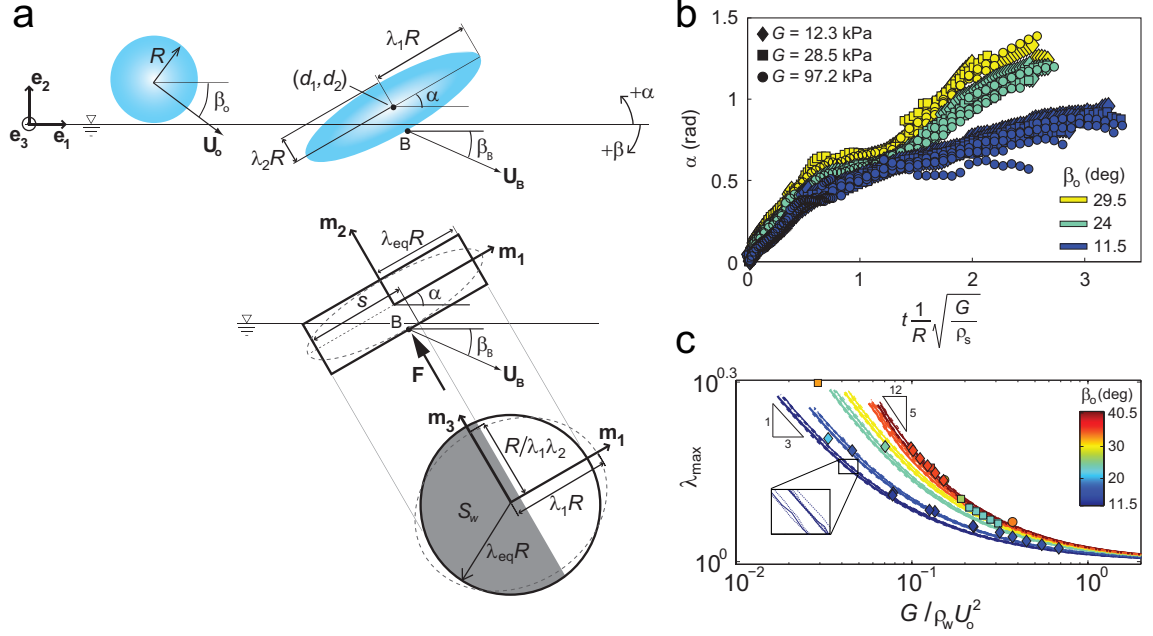


Fig. 3.3: Description of sphere deformation during impact. (a) Our analytical model assumes the deformed sphere takes an ellipsoidal shape with principal stretches λ_1 , λ_2 and $\lambda_3 = 1/\lambda_1\lambda_2$ aligned with the body-fixed $\{\mathbf{m}_1, \mathbf{m}_2, \mathbf{m}_3\}$ coordinates, respectively. The $\{\mathbf{m}_1, \mathbf{m}_2, \mathbf{m}_3\}$ coordinate system is inclined at attack angle α relative to the free-surface and has its origin at the sphere's center of mass (d_1, d_2) . To model the hydrodynamic force \mathbf{F} , we represent the sphere as a circular disk with radius $\lambda_{\text{eq}}R$ and assume that \mathbf{F} acts at the point B on the water-contacting face, which moves with velocity described by \mathbf{U}_B and β_B . (b) The attack angle α is measured from simulations using our Abaqus numerical model for spheres undergoing mode 1⁻ deformations, with properties $R = 25.4$ mm, $\rho^* = 1.05$ and varying shear modulus; sample α measurements are shown in figure 4b-d. The attack angle is collapsed by the dimensionless time $\frac{1}{R}\sqrt{\frac{G}{\rho_s}}$, which is proportional to the speed of mode 1⁻ elastic waves propagating through the characteristic distance R . These attack angle data are fed into our analytical model (see Methods section). (c) The simulations also show the dependence of λ_{max} on $G/\rho_w U_o^2$, where λ_{max} is the maximum value of λ_{eq} achieved during impact (individual marker shapes same as for (b)). The numerical results agree with predictions from our analytical model (the zoomed region shows the nine different line styles corresponding to analytical results for nine different spheres: dashed lines $R = 20.1$ mm; solid lines $R = 26.2$ mm; dash-dot lines $R = 48.8$ mm; line width indicates G : thin $G = 12.3$ kPa; middle $G = 28.5$ kPa; thick $G = 97.2$ kPa). In the limit of small G , we find $\lambda_{\text{max}} \propto (G/\rho_w U_o^2)^{-1/3}$ (valid for shallow β_o). For steeper β_o , we find $\lambda_{\text{max}} \propto (G/\rho_w U_o^2)^{-5/12}$ for decreasing $G/\rho_w U_o^2$.

are responsible for the observed improved skipping performance. To isolate the mechanisms we consider the limiting case of small G , for which $\dot{\alpha} \propto \frac{1}{R} \sqrt{\frac{G}{\rho_s}} \rightarrow 0$ and thus $\cos \alpha \approx 1$ over typical impact timescales. The expected dependence of U_{\min} on G in this limit can be rationalized by scaling analysis of equation 3.59 (see Methods and Supplement 2), which gives

$$\frac{2R}{t_c^2} \approx \frac{3}{8\pi R \rho^*} U_{\min}^2 \lambda_{\max}^2 - g \quad (3.3)$$

where t_c is the collision time (i.e., time in which the sphere is in contact with the water). For threshold skipping cases, we expect the characteristic acceleration $2R/t_c^2$ to be small compared to gravity and thus, to first order, $3U_{\min}^2 \lambda_{\max}^2 / 8\pi R \rho^* \approx g$. Furthermore, in the small G limit our numerical modeling shows that $\lambda_{\max} \propto (G/\rho_w U_{\min}^2)^{-1/3}$ (figure 3(b)). Applying this dependence and solving for U_{\min} , we find $U_{\min} \propto (g \rho^* R)^{3/10} (G/\rho_w)^{1/5}$. Figure 4(a) shows that U_{\min} approaches the $G^{1/5}$ relation in the limit of small G , indicating that the only mechanism by which reducing shear modulus enhances skipping in this limit is through the increased wetted area. However, for larger G ($> \approx 10$ kPa), U_{\min} deviates from the $G^{1/5}$ relation as the coupling between shear modulus and α becomes important (figure 4(a)-(d)). As stiffness continues to increase, ultimately the amplitude of the deformations (affecting both S_w and α) become negligible and the sphere is effectively rigid (figure 4(a), (e)). Consequently, we conclude that decreasing shear modulus below this rigid boundary causes an increase in the upward vertical force that promotes skipping through both of the hypothesized mechanisms, save for the limit of small G where decreasing shear modulus only affects lift by increasing S_w .

3.3.4 Skipping regimes

As the impact events devolve from clear skipping to water entry, we observe a transitional regime characterized by a matryoshka cavity, in which the sphere still skips (figure 1(d)). The matryoshka phenomenon occurs when the total contact time of the sphere with water t_c is longer than the wave time t_w associated with mode 1⁻ elastic wave propagation, such that $t_c/t_w > 1$. We define t_w as the time from impact until the circumferential

Fig. 3.4: The effect of material stiffness on skipping behaviour. (a) Below a threshold stiffness ($G \approx 10^3 - 10^4$ kPa, depending on β_o), the elastic response of the sphere affects skipping. In this elastic regime, the minimum speed required to skip U_{\min} decreases monotonically with decreasing shear modulus G , as shown by both experimental and numerical results (triangle and star markers, respectively). In the limit of small G we expect $U_{\min} \propto G^{1/5}$, which is confirmed by the numerics. As stiffness increases above $G \approx 10$ kPa, U_{\min} deviates from this relation as larger G augments the rate of change of α , thereby reducing the upward vertical force component. Our analytical model also captures this change in behaviour (solid coloured lines). For shallow impact angle, U_{\min} becomes insensitive to shear modulus for $G > \approx 10^3$ kPa, indicating that rigid sphere skipping behaviour is recovered. The transition between the elastic and rigid skipping regime occurs at larger G as β_o increases. In the rigid skipping regime, U_{\min} is very sensitive to β_o (also evident in figure 9). The lower bound of the rigid skipping regime is inferred from the dark triangle symbols, which occur for experiments with $\beta_o \sqrt{\rho^*} < 14.5^\circ$. The coloured triangle markers at $G = 5.66 \times 10^5$ kPa result from experiments where the colour gradient on the marker indicates the uncertainty in $\beta_o \sqrt{\rho^*}$. The upper bound on the rigid regime corresponds to $\beta_o \sqrt{\rho^*} = 18^\circ$; prior literature suggests that for $\beta_o \sqrt{\rho^*} > 18^\circ$ spheres may broach (i.e., completely immerse before exiting), but not skip [20]. (b)-(d) Numerical simulations show that increasing G results in a larger rate of change of α (purple lines) in the elastic skipping regime. Each image shown is 6 ms after impact and the interval between α measurements is 2 ms. (e) As shear modulus increases into the rigid regime, the sphere deformation is negligible (black outline is undeformed sphere contour). (f) We have observed broaching for rigid spheres impacting with $\beta_o \sqrt{\rho^*} > 18^\circ$. Sphere properties for data in (a): rigid sphere experiments, $R = 25.8$ mm, $\rho^* = 0.959$, $G = 5.66 \times 10^5$ kPa; all other data markers, $R = 26.2$ mm, $\rho^* = 0.937$ for $G \leq 12.3$ kPa and $\rho^* = 1.03$ for $G > 12.3$ kPa. The purple error bars are characteristic for experimental data. The numerical error bars represent $\pm 1/2$ of the difference in U_o between the skipping and non-skipping cases used to compute U_{\min} ; error bars are offset for clarity.

elastic wave strikes the air-water interface (figure 2(a), (b)). Experiments over a range of sphere properties and impact conditions reveal that t_c/t_w is governed by the impact angle β_o and the ratio $G/\rho_w U_o^2$ (figure 5). The dependence on these terms can be rationalized by scaling analysis with U_o replacing U_{\min} in equation 3.3. When $t_c \approx t_w$, the characteristic sphere acceleration is much greater than g such that $2R/t_c^2 \approx 3U_o^2 \lambda_{\max}^2 / 8\pi R \rho^*$ and we find $t_c \propto R\sqrt{\rho^*}/U_o \lambda_{\max}$ (see Methods section). Furthermore, based on the propagation speed of mode 1^- elastic waves, we expect $t_w \propto 1/\dot{\alpha} \propto R/\sqrt{G/\rho_s}$, which is confirmed experimentally (figure 10). Combining the scaling for each time gives $t_c/t_w \propto (G/\rho_w U_o^2)^{1/2} / \lambda_{\max}$. We can now examine the evolution of the timescale ratio in the vicinity of the transitional regime in the limit of shallow ($\beta_o \rightarrow 0$) and steep impact angles, making use of the relationship between λ_{\max} and $G/\rho_w U_o^2$ shown in figure 3(c). Here, we consider steep impact angles to be $\beta_o \rightarrow \beta_{\text{oEM}}$, where β_{oEM} is the maximum impact angle at which we have observed elastic sphere skipping ($\beta_{\text{oEM}} \approx 47^\circ$). In the shallow β_o limit, $t_c/t_w \approx 1$ occurs at values of $G/\rho_w U_o^2 > 0.1$, for which $\lambda_{\max} \rightarrow 1$ (figure 3(c)); thus, we anticipate $t_c/t_w \propto (G/\rho_w U_o^2)^{1/2}$ for shallow angles. For steep β_o , the transitional regime occurs for $G/\rho_w U_o^2 < 0.1$, for which $\lambda_{\max} \propto (G/\rho_w U_o^2)^{-5/12}$ (figure 3(c)), and we expect $t_c/t_w \propto (G/\rho_w U_o^2)^{11/12}$. These limiting relations capture the evolution of t_c/t_w observed experimentally (figure 5) and provide insight into the differences observed at different impact angles. We see that for steeper β_o , the sphere deformation has a larger effect on the collision time, which gets manifested as a higher sensitivity of t_c/t_w to $G/\rho_w U_o^2$.

Based on our findings regarding the transitional skipping regime, we hypothesize that the same dimensionless parameters (i.e., β_o and $G/\rho_w U_o^2$) govern all deformation modes and associated skipping behaviour. An empirical regime diagram indeed shows that these parameters classify all observed skip types (figure 6). Mode 1^+ is promoted by shallow β_o , large U_o and/or small G . As stiffness becomes large relative to hydrodynamic pressure, the vibration type traverses the mode 2 and mode 1^- regimes. Our analytical model correctly predicts the boundary between the mode 1^- skipping ($t_c/t_w < 1$) and mode 1^- transitional ($t_c/t_w > 1$) regimes (marked by red line on figure 6). A small, radius dependent overlap

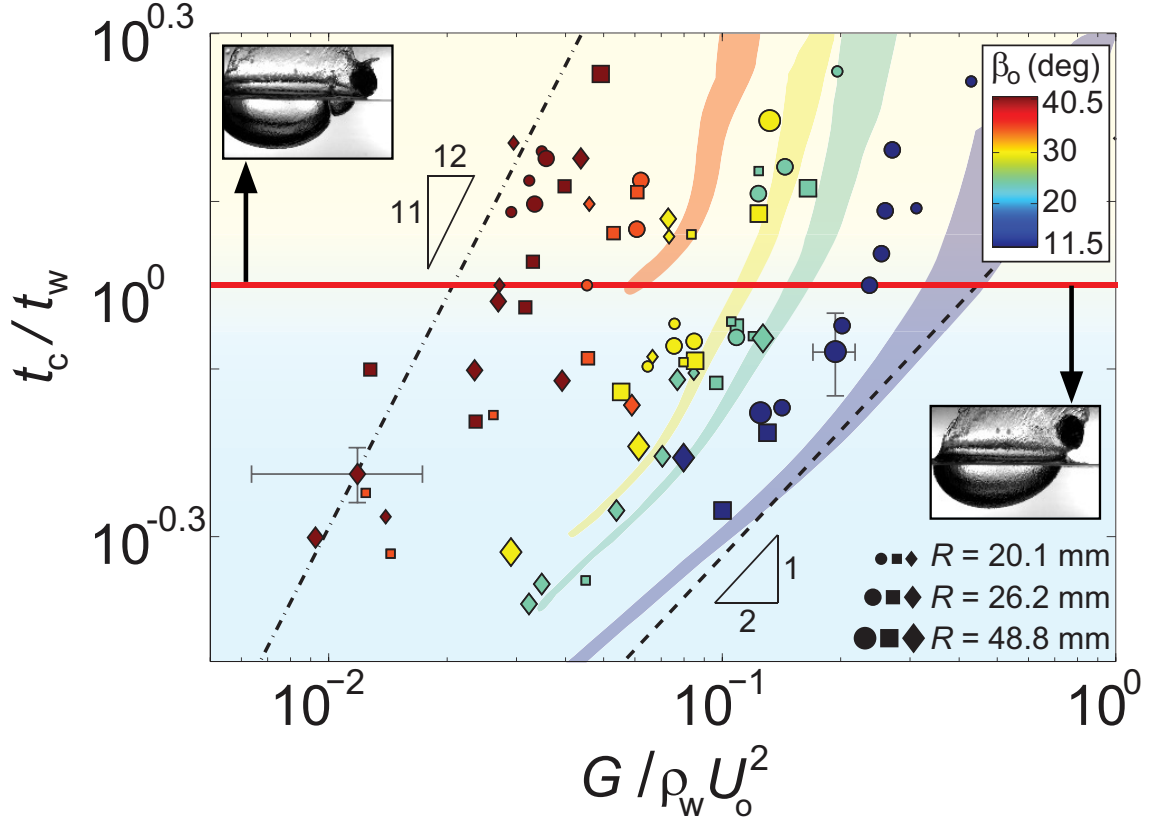


Fig. 3.5: Matryoshka cavities depend on two timescales. When conditions produce impacts in which the collision time t_c is longer than the elastic wave propagation time t_w (i.e., $t_c/t_w > 1$) matryoshka cavities form. Experiments show that the timescale ratio depends on $G/\rho_w U_o^2$ and β_o , with seemingly minimal dependence on R (marker size indicates R ; marker shapes indicate same G as for figure 3(b)). The four coloured patches result from calculations using our analytical model with the same material properties. Varying R in the model over the range experimentally tested results in the spread in the patches, which is small for $t_c/t_w < 1$. For shallow impact angles, scaling analysis predicts $t_c/t_w \propto (G/\rho_w U_o^2)^{1/2}$ (dashed line), while for steep impact angles we expect $t_c/t_w \propto (G/\rho_w U_o^2)^{11/12}$ (dash-dot line). These limiting trends capture the general evolution shown by the experimental data. Characteristic error bars are shown.

region exists between the transitional regime and water entry. Finally, we have observed that the vibration mode associated with the transitional and water entry regimes is exclusively mode 1^- .

3.3.5 Skipping sphere rebound

We quantify the rebound characteristics of skipping spheres by computing the normal and tangential coefficients of restitution, $\varepsilon_n = U_{e_n}/U_{o_n}$ and $\varepsilon_t = U_{e_t}/U_{o_t}$, where U_e is the exit velocity and n and t refer to components normal and tangential to the free-surface, respectively. Here, we find some interesting similarities between skipping elastic spheres and liquid droplets bouncing on inclined liquid layers [11]. Follow the work on bouncing liquid droplets, we plot ε_n^2 and ε_t^2 as a function of $\rho_w U_{o_n}^2/G$ (figure 7), which is equivalent to the normal Weber number ($We_{o_n} = \rho_w U_{o_n}^2 R_d/\sigma$) with shear modulus G replacing the Laplace pressure σ/R_d , where R_d is the droplet radius and σ is surface tension of the liquid droplet. Interestingly, we find $\varepsilon_n^2 \propto (\rho_w U_{o_n}^2/G)^{-1/2}$ and $\varepsilon_t^2 \propto (\rho_w U_{o_n}^2/G)^{-1/3}$, which are the same scaling relations found for liquid droplets bouncing on inclined liquid layers [11]. The restitution coefficients deviate from these trends when $t_c/t_w > 1$. In these cases, sphere vibrations interact with the water via the matryoshka cavity causing a significant decrease in bouncing efficiency. For both elastic skipping spheres and bouncing droplets, the restitution coefficients are always less than one as part of the initial translational kinetic energy goes into post-impact vibrations in the sphere or droplet [11, 26].

We build on the bouncing droplet analogy to speculate on the lower bound of validity of the $U_{\min} \propto G^{1/5}$ scaling relation in the limit $G \rightarrow 0$ (figure 4). When the relative magnitude of droplet surface tension becomes small for liquid droplets impacting liquid layers, bouncing does not occur and the droplet completely merges with the liquid layer [11]. We conjecture about a similar limit for elastic spheres with $G \rightarrow 0$ and impacting with $We = \rho_w U_o^2 R/\sigma_w \approx 1$, where σ_w is the surface tension of water. In this limit, we expect the surface tension force from the water to act prominently on the sphere [1] and to inhibit sphere reformation, thus preventing recovery of translational kinetic energy from deformational potential energy during impact. As a result, we hypothesize that sphere skipping would

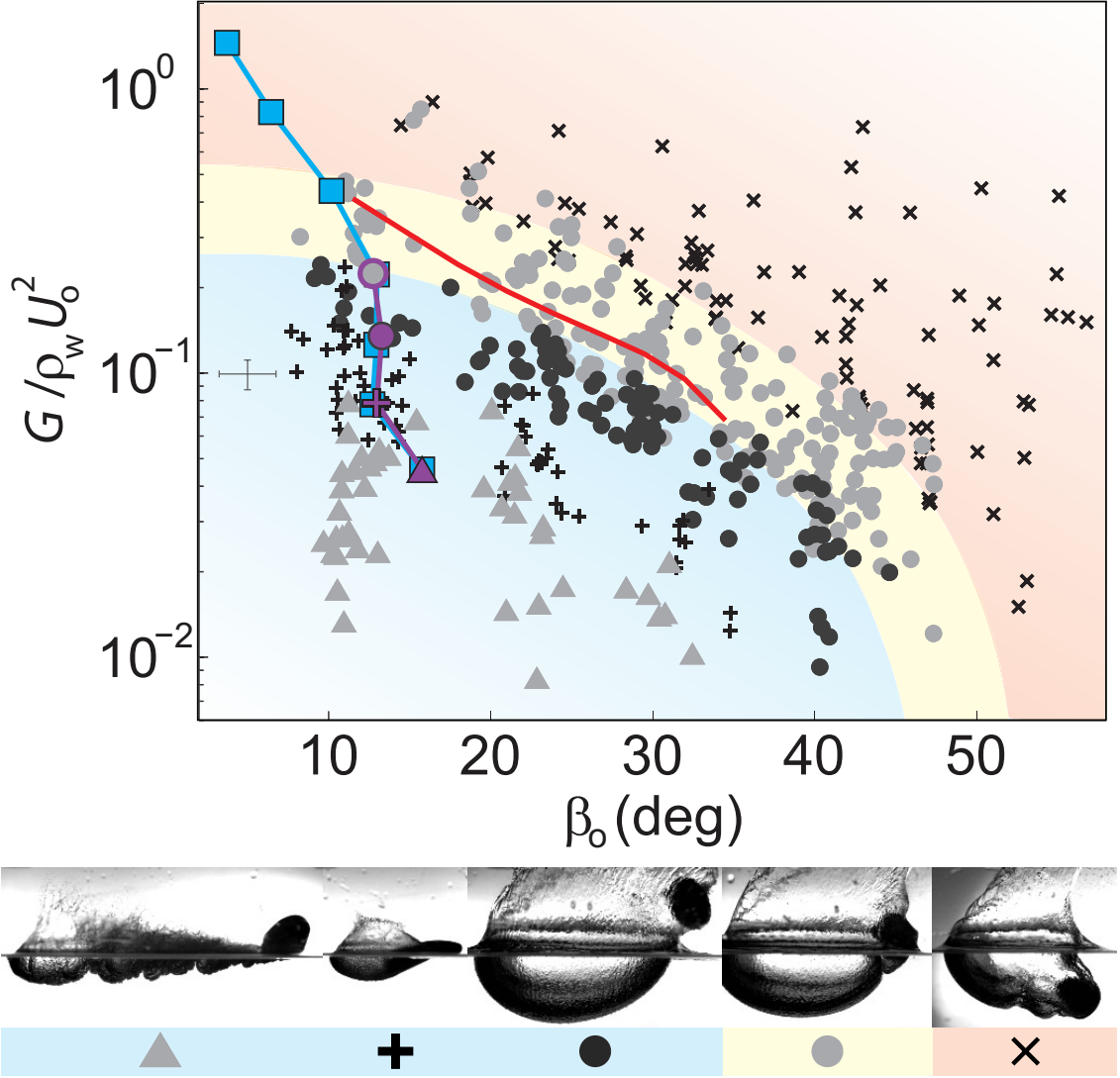


Fig. 3.6: Classification of impact phenomena for single and multiple skip events. Experiments show that all vibration modes and accompanying skipping behaviour are classified by the ratio of material stiffness to hydrodynamic pressure ($G/\rho_w U_o^2$) and β_o (triangles: mode 1^+ ; crosses: mode 2; black circles: mode 1^- skipping; gray circles: mode 1^- transitional; x-marks: water entry). The experimental data shown are for all three elastic sphere radii. The coloured regions provide a visual boundary of the skipping (blue), transitional (yellow) and entry (red) regimes. Our analytical model accurately predicts the boundary between mode 1^- skipping and transitional events; the red line is found from the intersection of the analytical results with $t_c/t_w = 1$ in figure 5. Given initial conditions of the first skip, our analytical model also predicts successive impact types in a multiple skip trajectory (blue squares). A multiple skip experiment (figure 8) validates these predictions within the limits of our test facility ($R = 26.2$ mm, $G = 12.3$ kPa, $\rho^* = 0.937$). Characteristic error bars are shown in gray.

ultimately cease in this limit. We anticipate these dynamics would become relevant when $G \approx \sigma_w/R$ (see figure 11 and Supplement 3). To validate these predictions is beyond the scope of the present work.

3.4 Discussion

Perhaps the most mesmerizing manifestation of elastic sphere water impact is continual skipping across water. To confirm that our physical description of a single skip generalizes to multiple skip events, we predict the placement of successive impacts on the regime diagram (figure 6). An experimental investigation using isolated water tanks validates the predictions and shows the sphere traversing through the vibration modes with each impact (figure 8). As to how repeated skipping is sustained over very long skipping trajectories, we gain insight from the behaviour of the restitution coefficients (figure 7). First, ε_t is consistently larger than ε_n , which causes β_o to decrease and thus become more favorable with each skip. Second, the restitution coefficients actually become larger as U_{on} decreases, until the sphere enters the mode 1^- skipping and transitional regimes. Therefore, one could say it becomes easier to skip with every skip.

While toy elastic balls may bestow upon the casual sportsman the ability to break the world stone skipping record (88 skips by K. Steiner, Guinness World Records), we believe the physics underlying the elastic sphere impact are common to the large deformation hydroelastic response of surface-riding and skipping compliant bodies. Models of these structures, such as inflatable boats, typically ignore extreme elastic deformation even though it is known to affect drag, stability and slamming loads [13]. The mechanisms of form and force augmentation, as well as the secondary vibration-induced fluid interactions that we have revealed, can be exploited for functional advantage and incorporated into higher-fidelity hydroelastic models.

3.5 Methods

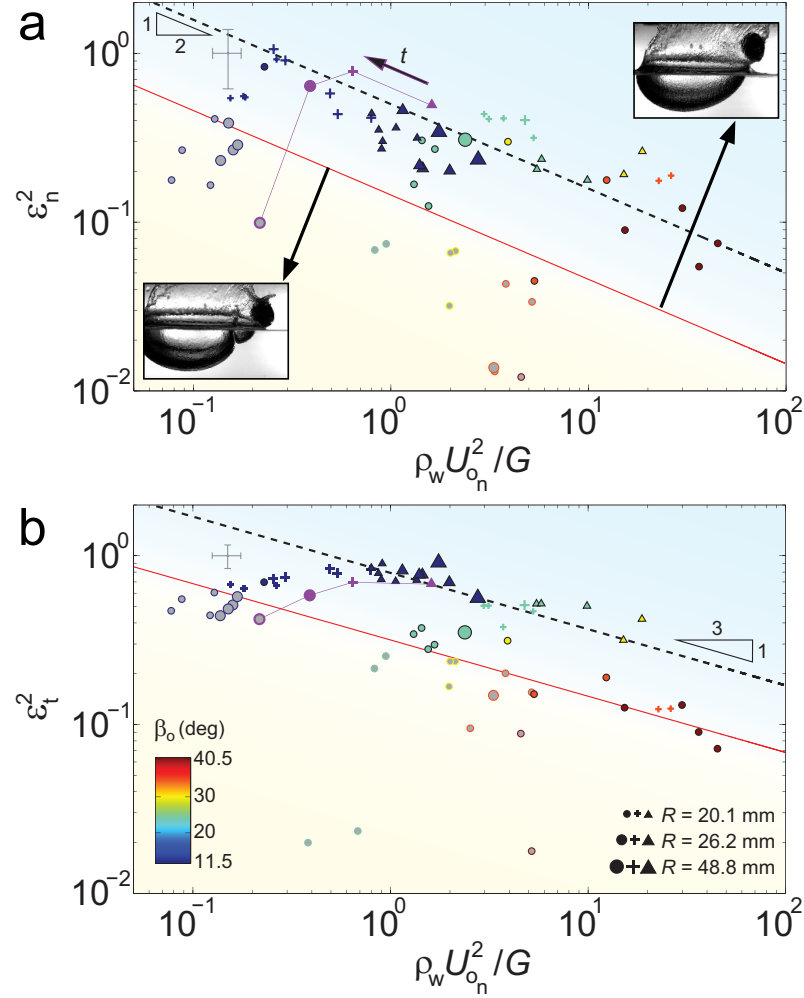


Fig. 3.7: Restitution coefficients of elastic spheres skipping on water. Experiments reveal the dependence of the square of the normal (a) and tangential (b) restitution coefficients on $\rho_w U_{on}^2 / G$ (gray symbols denote mode 1^- transitional skips; marker shapes same as for figure 6; $\rho^* = 1 \pm 0.08$). We find that ε_n^2 and ε_t^2 scale with $\rho_w U_{on}^2 / G$ in the same way that for bouncing liquid drops [11] they scale with $We_{on} = \rho_w U_{on}^2 R_d / \sigma$. Thus, shear modulus G for skipping elastic solid spheres plays the role of the Laplace pressure σ / R_d for bouncing liquid droplets. Because rebound is more efficient in the tangential direction, β_o decreases (thus becoming more favorable) with each skip. Additionally, both restitution coefficients increase with decreasing impact velocity until the sphere enters the mode 1^- skipping and transitional regimes. These two effects combine to enable multiple skip trajectories (figure 6). The demise of a multiple skip event starts when $t_c / t_w > 1$ and a matryoshka cavity forms (below red lines); ε_n^2 and ε_t^2 decrease rapidly when this occurs. This interpretation is confirmed by a multiple skip experiment; the purple markers on each plot correspond to the same multiple skip experiment that is shown in figure 6 & 8.

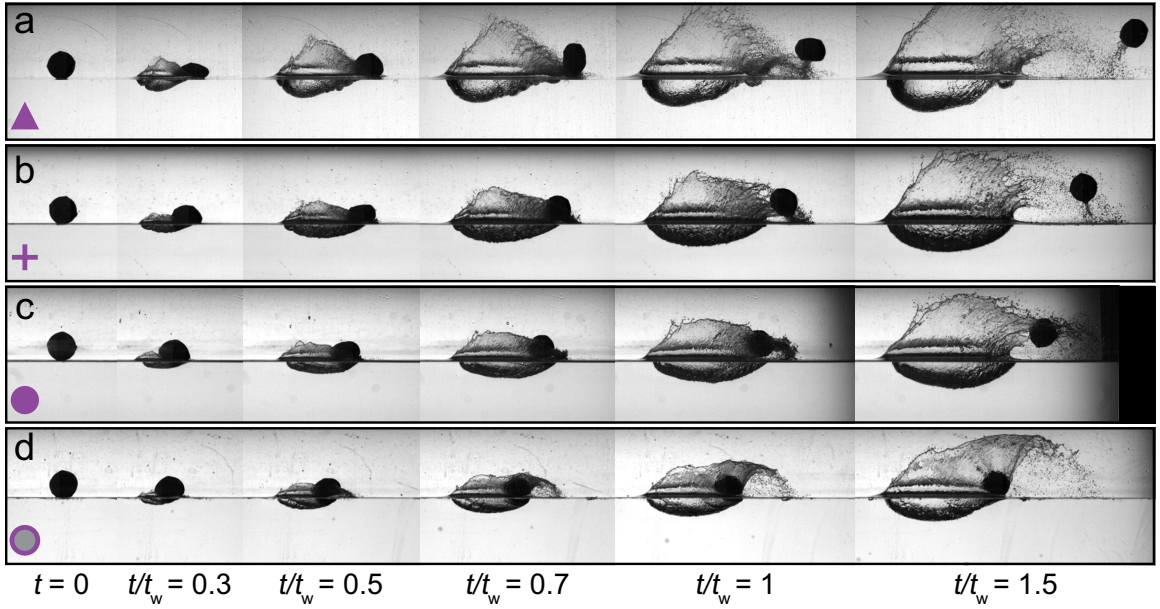


Fig. 3.8: An elastic sphere experiences several modes in a multiple skip event. In a multiple skip event, an elastic sphere experiences several skipping modes. These image sequences correspond to the four successive experimental impacts shown as purple symbols in figure 6 & 7. (a) The first skip displays mode 1^+ behaviour. (b) The impact angle β_o is reduced for the second skip, which is in the mode 2 regime. (c) The third impact (mode 1^- skipping) occurs with approximately the same value of β_o , but leads to reduced ε_n^2 and ε_t^2 . (d) The last skip shows mode 1^- transitional behaviour, and results in such small values of the restitution coefficients that the ensuing impact ends in water entry (not shown). All times are normalized by the wave time computed from the mode 1^- transitional skip (d).

3.5.1 Sphere fabrication and material properties

In order to control material properties, custom elastomeric spheres were fabricated from a high performance platinum-cure silicone rubber called Dragon Skin produced by Smooth-On, Inc., which consists of two liquid constituent parts. Once the two constituents are mixed, the material sets without requiring heat treatment. The shear modulus was varied by adding a silicone thinner to the mixture before setting, which reduces the material shear modulus by decreasing the polymer cross-linking density. Sphere materials with three different shear moduli were fabricated by adding 0, 1/3 and 1/2 parts thinner by mass ratio. Prior to setting, the liquid mixture was placed in a vacuum chamber to remove any entrained air. For our experiments, spheres were fabricated by curing the liquid mixture in smooth, machined aluminum molds to produce spheres with three different radii: 20.1 ± 0.8 mm, 26.2 ± 0.8 mm and 48.8 ± 0.9 mm. A rigid sphere with $R = 25.8 \pm 1$ mm was fabricated from Nylon DuraForm PA using selective laser sintering (SLS). The uncertainty on each sphere radius represents the 95% confidence interval based on several independent measurements. A thin Lycra casing was loosely fitted around each sphere in order to prevent undesired particles from adhering to the surface and to reduce the friction between the sphere and the launching mechanism from which it was fired.

The silicone rubber was so compliant that traditional uniaxial “dogbone” testing on our Instron machine was not feasible as the forces generated were too small to be reliably measured. To overcome this, we performed a test in which the spheres were compressed on the Instron to generate a quasi-static force-displacement curve. This test setup was then numerically modeled in Abaqus with the sphere material described by a neo-Hookean hyperelastic constitutive model, parameterized by the shear modulus G [4]. We then varied G to find the value that produced the best fit between the numerically simulated and experimentally measured force-displacement curves. The elastomeric spheres used in our experiments had shear moduli of 97.2 kPa, 28.5 kPa and 12.3 kPa corresponding to 0, 1/3 and 1/2 parts thinner, respectively. According to the manufacturer of the rigid sphere (3D Systems - Quickparts Solutions), the elastic modulus of the SLS Nylon DuraForm PA

material is 1.59×10^6 kPa, which - assuming a Poisson's ratio of 0.4 - gives a shear modulus of $G = 5.66 \times 10^5$ kPa.

3.5.2 Sphere skipping experiments and data processing

Spheres were launched at the water surface from a variable-angle, pressure-driven cannon consisting of a pressure chamber for compressed air, a sliding cylindrical piston and interchangeable barrels. Sliding the cylindrical piston allowed air to flow from the pressure chamber into the barrel, thus forcing the sphere to accelerate out of the barrel and strike the water surface with impact velocity U_o and angle β_o . Impact events were illuminated with diffuse white back lighting and filmed with either NAC GX-3 or Photron SA3 high speed cameras acquiring at 1000-2000 frames per second (fps).

The impact velocity U_o and angle β_o were measured from images of the sphere prior to water impact using a cross-correlation algorithm. The mean uncertainties on U_o and β_o are $\pm 1.09 \text{ m s}^{-1}$ and $\pm 1.75^\circ$, respectively (computed at 95% confidence level). The same algorithm was used to measure the exit velocity and angle of the sphere after lifting off the surface. Also, the rigid body rotation of the sphere was estimated after skipping by tracking reference markers on the exterior of the Lycra casing. It was found for mode 1⁻ skip types that the rotational kinetic energy was typically less than 8% of the translational kinetic energy after water exit. Furthermore, for these impacts the wave time t_w was typically less than 30% of the period of rigid body rotation measured after skipping. The collision time t_c , wave time t_w and vibration mode classification were all determined from manual inspection of the high speed images. The minimum skipping velocity U_{\min} was found experimentally by performing successive experiments with identical conditions but with increasing velocity until the sphere skipped.

3.5.3 Abaqus numerical model

Details of the Abaqus numerical model of the elastic sphere impact are contained in reference [17]; clarifications relevant for the present work are summarized here. The finite-element model uses the built in Coupled Euler-Lagrange functionality of Abaqus/Explicit,

which couples the contact region between the Lagrangian (sphere) and Eulerian (fluid) domains using a penalty method. Direct numerical simulation of the compressible Navier-Stokes equations is performed in the Eulerian domain. For the solid, conservation of momentum is solved with an incompressible neo-Hookean constitutive model describing the sphere. For all numerical model results presented herein, the mesh consists of 8-noded Eulerian hexahedral elements with spatial resolution of 3 mm. The sphere radius R , density ρ_s and shear modulus G , as well as the impact velocity U_o and angle β_o were set to match experimental values. The three-dimensional computational domain consists of a water tank (length = $30R$, depth = $6.5R$) with a symmetry plane coinciding with the plane of motion. For the numerical results presented in figure 4a, U_{\min} is the average of the impact velocities for a skipping case and the non-skipping case with the nearest U_o . The numerical marker error bars reported in figure 4a represent $\pm 1/2$ of the velocity difference between the two cases.

3.5.4 Analytical model of elastic sphere skipping

An approximate analytical approach to modeling the impact between a compliant elastic sphere and a fluid surface is outlined (for a complete derivation, see Supplement 1). Here, we describe the sphere deformation and motion using a set of reduced, scalar generalized coordinates that are governed by a system of ordinary differential equations (ODEs). We begin by defining a fixed Cartesian coordinate system $\{\mathbf{e}_1, \mathbf{e}_2, \mathbf{e}_3\}$ (figure 3a). We assume the sphere moves only in the $\mathbf{e}_1 - \mathbf{e}_2$ plane and undergoes no rigid body rotation. The sphere deformation is first described by a rigid displacement \mathbf{d} that describes the motion of the center of mass (COM) in terms of the generalized coordinates d_1, d_2 . This is followed by a volume preserving stretch \mathbf{V} that deforms the sphere into an ellipsoid. The coordinates of a material particle before deformation (\mathbf{x}) and after deformation (\mathbf{y}) are related by $\mathbf{y} = \mathbf{d} + \mathbf{V}\mathbf{x}$. The velocity and acceleration fields follow as $\mathbf{v} = \dot{\mathbf{d}} + \dot{\mathbf{V}}\mathbf{x}$ and $\mathbf{a} = \ddot{\mathbf{d}} + \ddot{\mathbf{V}}\mathbf{x}$. The stretch \mathbf{V} and its time derivatives $\dot{\mathbf{V}}, \ddot{\mathbf{V}}$ can be written in terms of the principal stretches λ_1, λ_2 and $\lambda_3 = 1/\lambda_1\lambda_2$, which are aligned with the body-fixed $\{\mathbf{m}_1, \mathbf{m}_2, \mathbf{m}_3\}$ coordinates, respectively (see figure 3a and Supplement 1). The $\{\mathbf{m}_1, \mathbf{m}_2, \mathbf{m}_3\}$ coordinate system is

inclined at attack angle α relative to the free-surface. We introduce a virtual velocity field $\delta \mathbf{v} = \delta \dot{\mathbf{d}} + \delta \dot{\mathbf{V}} \mathbf{x}$ where the kinematic variables are associated with virtual rates of change $\delta \dot{d}_1, \delta \dot{d}_2, \delta \dot{\lambda}_1, \delta \dot{\lambda}_2, \delta \dot{\alpha}$ about the current (deformed) state. The governing equations for the generalized coordinates $d_1, d_2, \lambda_1, \lambda_2$ and α are obtained from the principle of virtual work (i.e., weak form of the momentum conservation equation) [4]

$$\int_V (\sigma : \delta \mathbf{D}) dV + \int_V \rho_s (\mathbf{a} \cdot \delta \mathbf{v}) dV + \int_V \rho_s (\mathbf{b} \cdot \delta \mathbf{v}) dV - \int_A (\mathbf{t} \cdot \delta \mathbf{v}) dA = 0 \quad (3.4)$$

where σ is the Cauchy stress tensor, \mathbf{D} is the stretch rate, \mathbf{b} are body forces, \mathbf{t} are traction forces and V and A denote integration over the volume and surface of the deformed solid, respectively. The term involving the external traction can be re-written as

$$\int_A (\mathbf{t} \cdot \delta \mathbf{v}) dA = \mathbf{F} \cdot \delta \dot{\mathbf{d}} + \left[\int_A \mathbf{t} \otimes (\mathbf{y} - \mathbf{d}) dA \right] : [\delta \dot{\mathbf{V}} \mathbf{V}^{-1}] \quad (3.5)$$

where \mathbf{F} represents the resultant hydrodynamic force acting on the solid and the second term on the right hand side represents the virtual power associated with a force dipole tending to distort the elastomer. Expressing equations 3.32-3.40 in terms of the generalized coordinates (see Supplement 1) and then setting each of $\delta \dot{d}_1, \delta \dot{d}_2, \delta \dot{\lambda}_1, \delta \dot{\lambda}_2, \delta \dot{\alpha}$ to be nonzero in turn yields a set of coupled second order nonlinear ODEs in terms of general forces and

tractions:

$$\delta \dot{d}_1 : \quad \frac{4\pi R^3}{3} \rho_s \ddot{d}_1 = F_h \quad (3.6)$$

$$\delta \dot{d}_2 : \quad \frac{4\pi R^3}{3} \rho_s \ddot{d}_2 = F_v - \frac{4\pi R^3}{3} \rho_s g \quad (3.7)$$

$$\begin{aligned} \delta \dot{\alpha} : \quad & \frac{4\pi}{15} \rho_s R^5 \left[2\ddot{\alpha} (\lambda_1 - \lambda_2)^2 \right] \\ & = (\lambda_1 - \lambda_2) \int_A \left(t_1 \frac{(y_2 - d_2)}{\lambda_2} + t_2 \frac{(y_1 - d_1)}{\lambda_1} \right) dA \end{aligned} \quad (3.8)$$

$$\begin{aligned} \delta \dot{\lambda}_1 : \quad & \frac{4\pi}{15} \rho_s R^5 \left[\ddot{\lambda}_1 \left(1 + \frac{\lambda_2^2}{(\lambda_1 \lambda_2)^4} \right) + \ddot{\lambda}_2 \frac{\lambda_1 \lambda_2}{(\lambda_1 \lambda_2)^4} - 2\dot{\alpha}^2 (\lambda_1 - \lambda_2) + 2 \frac{\lambda_2 \dot{\lambda}_1 \dot{\lambda}_2}{(\lambda_1 \lambda_2)^4} \right. \\ & \quad \left. - 2 \frac{\lambda_2 (\dot{\lambda}_1 \lambda_2 + \lambda_1 \dot{\lambda}_2)^2}{(\lambda_1 \lambda_2)^5} \right] + \frac{4\pi}{3} G R^3 \left(\lambda_1 - \frac{\lambda_2}{(\lambda_1 \lambda_2)^3} \right) \\ & = \int_A \left(t_1 \frac{(y_1 - d_1)}{\lambda_1} - t_3 \frac{(y_3 - d_3)}{\lambda_1} \right) dA \end{aligned} \quad (3.9)$$

$$\begin{aligned} \delta \dot{\lambda}_2 : \quad & \frac{4\pi}{15} \rho_s R^5 \left[\ddot{\lambda}_2 \left(1 + \frac{\lambda_1^2}{(\lambda_1 \lambda_2)^4} \right) + \ddot{\lambda}_1 \frac{\lambda_1 \lambda_2}{(\lambda_1 \lambda_2)^4} - 2\dot{\alpha}^2 (\lambda_2 - \lambda_1) + 2 \frac{\lambda_1 \dot{\lambda}_1 \dot{\lambda}_2}{(\lambda_1 \lambda_2)^4} \right. \\ & \quad \left. - 2 \frac{\lambda_1 (\dot{\lambda}_1 \lambda_2 + \lambda_1 \dot{\lambda}_2)^2}{(\lambda_1 \lambda_2)^5} \right] + \frac{4\pi}{3} G R^3 \left(\lambda_2 - \frac{\lambda_1}{(\lambda_1 \lambda_2)^3} \right) \\ & = \int_A \left(t_2 \frac{(y_2 - d_2)}{\lambda_2} - t_3 \frac{(y_3 - d_3)}{\lambda_2} \right) dA \end{aligned} \quad (3.10)$$

where F_h and F_v are the horizontal and vertical force components in $\{\mathbf{e}_1, \mathbf{e}_2, \mathbf{e}_3\}$ coordinates, respectively, and t_i and y_i are the components of the traction vector and position vector on the surface of the ellipsoid in $\{\mathbf{m}_1, \mathbf{m}_2, \mathbf{m}_3\}$ coordinates, respectively.

Next, we propose an approximate model for the hydrodynamic forcing on the sphere. It is beyond the scope of this work to derive an analytical expression for the dynamic pressure distribution over the wetted sphere surface. Rather, our goal is to generate a simplified model that captures the first order sphere motion and deformation during an oblique water impact. Thus, the hydrodynamic force \mathbf{F} is computed using equation 3.1, which follows from work on skipping stones [28] by considering the deformed sphere to be a circular disk. The disk radius is described by an equivalent principal stretch λ_{eq}

computed by equating the area of the equivalent circular disk with the cross-sectional area of the deformed sphere in the $\mathbf{m}_1\text{-}\mathbf{m}_3$ plane, $\pi(\lambda_{\text{eq}}R)^2 = \pi(\lambda_1R)(R/\lambda_1\lambda_2)$, which gives $\lambda_{\text{eq}} = 1/\sqrt{\lambda_2}$. Furthermore, S_w , \mathbf{U}_B and β_B can be written in terms of the generalized coordinates describing the sphere deformation (see Supplement 1). Without describing the pressure distribution, we cannot specify the center of pressure and thus cannot define the y_1 coordinate at which the traction vector acts in equation 3.43, which governs the attack angle α . To overcome this, we determine α from our Abaqus numerical model (figure 3b). With α prescribed, the remaining ODEs for d_1 , d_2 , λ_1 and λ_2 (equations 3.41, 3.42, 3.44 & 3.45) can be solved without further simplification. Inserting the hydrodynamic force yields equation 3.59 and the remaining ODEs are:

$$\ddot{d}_1 = -\frac{3}{8\pi R^3} \frac{\rho_w}{\rho_s} |\mathbf{U}_B|^2 S_w \sin(\alpha + \beta_B) \sin \alpha \quad (3.11)$$

$$\begin{aligned} \frac{4\pi}{15} \rho_s R^5 \left[\ddot{\lambda}_1 \left(1 + \frac{\lambda_2^2}{(\lambda_1 \lambda_2)^4} \right) + \ddot{\lambda}_2 \frac{\lambda_1 \lambda_2}{(\lambda_1 \lambda_2)^4} - 2\dot{\alpha}^2 (\lambda_1 - \lambda_2) + 2 \frac{\lambda_2 \dot{\lambda}_1 \dot{\lambda}_2}{(\lambda_1 \lambda_2)^4} - 2 \frac{\lambda_2 (\dot{\lambda}_1 \lambda_2 + \lambda_1 \dot{\lambda}_2)^2}{(\lambda_1 \lambda_2)^5} \right] \\ + \frac{4\pi}{3} G R^3 \left(\lambda_1 - \frac{\lambda_2}{(\lambda_1 \lambda_2)^3} \right) = 0 \end{aligned} \quad (3.12)$$

$$\begin{aligned} \frac{4\pi}{15} \rho_s R^4 \left[\ddot{\lambda}_2 \left(1 + \frac{\lambda_1^2}{(\lambda_1 \lambda_2)^4} \right) + \ddot{\lambda}_1 \frac{\lambda_1 \lambda_2}{(\lambda_1 \lambda_2)^4} - 2\dot{\alpha}^2 (\lambda_2 - \lambda_1) + 2 \frac{\lambda_1 \dot{\lambda}_1 \dot{\lambda}_2}{(\lambda_1 \lambda_2)^4} - 2 \frac{\lambda_1 (\dot{\lambda}_1 \lambda_2 + \lambda_1 \dot{\lambda}_2)^2}{(\lambda_1 \lambda_2)^5} \right] \\ + \frac{4\pi}{3} G R^3 \left(\lambda_2 - \frac{\lambda_1}{(\lambda_1 \lambda_2)^3} \right) = -\frac{1}{2} \rho_w |\mathbf{U}_B|^2 S_w \sin(\alpha + \beta_B) \end{aligned} \quad (3.13)$$

Equations 3.59 & 3.58-3.13 are solved using a fourth-order Runge-Kutta solver in Matlab, with α and $\dot{\alpha}$ prescribed based on the Abaqus numerical model results.

3.5.5 Scaling analysis

Using U_{\min} as the characteristic velocity, $(\lambda_{\max} R)^2$ as the characteristic wetted area and $2R/t_c^2$ as the characteristic acceleration, equation 3.59 can be estimated as

$$\frac{2R}{t_c^2} \approx \frac{3}{8\pi R \rho^*} U_{\min}^2 \lambda_{\max}^2 \sin(\alpha + \beta_B) \cos \alpha - g \quad (3.14)$$

For cases that barely skip, we have observed $t_c \approx O(10^{-1})\text{s}$, which gives a characteristic acceleration of $2R/t_c^2 \approx O(1)\text{m s}^{-2}$ (with $R \approx O(10^{-2})\text{m}$). Therefore, in the case of the minimum impact velocity, we expect gravity to be an order of magnitude larger than the sphere acceleration such that

$$\frac{3}{8\pi R \rho^*} U_{\min}^2 \lambda_{\max}^2 \sin(\alpha + \beta_B) \cos \alpha \approx g \quad (3.15)$$

In the limit of small G , simulations show that $\sin(\alpha + \beta_B) \cos \alpha$ is of order 1 (see Supplement 2) and $\lambda_{\max} \propto (G/\rho_w U_{\min}^2)^{-1/3}$ (see figure 3b). Thus, equation 3.15 leads to

$$U_{\min} \propto (g \rho^* R)^{3/10} (G/\rho_w)^{1/5} \quad (3.16)$$

To determine how t_c/t_w evolves, we consider a scaling analysis of equation 3.63 when $t_c \approx t_w$, which is typically $O(10^{-2})\text{s}$ for our experiments. We find the characteristic acceleration $2R/t_c^2 \approx O(10^2)\text{m s}^{-2}$ and thus can neglect gravity. Replacing U_{\min} with U_o in equation 3.63 and solving for t_c gives $t_c \approx \frac{R}{U_o \lambda_{\max}} \sqrt{\frac{16\pi \rho^*}{3 \sin(\alpha + \beta_B) \cos \alpha}}$. Simulations show that $1/\sqrt{\sin(\alpha + \beta_B) \cos \alpha}$ is order 1 (see Supplementary Note 2). Thus, the collision time scales according to

$$t_c \propto (R/U_o \lambda_{\max}) \sqrt{\rho^*}. \quad (3.17)$$

3.6 Supplement 1: Analytical model of elastic sphere skipping

This section derives an approximate analytical approach to modeling the impact between a compliant elastomeric sphere and a fluid surface. The goal is to describe the deformation and motion using a set of reduced, scalar generalized coordinates (to be outlined)

which are governed by a system of ordinary differential equations (ODEs). We begin by defining a fixed Cartesian coordinate system with \mathbf{e}_1 parallel to the horizontal component of velocity of the sphere, \mathbf{e}_2 perpendicular to the surface of the fluid, and \mathbf{e}_3 transverse to the motion (see figure 3(a)).

We assume that the sphere is a homogeneous, isotropic, incompressible neo-Hookean solid with radius R , shear modulus G and mass density ρ_s . The sphere moves parallel to the \mathbf{e}_1 direction and we assume it undergoes no rigid body rotation. To justify this assumption, we experimentally measured the rotational and translational kinetic energy of the sphere after exiting the water for mode 1⁻ skip types; we found that the rotational kinetic energy was typically less than 8% of the translational kinetic energy. The deformation of the sphere is then described as a sequence of two deformations:

1. A rigid displacement through a vector \mathbf{d} that describes the motion of the center of mass (COM). The initial conditions, momentum conservation and symmetry require that $d_3 = 0$ throughout the motion.
2. A volume preserving stretch \mathbf{V} that deforms the sphere into an ellipsoid. By symmetry, one of the principal directions of stretch must be parallel to the \mathbf{e}_3 direction. The other two principal stretch directions are parallel to unit vectors $\mathbf{m}_1, \mathbf{m}_2$, which lie in the vertical plane (see figure 3(a)). We let α be the angle between the \mathbf{m}_1 and \mathbf{e}_1 directions (positive α corresponds to rotation of the principal stretch directions about the \mathbf{m}_3 axis); thus α describes the attack angle of the ellipsoid. We introduce the principal stretches λ_1, λ_2 and $\lambda_3 = 1/\lambda_1\lambda_2$. The coordinates of a material particle in the sphere before deformation are given by \mathbf{x} , and \mathbf{y} defines the coordinates after deformation.

The following identities are useful for further calculations. Elementary trigonometry shows that the unit vectors \mathbf{e}_i and \mathbf{m}_i are related by

$$\mathbf{e}_i = \mathbf{P}\mathbf{m}_i \tag{3.18}$$

where \mathbf{P} is a proper orthogonal tensor whose components in both the basis $\{\mathbf{e}_1, \mathbf{e}_2, \mathbf{e}_3\}$ and $\{\mathbf{m}_1, \mathbf{m}_2, \mathbf{m}_3\}$ can be expressed as a matrix

$$[\mathbf{P}] = \begin{bmatrix} \cos \alpha & -\sin \alpha & 0 \\ \sin \alpha & \cos \alpha & 0 \\ 0 & 0 & 1 \end{bmatrix} \quad (3.19)$$

Since \mathbf{e}_i are independent of time, derivatives of the vectors \mathbf{m}_i can be calculated as

$$\dot{\mathbf{m}}_i = \frac{d}{dt} \mathbf{P}^T \mathbf{e}_i \quad (3.20)$$

Since \mathbf{P} is orthogonal it follows that

$$\mathbf{P}\mathbf{P}^T = \mathbf{I} \implies \frac{d\mathbf{P}}{dt} \mathbf{P}^T + \mathbf{P} \frac{d\mathbf{P}^T}{dt} = 0 \implies \frac{d\mathbf{P}^T}{dt} = -\mathbf{P}^T \frac{d\mathbf{P}}{dt} \mathbf{P}^T \quad (3.21)$$

Substituting this result into equation 3.20 and making use of equation 3.18 yields

$$\dot{\mathbf{m}}_i = \mathbf{P}^T \frac{d\mathbf{P}}{dt} \mathbf{m}_i \quad (3.22)$$

Evaluating this expression shows that

$$\begin{aligned} \dot{\mathbf{m}}_1 &= \dot{\alpha} \mathbf{m}_2 \\ \dot{\mathbf{m}}_2 &= -\dot{\alpha} \mathbf{m}_1 \\ \dot{\mathbf{m}}_3 &= 0 \end{aligned} \quad (3.23)$$

The standard definition of principal stretches implies that the volume preserving stretch \mathbf{V} can be expressed as

$$\mathbf{V} = \lambda_1 \mathbf{m}_1 \otimes \mathbf{m}_1 + \lambda_2 \mathbf{m}_2 \otimes \mathbf{m}_2 + \frac{1}{\lambda_1 \lambda_2} \mathbf{m}_3 \otimes \mathbf{m}_3 \quad (3.24)$$

where $\mathbf{a} \otimes \mathbf{b}$ denotes the tensor product of two vectors; i.e the operator with the property

that $[\mathbf{a} \otimes \mathbf{b}] \cdot \mathbf{c} = (\mathbf{b} \cdot \mathbf{c}) \mathbf{a}$ for all vectors \mathbf{c} . Taking the time derivative of this expression and using equation 3.23 then shows that

$$\begin{aligned} \dot{\mathbf{V}} &= \dot{\lambda}_1 \mathbf{m}_1 \otimes \mathbf{m}_1 - \frac{\dot{\lambda}_1 \lambda_2 + \lambda_1 \dot{\lambda}_2}{(\lambda_1 \lambda_2)^2} \mathbf{m}_3 \otimes \mathbf{m}_3 + \dot{\lambda}_2 \mathbf{m}_2 \otimes \mathbf{m}_2 \\ &+ (\lambda_1 - \lambda_2) \dot{\alpha} (\mathbf{m}_2 \otimes \mathbf{m}_1 + \mathbf{m}_1 \otimes \mathbf{m}_2) \end{aligned} \quad (3.25)$$

and

$$\begin{aligned} \ddot{\mathbf{V}} &= \ddot{\lambda}_1 \mathbf{m}_1 \otimes \mathbf{m}_1 - \frac{\ddot{\lambda}_1 \lambda_2 + \lambda_1 \ddot{\lambda}_2}{(\lambda_1 \lambda_2)^2} \mathbf{m}_3 \otimes \mathbf{m}_3 + \ddot{\lambda}_2 \mathbf{m}_2 \otimes \mathbf{m}_2 + (\lambda_1 - \lambda_2) \ddot{\alpha} (\mathbf{m}_2 \otimes \mathbf{m}_1 + \mathbf{m}_1 \otimes \mathbf{m}_2) \\ &+ \left(\frac{2 (\dot{\lambda}_1 \lambda_2 + \lambda_1 \dot{\lambda}_2)^2}{(\lambda_1 \lambda_2)^3} - \frac{2 \dot{\lambda}_1 \dot{\lambda}_2}{(\lambda_1 \lambda_2)^2} \right) \mathbf{m}_3 \otimes \mathbf{m}_3 - 2 (\lambda_1 - \lambda_2) \dot{\alpha}^2 (\mathbf{m}_1 \otimes \mathbf{m}_1 - \mathbf{m}_2 \otimes \mathbf{m}_2) \\ &+ (\dot{\lambda}_1 - \dot{\lambda}_2) \dot{\alpha} (\mathbf{m}_2 \otimes \mathbf{m}_1 + \mathbf{m}_1 \otimes \mathbf{m}_2) \end{aligned} \quad (3.26)$$

The coordinates d_1 and d_2 describe the rigid body motion and λ_1 , λ_2 and α describe the deformation of the sphere. Our goal is to calculate equations of motion for these generalized coordinates. With this description we can write the deformation mapping as

$$\mathbf{y} = \mathbf{d} + \mathbf{V} \mathbf{x} \quad (3.27)$$

The velocity and acceleration fields follow as

$$\mathbf{v} = \dot{\mathbf{d}} + \dot{\mathbf{V}} \mathbf{x} \quad (3.28)$$

$$\mathbf{a} = \ddot{\mathbf{d}} + \ddot{\mathbf{V}} \mathbf{x} \quad (3.29)$$

We introduce a virtual velocity field

$$\delta \mathbf{v} = \delta \dot{\mathbf{d}} + \delta \dot{\mathbf{V}} \mathbf{x} \quad (3.30)$$

where the kinematic variables are associated with virtual rates of change $\delta \dot{d}_1$, $\delta \dot{d}_2$, $\delta \dot{\lambda}_1$, $\delta \dot{\lambda}_2$, $\delta \dot{\alpha}$ about the current (deformed) state. The governing equations for d_1 , d_2 , λ_1 , λ_2 and α are

obtained from the principle of virtual work (i.e., weak form of the momentum conservation equation) [4]

$$\int_V (\boldsymbol{\sigma} : \delta \mathbf{D}) dV + \int_V \rho_s (\mathbf{a} \cdot \delta \mathbf{v}) dV + \int_V \rho_s (\mathbf{b} \cdot \delta \mathbf{v}) dV - \int_A (\mathbf{t} \cdot \delta \mathbf{v}) dA = 0 \quad (3.31)$$

or, in index notation,

$$\int_V \sigma_{ij} \delta D_{ij} dV + \int_V \rho_s a_i \delta v_i dV + \int_V \rho_s b_i \delta v_i dV - \int_A t_i \delta v_i dA = 0 \quad (3.32)$$

where b_i represents body forces, t_i are traction forces (i.e., applied to the sphere boundary) and V and A denote integration over the volume and surface of the deformed solid, respectively. The stretch rate in the solid is given by

$$D_{ij} = \frac{1}{2} \left(\frac{\partial v_i}{\partial y_j} + \frac{\partial v_j}{\partial y_i} \right) \quad (3.33)$$

The first term in equation 3.32 is the virtual rate of change of strain energy in the sphere, which can be calculated directly as

$$\int_V \sigma_{ij} \delta D_{ij} dV = \frac{4\pi}{3} G R^3 \left(\lambda_1 \delta \dot{\lambda}_1 + \lambda_2 \delta \dot{\lambda}_2 - \frac{\lambda_1 \delta \dot{\lambda}_2 + \lambda_2 \delta \dot{\lambda}_1}{(\lambda_1 \lambda_2)^3} \right) \quad (3.34)$$

To evaluate the remaining terms, the following identities are useful

$$\begin{aligned} \int_{V_0} dV_0 &= \frac{4\pi}{3} R^3 \\ \int_{V_0} x_i dV_0 &= 0 \\ \int_{V_0} x_i x_j dV_0 &= \frac{4\pi}{15} R^5 \delta_{ij} \end{aligned} \quad (3.35)$$

where x_i denote the coordinates of a material particle with respect to the center of the sphere and the integrals are evaluated over the undeformed sphere. Thus,

$$\int_V \rho_s b_i \delta v_i dV = \int_{V_0} \rho_s b_i \delta v_i dV_0 = -g\rho_s \frac{4\pi R^3}{3} \delta \dot{d}_2 \quad (3.36)$$

where we have made use of incompressibility to convert the integral over the volume of the deformed sphere (V) to an integral over the volume of the undeformed sphere (V_0). Also, we have noted that $b_i = -\rho_s g \delta_{i2}$, have substituted equation 3.30 for δv_i and have made use of the first two integrals in equation 3.35. Using equations 3.29-3.30 and again imposing incompressibility, the inertia term can be expressed as

$$\int_V \rho_s a_i \delta v_i dV = \int_{V_0} \rho_s a_i \delta v_i dV_0 = \int_{V_0} \rho_s [\ddot{\mathbf{d}} + \ddot{\mathbf{V}}\mathbf{x}] \cdot [\delta \dot{\mathbf{d}} + \delta \dot{\mathbf{V}}\mathbf{x}] dV_0 \quad (3.37)$$

Expanding the terms on the right hand side yields

$$\begin{aligned} \int_{V_0} \rho_s \ddot{\mathbf{d}} \delta \dot{\mathbf{d}} dV_0 &= \frac{4\pi \rho_s R^3}{3} (\ddot{d}_1 \delta \dot{d}_1 + \ddot{d}_2 \delta \dot{d}_2) \\ \int_{V_0} \rho_s [\ddot{\mathbf{V}}\mathbf{x}] \cdot \delta \dot{\mathbf{d}} dV_0 &= \int_{V_0} \rho_s \ddot{\mathbf{d}} \cdot [\delta \dot{\mathbf{V}}\mathbf{x}] dV_0 = 0 \\ \int_{V_0} \rho_s [\ddot{\mathbf{V}}\mathbf{x}] \cdot [\delta \dot{\mathbf{V}}\mathbf{x}] dV_0 &= \frac{8\pi}{15} \rho_s R^5 [\ddot{\mathbf{V}}\mathbf{V} : \delta \dot{\mathbf{V}}\mathbf{V}^{-1}] \end{aligned} \quad (3.38)$$

The nonzero terms can be interpreted physically as rates of change of translational and vibrational kinetic energies.

Finally, consider the term involving the external traction, which represents the pressure applied by the fluid on the elastomer surface,

$$\int_A t_i \delta v_i dA = \int_A \mathbf{t} \cdot [\delta \dot{\mathbf{d}} + \delta \dot{\mathbf{V}}\mathbf{x}] dA \quad (3.39)$$

It is preferable to express the integrand in terms of spatial coordinates. Note that from equation 3.27 we have $\mathbf{x} = \mathbf{V}^{-1}(\mathbf{y} - \mathbf{d})$ so that

$$\begin{aligned} \int_A t_i \delta v_i dA &= \int_A \mathbf{t} \cdot [\delta \dot{\mathbf{d}} + \delta \dot{\mathbf{V}} \mathbf{V}^{-1}(\mathbf{y} - \mathbf{d})] dA \\ &= \mathbf{F} \cdot \delta \dot{\mathbf{d}} + \left[\int_A \mathbf{t} \otimes (\mathbf{y} - \mathbf{d}) dA \right] : [\delta \dot{\mathbf{V}} \mathbf{V}^{-1}] \end{aligned} \quad (3.40)$$

Here, \mathbf{F} represents the resultant hydrodynamic force acting on the solid and the second term on the right hand side represents the virtual power associated with a force dipole tending to distort the elastomer.

Equation 3.32 can now be expressed in terms of the generalized coordinates. Substituting the expressions of equations 3.24-3.26 into equations 3.34,3.36-3.38 and 3.40, then setting each of $\delta \dot{d}_1$, $\delta \dot{d}_2$, $\delta \dot{\lambda}_1$, $\delta \dot{\lambda}_2$, $\delta \dot{\alpha}$ to be nonzero in turn will yield a set of coupled second order nonlinear ODEs. Working through this procedure yields the following governing

equations:

$$\delta \dot{d}_1 : \quad \frac{4\pi R^3}{3} \rho_s \ddot{d}_1 = F_h \quad (3.41)$$

$$\delta \dot{d}_2 : \quad \frac{4\pi R^3}{3} \rho_s \ddot{d}_2 = F_v - \frac{4\pi R^3}{3} \rho_s g \quad (3.42)$$

$$\begin{aligned} \delta \dot{\alpha} : \quad & \frac{4\pi}{15} \rho_s R^5 \left[2\ddot{\alpha} (\lambda_1 - \lambda_2)^2 \right] \\ & = (\lambda_1 - \lambda_2) \int_A \left(t_1 \frac{(y_2 - d_2)}{\lambda_2} + t_2 \frac{(y_1 - d_1)}{\lambda_1} \right) dA \end{aligned} \quad (3.43)$$

$$\begin{aligned} \delta \dot{\lambda}_1 : \quad & \frac{4\pi}{15} \rho_s R^5 \left[\ddot{\lambda}_1 \left(1 + \frac{\lambda_2^2}{(\lambda_1 \lambda_2)^4} \right) + \ddot{\lambda}_2 \frac{\lambda_1 \lambda_2}{(\lambda_1 \lambda_2)^4} - 2\dot{\alpha}^2 (\lambda_1 - \lambda_2) + 2 \frac{\lambda_2 \dot{\lambda}_1 \dot{\lambda}_2}{(\lambda_1 \lambda_2)^4} \right. \\ & \quad \left. - 2 \frac{\lambda_2 (\dot{\lambda}_1 \lambda_2 + \lambda_1 \dot{\lambda}_2)^2}{(\lambda_1 \lambda_2)^5} \right] + \frac{4\pi}{3} G R^3 \left(\lambda_1 - \frac{\lambda_2}{(\lambda_1 \lambda_2)^3} \right) \\ & = \int_A \left(t_1 \frac{(y_1 - d_1)}{\lambda_1} - t_3 \frac{(y_3 - d_3)}{\lambda_1} \right) dA \end{aligned} \quad (3.44)$$

$$\begin{aligned} \delta \dot{\lambda}_2 : \quad & \frac{4\pi}{15} \rho_s R^5 \left[\ddot{\lambda}_2 \left(1 + \frac{\lambda_1^2}{(\lambda_1 \lambda_2)^4} \right) + \ddot{\lambda}_1 \frac{\lambda_1 \lambda_2}{(\lambda_1 \lambda_2)^4} - 2\dot{\alpha}^2 (\lambda_2 - \lambda_1) + 2 \frac{\lambda_1 \dot{\lambda}_1 \dot{\lambda}_2}{(\lambda_1 \lambda_2)^4} \right. \\ & \quad \left. - 2 \frac{\lambda_1 (\dot{\lambda}_1 \lambda_2 + \lambda_1 \dot{\lambda}_2)^2}{(\lambda_1 \lambda_2)^5} \right] + \frac{4\pi}{3} G R^3 \left(\lambda_2 - \frac{\lambda_1}{(\lambda_1 \lambda_2)^3} \right) \\ & = \int_A \left(t_2 \frac{(y_2 - d_2)}{\lambda_2} - t_3 \frac{(y_3 - d_3)}{\lambda_2} \right) dA \end{aligned} \quad (3.45)$$

where F_h and F_v are the horizontal and vertical force components in $\{\mathbf{e}_1, \mathbf{e}_2, \mathbf{e}_3\}$ coordinates, respectively; t_i and y_i are the components of the traction vector and position vector on the surface of the ellipsoid in $\{\mathbf{m}_1, \mathbf{m}_2, \mathbf{m}_3\}$ coordinates, respectively. Note that the translational degrees-of-freedom (DOF) decouple; they are coupled to vibration through the fluid, as we will show.

Before seeking a suitable expression for the hydrodynamic loading on the elastomer, we note that the governing equations predict vibration modes involving the propagation of a circumferential wave, which we have classified experimentally as mode 1^- and mode 1^+ (see figure 2). To see this, note that a steady-state solution exists with all tractions vanishing, and all time derivatives and second time derivatives vanishing except for the

rotation rate of the $\{\mathbf{m}_1, \mathbf{m}_2, \mathbf{m}_3\}$ axes, $\dot{\alpha}$. All governing equations are satisfied trivially except for equations 3.44-3.45, which give

$$\frac{4\pi}{15}\rho_s R^5 [-2\dot{\alpha}^2 (\lambda_1 - \lambda_2)] + \frac{4\pi}{3}GR^3 \left(\lambda_1 - \frac{\lambda_2}{(\lambda_1 \lambda_2)^3} \right) = 0 \quad (3.46)$$

and

$$\frac{4\pi}{15}\rho_s R^5 [-2\dot{\alpha}^2 (\lambda_2 - \lambda_1)] + \frac{4\pi}{3}GR^3 \left(\lambda_2 - \frac{\lambda_1}{(\lambda_1 \lambda_2)^3} \right) = 0 \quad (3.47)$$

These are satisfied by any solution in which $\lambda_1 = 1/\lambda_2 = \lambda$ (other solutions are unphysical), in which case equations 3.46 & 3.47 both reduce to

$$\frac{4\pi}{15}\rho_s R^5 \left[-2\dot{\alpha}^2 \left(\lambda - \frac{1}{\lambda} \right) \right] + \frac{4\pi}{3}GR^3 \left(\lambda - \frac{1}{\lambda} \right) = 0 \quad (3.48)$$

The angular velocity of the axes follows as

$$\dot{\alpha} = \pm \frac{1}{R} \sqrt{\frac{5G}{2\rho_s}} \quad (3.49)$$

This provides the basis for the scaling of the attack angle α as measured from the Abaqus numerical simulations (figure 3(b)) as well as the scaling of the wave time t_w measured experimentally (figure 11).

It is beyond the scope of this effort to derive an analytical expression for the dynamic pressure distribution over the wetted sphere surface. Rather, our goal is to generate a simplified analytical model that captures the first order effects of an oblique water impact using the framework just derived. Even though the large degree of freedom Abaqus model has been shown to accurately capture the sphere and fluid response (see figure 2), a simplified model is sought to gain intuition into the dominant physics and to serve as a rapid simulation tool. Therefore, we make the following simplifying assumptions in order to specify \mathbf{F} and the force dipole in terms of the shape of the elastomer and its motion:

1. The hydrodynamic force \mathbf{F} is computed by considering the deformed sphere to be a circular disk described by an equivalent principal stretch λ_{eq} (to be defined), as

shown in figure 3(a). This assumption allows for computation of \mathbf{F} based on an existing force model for rigid circular disk water impact (i.e., stone skipping) [28]. This model neglects viscous and surface tension forces, and is thus suitable when the Reynolds number $\text{Re} = U_o R / \nu \gg 1$ and Weber number $\text{We} = \rho_w U_o^2 R / \sigma \gg 1$, where ν and σ are the kinematic viscosity and surface tension of water. Like skipping stones, our sphere impacts are in this inertia-dominated regime.

2. In this disk model, the resultant hydrodynamic force acts only in the \mathbf{m}_2 direction [28].
3. Without describing the pressure distribution, we cannot specify the center of pressure and thus cannot define the y_1 coordinate at which the traction vector acts in equation 3.43, which governs the attack angle α . To overcome this, we determine α from our Abaqus numerical model. With α prescribed, equations 3.41, 3.42, 3.44 & 3.45 can be solved without further simplification.

To implement the first assumption, we define λ_{eq} by equating the area of the equivalent circular disk with the cross-sectional area of the deformed sphere in the \mathbf{m}_1 - \mathbf{m}_3 plane, $\pi(\lambda_{\text{eq}} R)^2 = \pi(\lambda_1 R)(\lambda_3 R)$, which gives $\lambda_{\text{eq}} = 1/\sqrt{\lambda_2}$ (figure 3(a)). We can then modify the expression for the resultant hydrodynamic force on a rigid circular disk [28] to give

$$\mathbf{F} = \frac{1}{2} \rho_w |\mathbf{U}_B|^2 S_w \sin(\alpha + \beta_B) \mathbf{m}_2 \quad (3.50)$$

where $\mathbf{u}_B = (u_B, v_B, w_B)^T$ is the velocity of the point B with coordinates $(m_{1_B}, m_{2_B}, m_{3_B}) = (0, -\lambda_2 R, 0)$ on the bottom surface of the ball and the angle $\beta_B = -\tan^{-1}(v_B/u_B)$ defines the instantaneous direction of \mathbf{u}_B (figure 3(a)). The wetted area S_w is defined by the submerged portion of the equivalent circular disk and is computed with respect to the still free-surface. Note that α is defined as positive counter-clockwise from the \mathbf{e}_1 axis and β_B is positive clockwise from the \mathbf{e}_1 axis. The force is assumed to act through the COM of the deformed sphere and is non-zero only when $\beta_B > -\alpha$.

Next, we express $|\mathbf{U}_B|$, β_B and S_w in terms of the kinematics of the deformed ball. Evaluating equation 3.28 gives the velocity of point B in $\{\mathbf{e}_1, \mathbf{e}_2, \mathbf{e}_3\}$ coordinates,

$$\mathbf{U}_B = \dot{\mathbf{d}} + \mathbf{P}\dot{\mathbf{V}}\mathbf{x}_B \quad (3.51)$$

where $\mathbf{x}_B = (0, -R, 0)^T$ in $\{\mathbf{m}_1, \mathbf{m}_2, \mathbf{m}_3\}$ coordinates and multiplication by \mathbf{P} takes $\dot{\mathbf{V}}\mathbf{x}_B$ to $\{\mathbf{e}_1, \mathbf{e}_2, \mathbf{e}_3\}$ coordinates. Applying the identities in equations 3.18-3.26 gives

$$\mathbf{U}_B = \begin{pmatrix} u_B \\ v_B \\ w_B \end{pmatrix} = \begin{pmatrix} \dot{d}_1 - R(\dot{\alpha}(\lambda_1 - \lambda_2)\cos\alpha - \dot{\lambda}_2\sin\alpha) \\ \dot{d}_2 - R(\dot{\alpha}(\lambda_1 - \lambda_2)\sin\alpha + \dot{\lambda}_2\cos\alpha) \\ 0 \end{pmatrix} \quad (3.52)$$

The angle of the velocity vector at B is then

$$\beta_B = -\tan^{-1}\left(\frac{v_B}{u_B}\right) = -\tan^{-1}\left(\frac{\dot{d}_2 - R(\dot{\alpha}(\lambda_1 - \lambda_2)\sin\alpha + \dot{\lambda}_2\cos\alpha)}{\dot{d}_1 - R(\dot{\alpha}(\lambda_1 - \lambda_2)\cos\alpha - \dot{\lambda}_2\sin\alpha)}\right) \quad (3.53)$$

The wetted area follows from the derivation for a rigid disk [28],

$$S_w = (\lambda_{eq}R)^2 \left[\cos^{-1}\left(1 - \frac{s}{\lambda_{eq}R}\right) - \left(1 - \frac{s}{\lambda_{eq}R}\right) \sqrt{1 - \left(1 - \frac{s}{\lambda_{eq}R}\right)^2} \right] \quad (3.54)$$

where s is the wetted length in the \mathbf{e}_1 - \mathbf{e}_2 plane (figure 3(a)) defined as

$$s = \begin{cases} 0 & \text{if } d_2 \geq R(\lambda_{eq}\sin\alpha + \lambda_2\cos\alpha) \\ -d_2/\sin\alpha + R(\lambda_{eq} + \lambda_2\cot\alpha) & \text{else} \\ 2\lambda_{eq}R & \text{if } d_2 \leq -R(\lambda_{eq}\sin\alpha - \lambda_2\cos\alpha) \end{cases} \quad (3.55)$$

Finally, to complete the simplified model we prescribe α based on the results from simulations using our numerical Abaqus model over a range of U_o and β_o with the following sphere properties: $R = 25.4$ mm, $\rho^* = 1.05$ and varying shear modulus ($G = 12.3, 28.5$ and

97.2 kPa). Recognizing that this approach is only useful if a general model for α can be established, we seek a suitable scaling of the data from simulations of mode 1⁻ skipping and mode 1⁻ transitional events. Given the angular rate of mode 1⁻ predicted by equation 3.49, we expect the attack angle to scale as $\alpha \propto t \frac{1}{R} \sqrt{\frac{G}{\rho_s}} \equiv t^*$. Figure 3b shows good collapse using this scaling, particularly for $\beta_o \leq 29.5^\circ$. For these angles, we apply the following piecewise linear model for α :

$$\alpha = \begin{cases} \frac{A_1 \sin \beta_o}{t_1^*} t^* & t^* < t_1^* \\ A_2 (t^* - t_1^*) + A_1 \sin \beta_o & t_1^* \leq t^* < t_2^* \\ A_3 (t^* - t_2^*) + A_2 (t_2^* - t_1^*) + A_1 \sin \beta_o & t_2^* \leq t^* < t_3^* \\ A_4 \sin \beta_o (t^* - t_3^*) + A_3 (t_3^* - t_2^*) + A_2 (t_2^* - t_1^*) + A_1 \sin \beta_o & t^* > t_3^* \end{cases} \quad (3.56)$$

where the coefficients A_i are found from fits to the data ($A_1 = 0.332$, $A_2 = 0.446$, $A_3 = 0.118$, $A_4 = 0.686$) in each region defined by the dimensionless times $t_1^* = 0.15$, $t_2^* = 1$ and $t_3^* = 2$. The first and last regions are β_o -dependent, while the middle two regions are independent of β_o but feature a slope change at $t^* = 1$. Applying this fit to the data shown in figure 3(b), we find a standard error of the fit of $\pm 2.35^\circ$.

For simulation data with $\beta_o \geq 34.5^\circ$, we find a dependence on $G^* = G/\rho_w U_o^2$ for $t_1^* \leq t^* < t_2^*$. For these angles, the piecewise linear model for α is given by,

$$\alpha = \begin{cases} \frac{A_1 \sin \beta_o}{t_1^*} t^* & t^* < t_1^* \\ (A_2 + C_2 \sin \beta_o / G^{*a}) (t^* - t_1^*) + A_1 \sin \beta_o & t_1^* \leq t^* < t_2^* \\ C_3 (t^* - t_2^*) + (A_2 + C_2 \sin \beta_o / G^{*a}) (t_2^* - t_1^*) + A_1 \sin \beta_o & t_2^* \leq t^* < t_3^* \\ C_4 (t^* - t_3^*) + C_3 (t_3^* - t_2^*) + (A_2 + C_2 \sin \beta_o / G^{*a}) (t_2^* - t_1^*) + A_1 \sin \beta_o & t^* > t_3^* \end{cases} \quad (3.57)$$

where the parameters are found from fits to the data in each region defined by the same dimensionless times as used for equation 3.56 ($a = 1.04$, $C_2 = 0.0219$, $C_3 = 0.108$, $C_4 = 0.324$). The standard error of this model fit to the numerical data is $\pm 4.81^\circ$.

The value of α and $\dot{\alpha}$ in equations 3.44, 3.45, 3.50 & 3.52-3.55 are computed using the models in equations 3.56 & 3.57. As our numerical simulations leave a gap for $29.5^\circ < \beta_o < 34.5^\circ$, we use equation 3.56 for $\beta_o \leq 32^\circ$ and equation 3.57 else.

We now insert the hydrodynamic force (equation 3.50) into the general equations of motion (equations 3.41, 3.42, 3.44 & 3.45). Inserting the force components $F_h = -|\mathbf{F}| \sin \alpha$ and $F_v = |\mathbf{F}| \cos \alpha$ into equations 3.41 & 3.42 gives

$$\ddot{d}_1 = -\frac{3}{8\pi R^3} \frac{\rho_w}{\rho_s} |\mathbf{U}_B|^2 S_w \sin(\alpha + \beta_B) \sin \alpha \quad (3.58)$$

$$\ddot{d}_2 = \frac{3}{8\pi R^3} \frac{\rho_w}{\rho_s} |\mathbf{U}_B|^2 S_w \sin(\alpha + \beta_B) \cos \alpha - g \quad (3.59)$$

Per our assumption that the only traction is in the \mathbf{m}_2 direction, equation 3.44 reduces to

$$\begin{aligned} \frac{4\pi}{15} \rho_s R^5 \left[\ddot{\lambda}_1 \left(1 + \frac{\lambda_2^2}{(\lambda_1 \lambda_2)^4} \right) + \ddot{\lambda}_2 \frac{\lambda_1 \lambda_2}{(\lambda_1 \lambda_2)^4} - 2\dot{\alpha}^2 (\lambda_1 - \lambda_2) + 2 \frac{\lambda_2 \dot{\lambda}_1 \dot{\lambda}_2}{(\lambda_1 \lambda_2)^4} - 2 \frac{\lambda_2 (\dot{\lambda}_1 \lambda_2 + \lambda_1 \dot{\lambda}_2)^2}{(\lambda_1 \lambda_2)^5} \right] \\ + \frac{4\pi}{3} G R^3 \left(\lambda_1 - \frac{\lambda_2}{(\lambda_1 \lambda_2)^3} \right) = 0 \end{aligned} \quad (3.60)$$

To express the forcing term in equation 3.45, we apply the point force $\mathbf{F} = |\mathbf{F}| \mathbf{m}_2$ at $y_2^* = d_2 - \lambda_2 R$. The right-hand side of equation 3.45 can be written as

$$\int_A t_2 \frac{y_2 - d_2}{\lambda_2} dA = \int_A |\mathbf{F}| \delta(y_2 - y_2^*) \frac{y_2 - d_2}{\lambda_2} dA = |\mathbf{F}| \frac{y_2^* - d_2}{\lambda_2} = -|\mathbf{F}| R \quad (3.61)$$

Combining this result with equations 3.45 & 3.50 gives

$$\begin{aligned} \frac{4\pi}{15} \rho_s R^4 \left[\ddot{\lambda}_2 \left(1 + \frac{\lambda_1^2}{(\lambda_1 \lambda_2)^4} \right) + \ddot{\lambda}_1 \frac{\lambda_1 \lambda_2}{(\lambda_1 \lambda_2)^4} - 2\dot{\alpha}^2 (\lambda_2 - \lambda_1) + 2 \frac{\lambda_1 \dot{\lambda}_1 \dot{\lambda}_2}{(\lambda_1 \lambda_2)^4} - 2 \frac{\lambda_1 (\dot{\lambda}_1 \lambda_2 + \lambda_1 \dot{\lambda}_2)^2}{(\lambda_1 \lambda_2)^5} \right] \\ + \frac{4\pi}{3} G R^3 \left(\lambda_2 - \frac{\lambda_1}{(\lambda_1 \lambda_2)^3} \right) = -\frac{1}{2} \rho_w |\mathbf{U}_B|^2 S_w \sin(\alpha + \beta_B) \end{aligned} \quad (3.62)$$

The four governing ODEs (equations 3.58-3.60 & 3.62) are solved using a fourth-order Runge-Kutta solver in Matlab, with \mathbf{U}_B , β_B and S_w defined by equations 3.52-3.55, and α ,

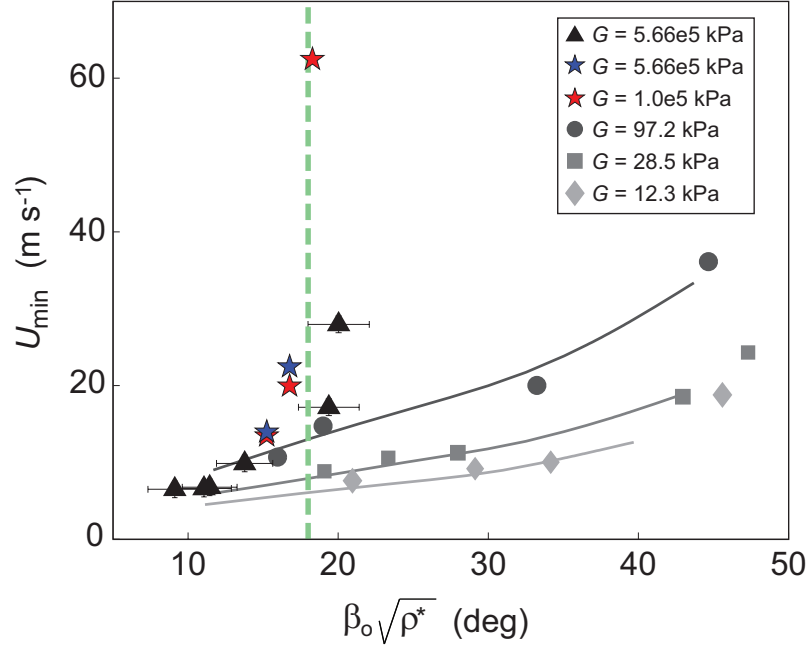


Fig. 3.9: Elastic spheres skip at much larger impact angles than rigid spheres. Markers result from experimental measurement with rigid spheres (black triangles: $R = 25.8 \text{ mm}$, $\rho^* = \rho_s/\rho_w = 0.959$) and elastic spheres ($R = 26.2 \text{ mm}$; diamonds: $\rho^* = 0.937$, squares: $\rho^* = 1.03$, circles: $\rho^* = 1.03$). The coloured star markers result from Abaqus simulations ($R = 26.4 \text{ mm}$, $\rho^* = 1.03$). The solid gray curves result from our analytical model (see Methods section). The vertical line denotes the predicted maximum $\beta_{\text{Omax}}\sqrt{\rho^*} = 18^\circ$, below which rigid spheres will skip. The numerical results follow this predicted bound. The experimental data seem to follow the same trend, albeit at larger values of $\beta_o\sqrt{\rho^*}$ than predicted; the bounding value of $\beta_{\text{Omax}}\sqrt{\rho^*} = 18^\circ$ is nonetheless within the experimental uncertainty. The experiments also suggest a lower bound for U_{\min} as $\beta_o\sqrt{\rho^*}$ decreases. This inferred value sets the lower boundary of the rigid skipping regime on Fig. 4.

$\dot{\alpha}$ defined by either equation 3.56 or 3.57, depending on the value of β_o .

3.7 Supplement 2: Typical values and scaling analysis

As shown in the Methods section, a scaled version of equation 3.59 can be estimated as

$$\frac{2R}{t_c^2} \approx \frac{3}{8\pi R \rho^*} U_{\min}^2 \lambda_{\max}^2 \sin(\alpha + \beta_B) \cos \alpha - g \quad (3.63)$$

We examine terms in equation 3.63 using representative values for a sphere that barely skips and has small G for which we expect $\dot{\alpha} \propto \frac{1}{R} \sqrt{\frac{G}{\rho_s}} \rightarrow 0$. A typical simulation using the analytical model with a relatively small shear modulus $G = 1 \text{ kPa}$ and sphere properties

$R = 26.4$ mm and $\rho_s = 1032$ kg m⁻³ gives a mean value of $\cos \alpha = 0.68$ over the duration of impact. Furthermore, the mean value of $\sin(\alpha + \beta_B) = 0.64$ and thus both angle dependent terms are of order 1. For threshold skipping cases, we expect the characteristic acceleration $2R/t_c^2$ to be small compared to gravity (see Methods) and thus predict $3U_{\min}^2 \lambda_{\max}^2 / 8\pi R \rho^* \approx g$, which gives $U_{\min} \approx \sqrt{8\pi g \rho^* R / 3\lambda_{\max}^2}$. Using the typical values from the simulation case, for which $\lambda_{\max} = 1.44$, gives $U_{\min} = 1.04$ m s⁻¹, which is on the same order as the actual impact velocity used to generate the simulation, $U_o = 2.71$ m s⁻¹.

We now consider typical values of the terms in equation 3.63 for skipping events in which $t_c \approx t_w$. We consider a representative experiment with $R = 26.2$ mm, $G = 12.3$ kPa, $\rho^* = 0.937$, $U_o = 13.2$ m s⁻¹ and $\beta_o = 24.2^\circ$ that results in skipping with measured $t_c = 15$ ms and $t_w = 24$ ms. Simulation with our analytical model using these same parameters reveals a mean value of $\sin(\alpha + \beta_B) \cos \alpha \approx 0.4$ and $\lambda_{\max} \approx 1.5$. Thus $1/\sqrt{\sin(\alpha + \beta_B) \cos \alpha} \approx 1$ and based on the scaling analysis (see Methods section), we expect $t_c \approx \frac{R}{U_o \lambda_{\max}} \sqrt{\frac{16\pi \rho^*}{3}}$. Inserting the experimental values into this expression gives $t_c \approx 8$ ms, which is comparable to the actual measured collision time of $t_c = 15$ ms. Thus, the scaling for the collision time is $t_c \propto (R/U_o \lambda_{\max}) \sqrt{\rho^*}$. Combining this with the wave time scaling, $t_w \propto R/\sqrt{G/\rho_s}$ (see figure 10), gives the expected dependence of the timescale ratio,

$$\frac{t_c}{t_w} \propto \left(\frac{G}{\rho_w U_o^2} \right)^{1/2} \frac{1}{\lambda_{\max}} \quad (3.64)$$

In the shallow β_o limit, $t_c/t_w \approx 1$ occurs at values of $G/\rho_w U_o^2 > 0.1$. For example, for $\beta_o = 11.5^\circ$, $t_c/t_w = 1$ occurs at $G/\rho_w U_o^2 = 0.24$ (see figure 5) and for shallower impact angles we expect this critical value of $G/\rho_w U_o^2$ to continue to increase. As $G/\rho_w U_o^2$ increases, we expect $\lambda_{\max} \rightarrow 1$ (figure 3(c)) and thus anticipate $t_c/t_w \propto (G/\rho_w U_o^2)^{1/2}$ for shallow angles. For steeper values of β_o (e.g., $\beta_o > 34.5^\circ$), our simulations indicate a limiting dependence of $\lambda_{\max} \propto (G/\rho_w U_o^2)^{-5/12}$ for critical values of $G/\rho_w U_o^2$ for which $t_c/t_w = 1$ (figure 3(c), figure 5). Therefore, in the steep β_o limit we expect $t_c/t_w \propto (G/\rho_w U_o^2)^{11/12}$.

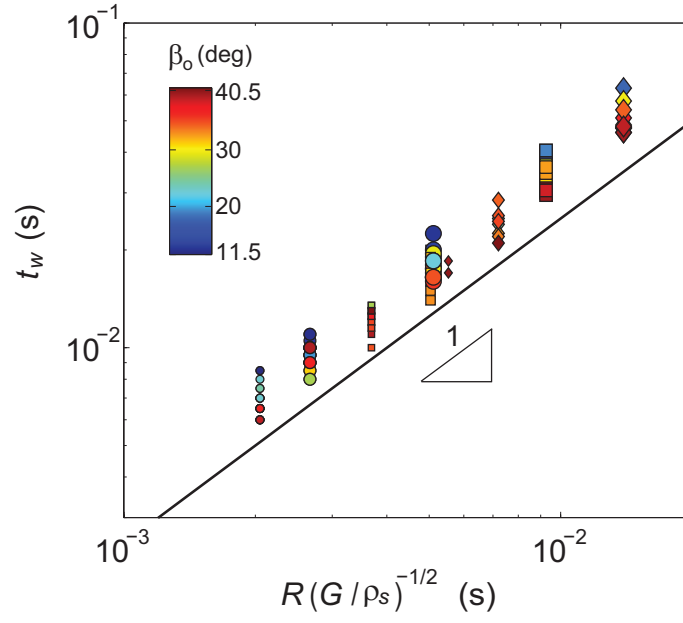


Fig. 3.10: The wave time is linked to the rate of change of attack angle. Our analytical model predicts that the mode 1^- elastic wave regulates $\dot{\alpha}$, which leads to the expectation that $t_w \propto R/\sqrt{G/\rho_s}$. This is confirmed experimentally over a range of R , G and β_o (marker shapes and sizes same as for Fig. 5). The data plotted encompass all experimental impacts characterized by the propagation of a mode 1^- type wave, including mode 1^- skipping, transitional and water entry events. Therefore, the data shown capture a range of U_o and the relatively small spread for a given set of sphere properties indicates that impact speed has a small effect on t_w .

3.8 Supplement 3: Small stiffness limit in which surface tension is important.

We now estimate the value of shear modulus at which surface tension forces have a non-negligible effect on deformation by considering an elastic sphere impacting normal to the surface ($\beta_o = 90^\circ$, see figure 11). First, we expect surface tension to be important to the overall dynamics of sphere impact (rigid or elastic) when the Weber number is of order one, $We = \rho_w U_o^2 R / \sigma_w \approx 1$. We assume symmetry in the sphere deformation such that $\lambda_1 = \lambda_3 = \lambda$ and $\lambda_2 = 1/\lambda^2$. The components of the differential force from surface tension are $dF_{c_1} = \sigma_w \cos \psi (\lambda R d\phi) \cos \phi$, $dF_{c_2} = \sigma_w \sin \psi (\lambda R d\phi)$ and $dF_{c_3} = \sigma_w \cos \psi (\lambda R d\phi) \sin \phi$, where $\psi = \theta_c - \pi/2$ and θ_c is the cavity cone angle [1]. In the limit of $G \rightarrow 0$, we expect the period of sphere vibrations $t_w \rightarrow \infty$ such that $\ddot{\lambda}$ and $\dot{\lambda}$ are negligible. Considering equation 3.45 with all time derivatives set to zero gives

$$\frac{4\pi}{3} GR^3 \left(\frac{1}{\lambda^2} - \lambda^4 \right) = \int_A (t_2 \lambda^2 (y_2 - d_2) - t_3 \lambda^2 (y_3 - d_3)) dA \quad (3.65)$$

For a first order analysis, we assume the surface tension force acts at $y_2 - d_2 = 0$, which gives

$$\frac{4\pi}{3} GR^3 \left(\lambda^4 - \frac{1}{\lambda^2} \right) = \sigma_w \cos \theta \lambda^3 R^2 \int_0^{2\pi} \sin^2 \phi d\phi \quad (3.66)$$

Solving equation 3.66 and rearranging gives

$$\lambda - \frac{1}{\lambda^5} = \frac{3\sigma_w \cos \theta}{4GR} \quad (3.67)$$

For the left-hand side of equation 3.67 to be non-zero requires $\sigma_w / GR \approx 1$, which gives $G \approx \sigma_w / R$.

3.9 Acknowledgements

J.B., T.T.T. and R.C.H. acknowledge funding from the Office of Naval Research, Navy Undersea Research Program (grant N0001414WX00811), monitored by Ms. Maria Medeiros. J.B. and M.A.J. acknowledge funding from the Naval Undersea Warfare Center

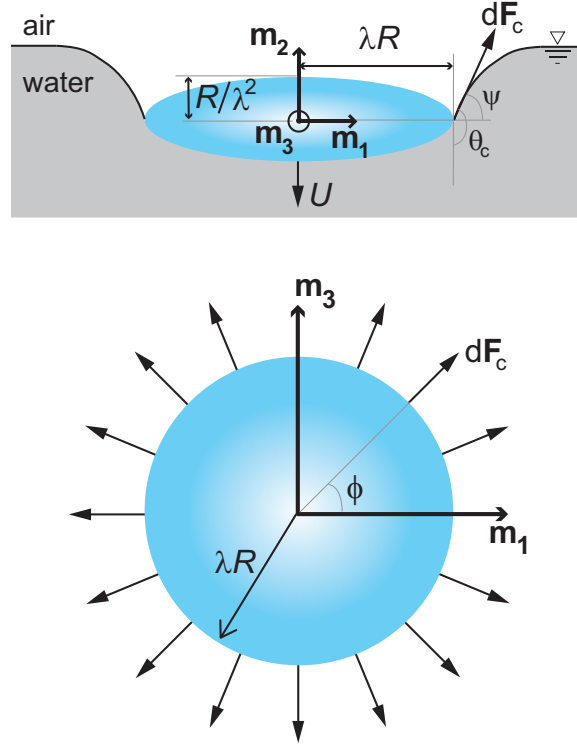


Fig. 3.11: Limiting case when surface tension becomes important. In the limit of $G \rightarrow 0$, and for impacts where the Weber number is of order one ($We = \rho_w U_o^2 R / \sigma_w \approx 1$), we expect surface tension at the air-water interface to affect the sphere deformation. This simplified model shows an elastic sphere impacting normal to the air-water interface. The differential force from surface tension is dF_c and $\psi = \theta_c - \pi/2$, where θ_c is the cavity cone angle. A first order force balance using our analytical model for sphere deformation leads to the expectation that surface tension effects become relevant when $G \approx \sigma_w / R$ (see Supplement 3 for more details).

In-House Lab Independent Research program, monitored by Mr. Neil Dubois. We thank J.Bird, N. Dubois, A. Hellum, J. Marston, B. Roden and S. Thoroddsen for reading and commenting on the manuscript and C.Mabey for his photography.

REFERENCES

- [1] J. M. Aristoff and J. W. M. Bush. Water entry of small hydrophobic spheres. *J. Fluid Mech.*, 619:45–78, 2009.
- [2] G. Birkhoff, G.D. Birkhoff, W.E. Bleick, E.H. Handler, F.D. Murnaghan, and T.L. Smith. Ricochet off water. *AMP Memo*, 42, 1944.
- [3] L. Bocquet. The physics of stone skipping. *American journal of physics*, 71(2):150–155, 2003.
- [4] A. F. Bower. *Applied Mechanics of Solids*. CRC Press, 2009.
- [5] J. W. M. Bush and D. L. Hu. Walking on water: biolocomotion at the interface. *Annu. Rev. Fluid Mech.*, 38:339–369, 2006.
- [6] C. Clanet, F. Hersen, and L. Bocquet. Secrets of successful stone-skipping. *Nature*, 427(6969):29–29, 2004.
- [7] E. de Jonquières. Sur le ricochet des projectiles sphériques a la surface de l’eau. *C.R. [Comptes Rendus des Séances de l’Académie des Sciences. Paris]*, 97:1278–1281, 1883.
- [8] H. Douglas. *A treatise on naval gunnery*. J. Murray, 1860.
- [9] O. M. Faltinsen. Hydroelastic slamming. *Journal of Marine Science and Technology*, 5(2):49–65, 2000.
- [10] S. Floyd, T. Keegan, J. Palmisano, and M. Sitti. A novel water running robot inspired by basilisk lizards. In *Intelligent Robots and Systems, 2006 IEEE/RSJ International Conference on*, pages 5430–5436. IEEE, 2006.
- [11] T. Gilet and J. W. M. Bush. Droplets bouncing on a wet, inclined surface. *Physics of Fluids*, 24(12):122103, 2012.

- [12] J. W. Glasheen and T. A. McMahon. A hydrodynamic model of locomotion in the basilisk lizard. *Nature*, 380(6572):340–342, 1996.
- [13] P. Halswell, P. A. Wilson, D. J. Taunton, and S. Austen. Hydroelastic inflatable boats: relevant literature and new design considerations. *The International Journal of Small Craft Technology*, 2012.
- [14] I. J. Hewitt, N. J. Balmforth, and J. N. McElwaine. Continual skipping on water. *Journal of Fluid Mechanics*, 669:328–353, 2011.
- [15] P. D. Hicks and F. T. Smith. Skimming impacts and rebounds on shallow liquid layers. In *Proceedings of the Royal Society of London A: Mathematical, Physical and Engineering Sciences*, volume 467, pages 653–674. The Royal Society, 2011.
- [16] R. Hurd, T. Fanning, Z. Pan, C. Mabey, K. Bodily, K. Hacking, N. Speirs, and T. Truscott. Matryoshka cavity. *Phys. Fluids*, 27(091104), 2015.
- [17] M. A. Jandron, R. C. Hurd, J. L. Belden, A. F. Bower, W. Fennell, and T. T. Truscott. Modeling of hyperelastic water-skipping spheres using abaqus/explicit. SIMULIA Community Conference, May 2014.
- [18] W. Johnson. Ricochet of non-spinning projectiles, mainly from water part i: Some historical contributions. *International journal of impact engineering*, 21(1-2):15–24, 1998.
- [19] W. Johnson. The ricochet of spinning and non-spinning spherical projectiles, mainly from water. part ii: An outline of theory and warlike applications. *International journal of impact engineering*, 21(1-2):25–34, 1998.
- [20] W. Johnson and S. R. Reid. Ricochet of spheres off water. *Journal of Mechanical Engineering Science*, 17(2):71–81, 1975.
- [21] A. Korobkin, E. I. Parau, and J. M. Vanden-Broeck. The mathematical challenges and modelling of hydroelasticity. *Phil. Trans. R. Soc. A*, 369:2803–2812, 2011.

- [22] A. Korobkin and V. Pukhnachov. Initial stage of water impact. *Annual review of fluid mechanics*, 20(1):159–185, 1988.
- [23] K. Liu and F. T. Smith. Collisions, rebounds and skimming. *Phil. Trans. R. Soc. A*, 372(2020):20130351, 2014.
- [24] T. Miloh. On the oblique water-entry problem of a rigid sphere. *Journal of Engineering Mathematics*, 25(1):77–92, 1991.
- [25] S. Nagahiro and Y. Hayakawa. Theoretical and numerical approach to “magic angle” of stone skipping. *Physical review letters*, 94(17):174501, 2005.
- [26] D. Richard and D. Quéré. Bouncing water drops. *EPL (Europhysics Letters)*, 50(6):769, 2000.
- [27] E. G. Richardson. The impact of a solid on a liquid surface. *Proc. Phys. Soc.*, 61:352–367, 1948.
- [28] L. Rosellini, F. Hersen, C. Clanet, and L. Bocquet. Skipping stones. *Journal of Fluid Mechanics*, 543:137–146, 2005.
- [29] T. T. Truscott, B. P. Epps, and J. Belden. Water entry of projectiles. *Annu. Rev. Fluid Mech.*, 46:355–378, 2014.
- [30] J. Von Heland. Water bouncing ball, December 19 2008. US Patent App. 13/140,358.
- [31] T. Von Karman. The impact on seaplane floats during landing. *NANA-TN-321*, 1929.
- [32] P. C. Withers. Aerodynamics and hydrodynamics of the ‘hovering’ flight of wilson’s storm petrel. *Journal of Experimental Biology*, 80(1):83–91, 1979.

CHAPTER 4

WATER WALKING: A NEW MODE OF FREE SURFACE SKIPPING

4.1 Prologue

After gaining insight into the skipping behavior of elastomeric spheres during a single impact event, I investigated this behavior during multi-skip events. This was in part to evaluate whether trends identified for single impact events held for subsequent impacts, but also to see whether the confined laboratory setting had limited my observations. Data were primarily collected during a week long, on-site study at Bear Lake, Utah. Additional skipping events were filmed in a more controlled environment at the Naval Undersea Warfare Center in Newport, Rhode Island. Analysis and modeling occurred at Utah State University and at the Naval Undersea Warfare Center. The study is still in preparation under the title “Water walking: a new mode of free surface skipping.” The authors listed are: Randy C. Hurd, Jesse Belden, Sean Holekamp, Michael A. Jandron, Allan F. Bower and Tadd T. Truscott. The proposed article is presented below.

4.2 Abstract

Deformable elastomeric spheres are evaluated experimentally as they skip multiple times over a lake surface. Some spheres are embedded with a small inertial measurement unit to measure the acceleration experienced on impact. A model for multiple impact events shows good agreement between measured acceleration, number of skipping events and distanced traveled. The experiment reveals a new mode of skipping, “water walking,” which is observed for relatively soft spheres impacting at low impact angles. The mode occurs when the sphere gains significant angular velocity over the first several impacts, causing the sphere to maintain a deformed, oblate and oblong shape. The sphere moves nearly parallel to the water surface with major axis tips dipping below with each rotation

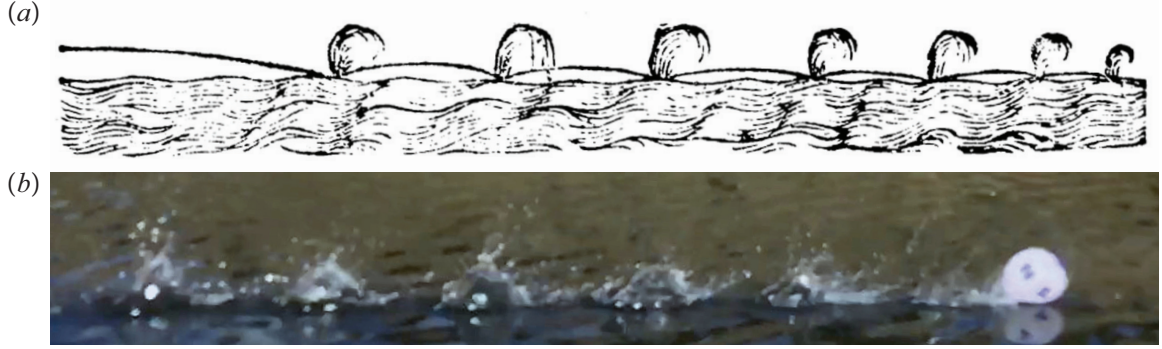


Fig. 4.1: (a) A depiction of a cannonball skipping across the water surface from *The Arte of Shooting in Great Ordnance*, written by master gunner William Bourne in 1587. (b) An elastomeric, silicone rubber sphere skips across the water surface at Bear Lake, UT, exhibiting a newly observed skipping mode, “water walking.”

while the shorter sides pass just above, giving the impression that the sphere is walking across the water surface.

4.3 Background

As early as the late 16th Century, naval gunners knew that a cannonball fired at a sufficiently small impact angle to the water surface could be made to skip across the sea [6]. Figure 4.1(a) displays a 16th century depiction of this phenomenon. The technique simplified targeting because skipping spheres would strike any object along a straight line, rather than only a single point. By the mid 19th century, engineers were investigating how changes in impact angle and sphere density affected the number of skipping events. Notes from experiments collected in 1855 record a 24.5 kg sphere skipping 32 times before entry [9]. In 1883, de Jonquières discussed that a critical impact angle exists above which skipping does not occur, which is inversely proportional to the square root of the sphere specific gravity ($\theta_c = 18/\sqrt{SG}$) [8].

Early efforts to study skipping behavior produced little more than qualitative results [12]. In 1944, photographic techniques allowed Birkhoff *et al.* to perform a more complete study and create a model for the forces experienced by a rigid sphere obliquely impacting a liquid surface [4]. However, Birkhoff’s model is not completely analytical. Other researchers, as well as Birkhoff himself, have noted that more than one assumption in the model are not

necessarily true, but provide a good estimate of the forces involved [12]. Johnson mentions that, “the phenomenon of ricochet [on water] is well known but not widely understood because it takes place in circumstances difficult to control and define... It is a succession of oblique high speed impact events... in which the geometry of each individual strike is different.” Perhaps for this reason, most studies concerning skipping phenomenon focus on single impacts rather than the complete skipping event [12] .

More recently, skipping behavior has been studied in reference to skipping stones. In 2003, Bocquet presented a model for stone skipping which he used to theoretically estimate the maximum number of skips that can be achieved with a skipping stone [5]. Clanet *et al.* published an experimental investigation in 2004 which shows optimal values for both impact angle and attack angle [7]. The model for stone skipping was refined further in light of experimental results by Rosellini *et al.* [14]. In 2005, Nagahiro and Hayakawa performed a three-dimensional simulation of stone skipping which produced results in agreement with those discovered by Clanet *et al.* [13].

Hewitt *et al.* studied subsequent water skipping events, more specifically a fixed plane skipping on a moving channel [11]. The authors identified multiple skipping states or modes and present several models to explain their qualitative features. While the governing principles are similar, the study by Hewitt *et al.* differs significantly from an investigation of elastomeric spheres skipping on a fixed liquid pool, which is presented here.

Deformable skipping spheres were first studied in 2011 when Truscott *et al.* investigated a water skipping toy known as a Waboba® [15]. They noted that deformation upon impact appears to increase lift and thus produce more successful skipping. Following publications by the same research group have provided additional insight into why elastomeric spheres skip more readily than their rigid counterparts [3], [2]. Deformation upon impact not only increases cross-sectional area, resulting in greater lift, but also produces more favorable attack angles with the water surface.

This paper presents an investigation of the skipping behavior of elastomeric spheres over successive skipping events. The measured results are compared to multi-skip events

predicted by single skip models applied back to back. These models show good agreement for traditional skipping events. Additionally, experimental investigations revealed a previously unknown mode of water surface skipping for elastomeric spheres. The new skipping mode consists of the sphere moving nearly parallel to the water surface while impacting the water rapidly; this gives the impression that the sphere is walking across the water surface (see figure 4.1(b)). We investigate the causes and behavior of this newly observed phenomenon.

4.4 Methods

We investigated the water skipping characteristics of deformable elastic spheres by creating multi-skip events on a lake surface (Bear Lake, UT, USA). Data were only collected during the early morning or early evening hours when the lake was smooth and waves were minimal (see figure 4.3). We varied sphere impact velocity U_0 , impact angle β_0 , diameter D and material shear modulus G . Spheres were made from a platinum-cure silicone rubber called Dragon Skin®, produced by Smooth-On, Inc. Sphere shear modulus G was altered by adding a silicone thinner to the mixture to produce three values ($G = 12.3, 28.5$ & 74.7 kPa) with a density of $\rho_s = 1070$ kg/m³. The ingredients were measured by mass ratio, then mixed and placed into a vacuum chamber to remove entrained air. The resulting mixtures were poured into aluminum molds to form spheres of two diameters ($R = 25.5$ & 50 mm). Prior research shows that these spheres can be reasonably modeled as neo-Hookean solids [2].

Spheres were launched from a pneumatic cannon at the water surface to initiate skipping, as shown in figure 4.2. Air pressure was varied to control U_0 and the barrel angle was adjusted to alter β_0 . Impact conditions were filmed using a Photron SA3 high speed camera filming at 1000 fps. Downrange footage was captured using several different cameras (Photron SA3, Sony 7r, GoPro and iPhone). This experimental setup on the lakeside is shown in figure 4.2. A six-axis ± 200 g accelerometer was embedded within some of the larger spheres ($R = 50$ mm) to measure acceleration during skipping. The number of times a sphere skips before entry is indicated by N , and was measured from high speed video. The distance from the cannon barrel tip to entry is denoted by d , and was measured by eye

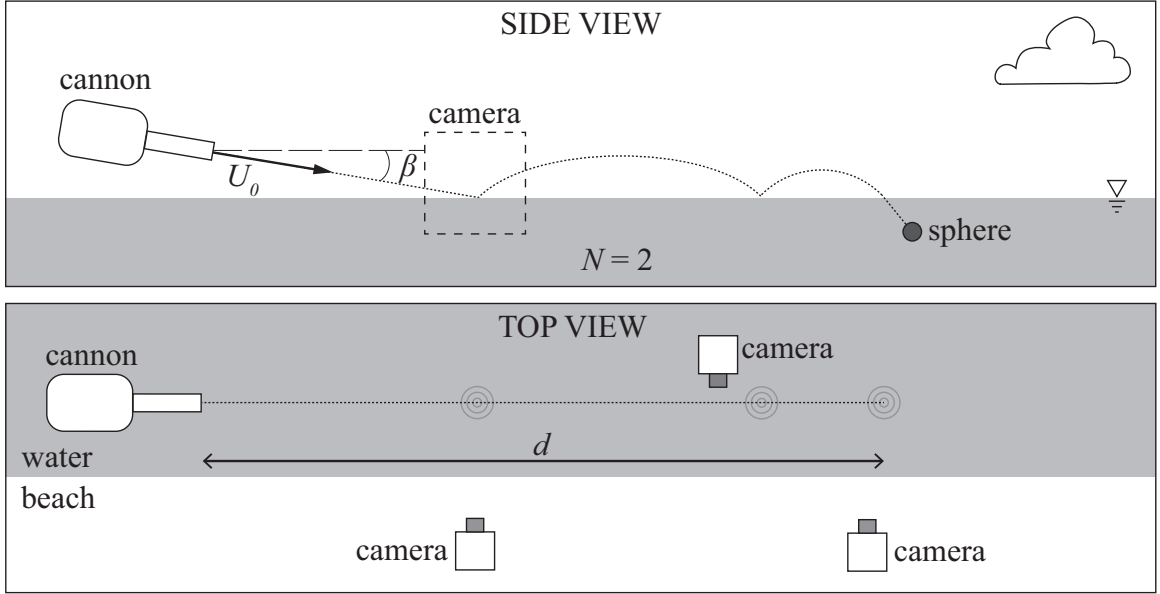


Fig. 4.2: Experimental spheres of radius R and shear modulus G were propelled from a pneumatic air cannon toward a lake surface. The cannon allowed for adjustment to impact velocity U_0 and impact angle β_0 . The initial impact event was filmed with a high speed camera, while subsequent impact events were filmed with cameras and high speed cameras. The total distance travelled before entry is represented by d and N represents the number of skips before entry.

in reference to markers along the shore.

Additional experiments were conducted in a $0.9 \times 1.2 \times 27.4$ m tank. The skipping events were filmed with a Phantom v310 high speed camera using diffuse backlighting.

4.5 Results

4.5.1 Multiple skip phenomena

A deformable elastomeric sphere impacting a water surface at an oblique angle will, under certain conditions, rebound or skip from the water surface. When this event happens on a large body of water, the rebounding sphere follows a predictable projectile trajectory before impacting the water a second time [2]. Depending on the initial impact conditions the sphere can skip once, twice, or several times before losing the energy necessary to skip and (for spheres denser than water such as these) entering the water. The height and

distance achieved between skips decreases with each skipping event, just like a skipping stone, with the last few skips before entry typically occurring rapidly with spacing near one sphere diameter. These rapid impacts just prior to entry are known as “pitty-pat” in the stone skipping community. A photographic example of this type of traditional skipping for elastomeric spheres is presented in figure 4.3(a). A representative trajectory of traditional skipping is presented in figure 4.3(c).

In addition to the skipping behavior described above, skipping experiments at the lake soon showed that when softer spheres (smaller G) were skipped with lower values of the angle β_0 , they would quickly transition from traditional skipping behavior (always within 3-4 skips), to moving approximately parallel to the water surface with impact events occurring very close together (on the order of one sphere diameter). This is diagramed in figure 4.3(d). In this mode, the height of skipping events was nearly indiscernible, even from high speed footage. This motion parallel to the water surface with rapid skipping events gave the impression that the sphere was “walking” across the water surface in a manner which brought to mind the water walking basilisk lizard [10]. Photographs of this walking behavior are shown in figure 4.3(b). Upon closer inspection of high speed photographs, we observed that spheres exhibiting this behavior exhibited high angular velocity $\dot{\psi}$ and generally maintained a more pronounced deformed shape during the skipping event (visible in figure 4.3(b)). This deformation is represented by the parameter λ , shown in the inset of figure 4.3(d).

We investigate the differences between this “water walking” behavior and traditional skipping through high speed photographs collected in a more controlled lab setting. Consider the traditional skipping event in shown figure 4.4(a); the ball impacts at a shallow oblique angle, creates a single cavity, then rises above the water surface. The centroid of the sphere image (black diamond) is clearly descending before impact and ascending after impact. The cavity created by this impact sequence is shown in Figure 4.4(b). By contrast, the sphere in figure 4.4(c) exhibits water walking. The sphere maintains a more pronounced deformed shape and impact events appear not to come from the sphere descending into the

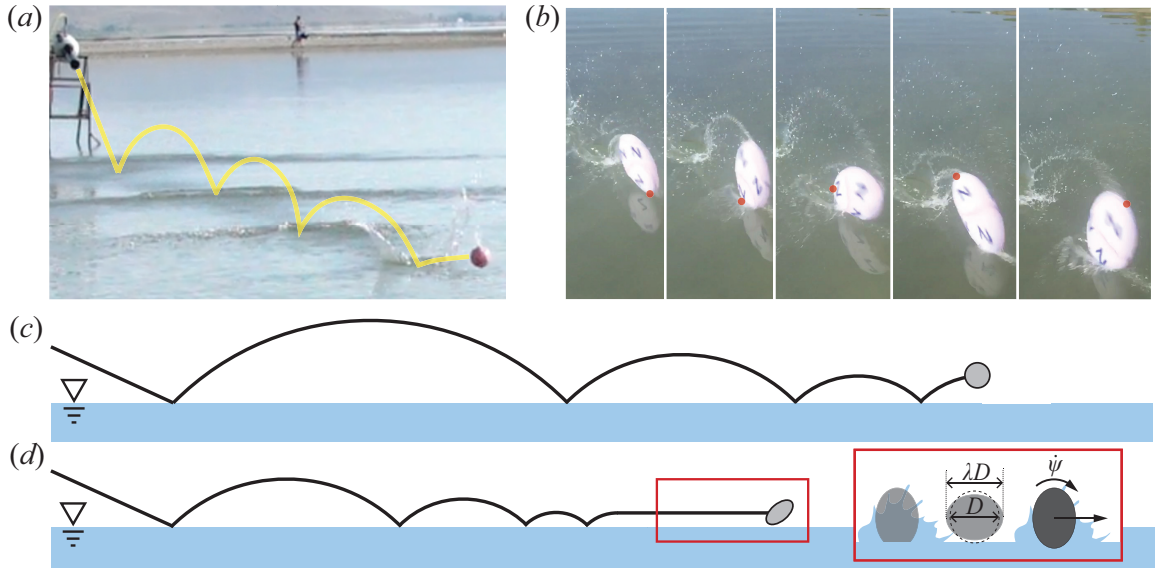


Fig. 4.3: (a) An elastomeric sphere skips from the water surface several times in a traditional manner with the distance between skips decreasing significantly with each impact event; a yellow line traces the sphere trajectory. (b) An elastomeric sphere exhibits the “water walking” skipping mode. A red dot identifies the same point throughout the image sequence (4 ms between images). The sphere rotates at high speeds, maintaining a deformed shape, with only the tips of the major axis of the deformed spheroid dipping below the surface. (c) A side view of a characteristic trajectory for a traditional skipping event. (d) A side view of a characteristic trajectory for a water walking skipping event. Sphere deformation due to angular velocity $\dot{\psi}$ is indicated by the parameter λ , which is experimentally measured from the major axis.

water, but due to the tips of the major axis of the prolate spheroid rotating to interact with the water surface (d). This impact event doesn't generate enough lift to cause the ball to ascend significantly, but generates sufficient lift to prevent the sphere from descending below the water surface (note the relatively constant height of the centroid). In extreme cases this behavior can persist for more than 100 surface impact events.

4.5.2 Modeling multiple skip events

This newly observed skipping behavior and traditional skipping events are investigated in light of the hydrodynamic force model proposed by Belden *et al.* [2]. Consider an elastomeric sphere impacting the water surface as shown in figure 4.5. The magnitude and direction of sphere velocity are represented by U and β , with subscripts referring to those values upon impact (0), at the sphere bottom during impact (B) and upon exiting the water (E). Changes in the sphere radius R during impact are represented by the scalars λ_1 and λ_2 . The coordinates of the sphere centroid are (d_1, d_2) and the attack angle is represented by α .

Belden *et al.* proposed an analytical model where the sphere is idealized as an incompressible neo-Hookean hyperelastic solid with shear modulus G and density ρ_s . They altered an existing model proposed by Rosellini *et al.* for circular disks and approximated the wetted area as a circular disk with radius $\lambda_{eq}R$, modeling the force as

$$F = \frac{1}{2}\rho_w|U_B|^2 S_w \sin(\alpha + \beta_B), \quad (4.1)$$

where S_w is the sphere wetted area. Their published results show that this model predicts the skipping behavior of a sphere in terms of impact velocity U_0 and impact angle β_0 over four subsequent skipping events. Their work does not comment on the ability of the model to predict impact force, number of impact events or distance travelled [2].

We present two cases characteristic of observed traditional skipping and water walking, and compare the results with model predictions. For each scenario, experimentally measured impact conditions $U_{0,1}$ and $\beta_{0,1}$ (the second subscript refers to the impact number) are used

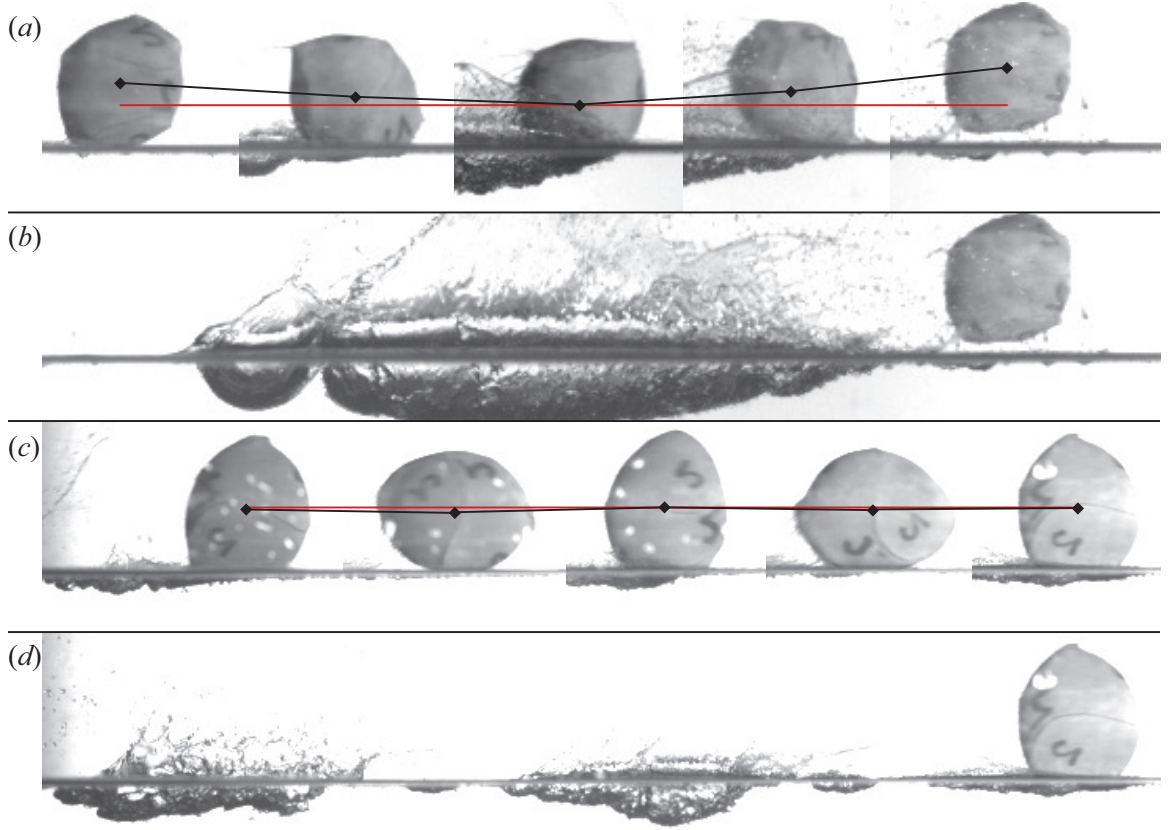


Fig. 4.4: High speed images of two types of skipping events are shown. The skipping events were filmed in a long glass tank using high speed cameras and diffuse backlighting. (a) A traditional skipping event in which the sphere impacts the free surface at an oblique angle and creates a single cavity before rising above the free surface (12 ms between images). The sphere completes one full rigid rotation in the period T , which begins at the first displayed black diamond and ends at the last. The black diamonds mark the sphere centroid through the image sequence. Measurements of angular velocity $\dot{\psi}$ are averaged over one period T . For the event shown in (a), $T = 48$ ms and $\dot{\psi} = 130.9$ rad/s. (b) The cavity formed by the sequence shown in (a) is relatively long and deep. (c) In a water walking type 2 event the sphere centroid moves nearly parallel to the water surface and only the tips of the major axis of the prolate sphere create cavities (6 ms between images, $T = 24$ ms, $\dot{\psi} = 261.8$ rad/s). (d) Only the tips on the major axis of the prolate sphere strike the water surface resulting in two distinct, shallow cavities formed during one rotation period. This type of skipping is referred to as “water walking.”

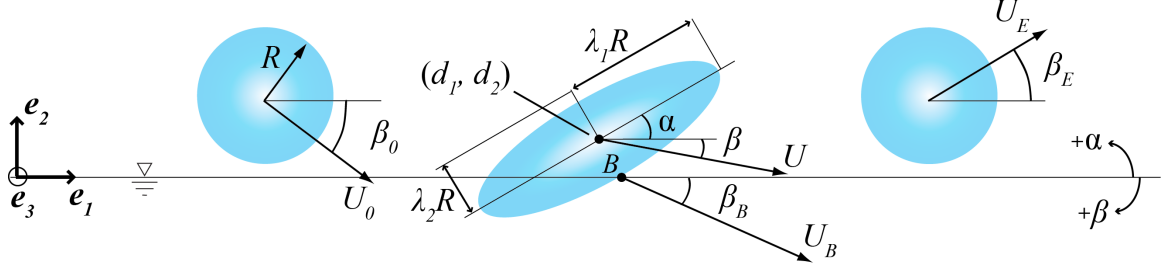


Fig. 4.5: An elastomeric sphere is represented before, during and following impact with a water surface. The sphere radius is represented by R , and λ_1 and λ_2 represent the principal material stretches. The magnitude and direction of sphere velocity are represented by U and β , with subscripts referring to those values upon impact (0), at the sphere bottom during impact (B) and upon exiting the water (E). The location of the sphere centroid is described by (d_1, d_2) and α is the attack angle during impact.

as inputs for the model to calculate exit conditions $U_{E,1}$ and $\beta_{E,1}$. These exit conditions were applied to a ballistic model with simplified air drag to calculate the distance of flight and generate values for $U_{0,2}$ and $\beta_{0,2}$. The process was repeated until the impact angle $\beta_{0,N} < 0.001^\circ$, at which point the impact was deemed an entry. In this way values for U_0 , β_0 and the root-mean-squared acceleration a were modeled for each impact, in addition to predictions for N and d for each complete skipping event.

For the traditional skipping case, a sphere with $R = 0.05$ m, $G = 74.4$ kPa and containing a small 6-axis accelerometer was shot toward the water free surface with impact conditions of $\beta_0 = 10.7^\circ$ and $U_0 = 45.1$ m/s. The sphere skipped in a traditional manner $N = 10$ times and traveled $d = 105$ m before entry. Figure 4.6(a) presents the root-mean-squared acceleration a for this skipping event (gray lines). The measured acceleration peaks initially decrease relatively slowly, then decay more quickly between the final and more rapid impacts of “pitty-pat” prior to entry. The impacts in the middle of the skipping event (highlighted in the plot inset) have a magnitude near $a = 50$ g with well-defined peaks. The peak values of a for a modeled skipping event with the same initial impact conditions are plotted on the same graph (green marks). The timeline for the modeled and experimental data are aligned at the first impact event. For this case, the model significantly over predicts a for the initial impact, but shows good agreement through the sixth impact event, predicting $N = 12$, $d = 83$ m (*measured*: $N = 10$, $d = 105$ m) and also accurately

predicts a “pitty-pat” event prior to entry.

In the water walking case, a sphere with $R = 0.05$ m and $G = 12.3$ kPa, was embedded with a small 6-axis accelerometer and shot toward the water free surface with impact conditions of $\beta_0 = 11.8^\circ$ and $U_0 = 29.2$ m/s. The sphere skipped in a traditional manner three times before the vertical motion of the sphere all but ceased and the sphere traversed nearly parallel to the water surface. During this time the sphere was striking the water so frequently the splash crowns commonly overlapped. The splash events are so intermingled that it is impossible to count the number of impact events visually with confidence. However, individual impact events can be identified via small peaks in the accelerometer data (figure 4.6(b) inset). The experimental sphere was observed to skip $N = 30$ times over a distance of $d = 52$ m. The measured and calculated accelerations are shown in Figure 4.6(b), where we see the peak a values decreasing more quickly than for the skipping case shown in figure 4.6(a). For the first impact event in the traditional skipping case shown in (a), the ratio of impact to exit velocity is $U_E/U_0 = 0.87$, where for the first impact event in the water walking case in (b), $U_E/U_0 = 0.80$. The sphere that exhibits water walking from these two cases is softer than the sphere exhibiting traditional skipping and loses more kinetic energy during this first impact event, most likely because of increased drag due to more pronounced deformation upon impact. This leads to lower acceleration impacts in subsequent skipping events as can be seen in the inset in figure 4.6(b). However, this behavior also seems to enable the sphere to transition to water walking. The peak values of a from a simulated skipping event with the same initial impact conditions for the first skip are plotted on the same graph (black marks). Again the model significantly over predicts a for the initial impact, but shows good agreement through the seventh impact event, predicting $N = 13$ and $d = 24$ m (*measured*: $N = 30$, $d = 52$ m). The model accurately predicts a transition to rapid, low acceleration impact events between 3-4 skips, which enables the transition to water walking. However, the model significantly under-predicts both number of skips N and distance travelled d for water walking.

Research by Belden *et al.* [2] showed that for elastomeric spheres with specific gravity

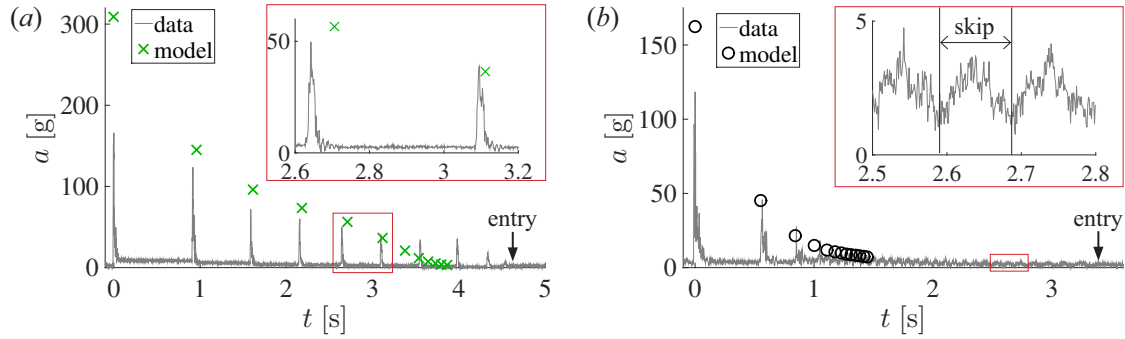


Fig. 4.6: (a) The root mean squared acceleration a is plotted for a traditional skipping event (gray lines). The peak a values from a modeled skipping event with the same initial conditions for the first skip are marked with green \times marks. (b) The root mean square acceleration a is plotted for a water walking skipping event (gray lines). The peak a values from a modeled skipping event with the same impact conditions for the first skip are indicated with black \circ marks. For the first impact event in the traditional skipping case shown in (a), the ratio of impact to exit velocity is $U_E/U_0 = 0.87$, where for the first impact event in the water walking case in (b), $U_E/U_0 = 0.80$. In each of the plots above, the events are aligned in time at the first impact event.

near unity ($SG \approx 1$), skipping or entry can be predicted from two dimensionless parameters: $G/\rho_w U_0^2$ and β_0 . Figure 4.7(a) shows a predictive plot with data from their study. The two simulated skipping events introduced in figure 4.6 are plotted over this regime diagram in figure 4.7(a). The traditional skipping event, plotted with green squares in figure 4.7(a), exhibits behavior similar to the multi-skip event presented by Belden *et al.* [2]. The sphere maintains a relatively constant value of β_0 through the first several impact events until increasing values for $G/\rho_w U_0^2$ (decreasing velocity) bring the sphere into the transitional skipping region (hollow gray triangles). At this point β_0 decreases more rapidly, which eventually leads to entry (highest green square). However, the simulated skip for the water walking case (black squares) exhibits markedly different behavior in light of the regime diagram. Rather than maintaining a relatively constant β_0 over the first few skips, β_0 decreases rapidly over the first 3-4 skips (transition to water walking was always observed to occur within 3-4 skips). The model then predicts several successive impact events with very low values of β_0 , yet small changes in $G/\rho_w U_0^2$ (impact velocity). In other words the model predicts a quick transition to impact events which remain close to the water surface

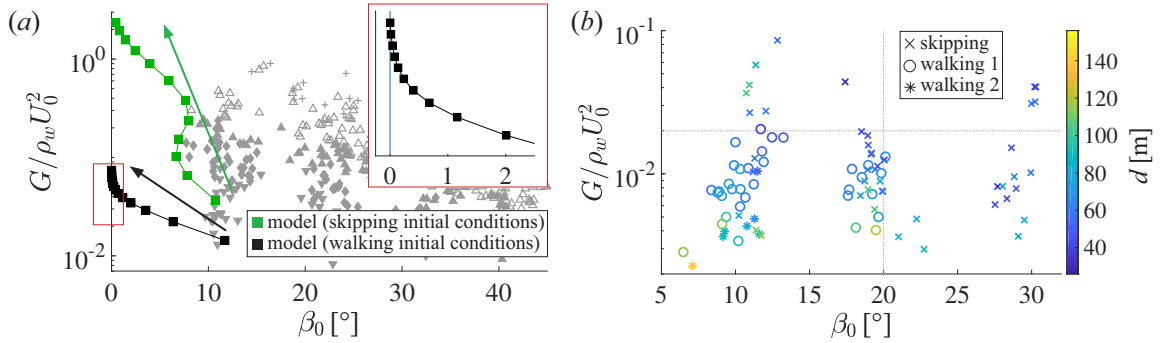


Fig. 4.7: (a) For elastomeric spheres, skipping can be predicted from the dimensionless terms $G/\rho_w U_0^2$ and β_0 . Gray symbols indicate single impact data points from the study of Belden *et al.* [2]. Skips are plotted with solid symbols, while hollow symbols represent a transition to entry and $+$ marks indicate a failed skip (water entry). For the traditional skipping and water walking cases described in figure 4.6, the impact parameters for each impact event are plotted over the diagram. The impact events for the traditional skipping simulation shown in figure 4.6(a) are marked by green squares, with the skipping event progressing in the direction of the green arrow. The impact events for the water walking simulation shown in figure 4.6(b) are marked by black squares. (b) The impact conditions for every multi-skip event analyzed in this study are plotted in the same parameter space. A traditional skip is marked by \times , where water walking skipping events are marked by \circ and $*$ (differentiated in figure 4.9). Water walking was only observed when $G/\rho_w U_0^2 < 0.02$ and $\beta_0 < 20^\circ$, indicated by dotted gray lines. The color of the symbols denotes the distance the sphere traveled before entry d , as indicated by the colored sidebar.

(low impact angles), with minimal change in velocity, characteristics of water walking

Figure 4.7(b) presents all the multi-skip events analyzed for this study. Traditional skipping events are indicated by \times marks where water walking is indicated with \circ and $*$ marks (differentiated later). Note that water walking was only observed when $G/\rho_w U_0^2 < 0.02$ and $\beta_0 < 20^\circ$ (gray dotted lines). The largest values for d were observed when $G/\rho_w U_0^2$ and β_0 were minimized.

4.5.3 Investigating water walking

A primary difference we observed for water walking compared traditional skipping is the presence of significant angular velocity ($\dot{\psi}$). To investigate the role that rotation might play in water walking, we return to the skipping model presented in by Belden *et al.* [2]. They provide a set of equations for the motion of the center of mass and sphere deformation

in terms of general forces and tractions acting on the body. We use an expanded version of the model used by Belden *et al.* to include rigid body rotation. By looking for steady-state solutions with a constant rigid rotation rate $\dot{\psi}$ and all other derivatives and tractions vanishing, we get two equations of motion relating $\dot{\psi}$ to the principal stretches λ_1 and λ_2 , which are

$$\dot{\psi}^2 = \frac{5G}{\rho_s R^2} \left(1 - \frac{\lambda_2}{\lambda_1(\lambda_1 \lambda_2)^3} \right) \quad (4.2)$$

$$\dot{\psi}^2 = \frac{5G}{\rho_s R^2} \left(1 - \frac{\lambda_1}{\lambda_2(\lambda_1 \lambda_2)^3} \right) \quad (4.3)$$

where ρ_s is the sphere density. These equations of motion are only satisfied by solutions in which $\lambda_1 = \lambda_2 \equiv \lambda$, and both expressions simplify to

$$\lambda = \left(\frac{1}{1 - \left(\dot{\psi} / \sqrt{\frac{5G}{\rho_s R^2}} \right)^2} \right)^{\frac{1}{6}}. \quad (4.4)$$

Equation 4.4 thus describes a sphere in steady-state translation and rotation that holds a constant deformed shape described by the principal stretch λ . The expression predicts higher values of lamda λ for larger values of $\dot{\psi}$, ρ_s and R and for smaller values of G . This scaling is plotted as a black line in figure 4.8(b), which predicts an exponential increase in λ as $\dot{\psi} / \sqrt{5G/\rho_s R^2} \rightarrow 1$. This represents a state where the angular velocity $\dot{\psi}$ is equal to the angular material wave speed $\dot{\alpha} = \sqrt{5G/\rho_s R^2}$. Thus, a relatively high value of $\dot{\psi} / \sqrt{5G/\rho_s R^2}$ is necessary to produce the higher values of λ characteristic of water walking, and necessary to produce distinct impact events with sphere rotation. The value of λ is approximated for all experimental cases by measuring the maximum diameter from high speed images. Angular velocity $\dot{\psi}$ is measured from high speed video as near to the middle of the skipping event as possible. These experimentally measured values of λ are plotted against dimensionless angular velocity for all tested cases in figure 4.8(b). Water walking

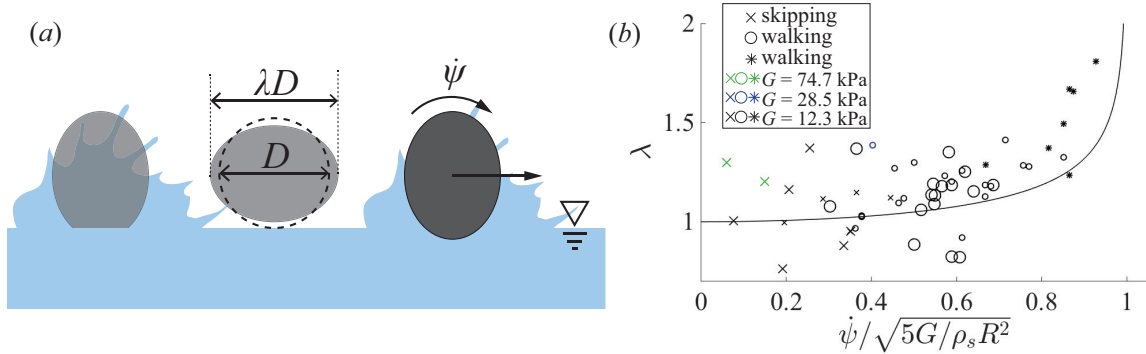


Fig. 4.8: (a) Idealized water walking is diagrammed with indications of the stretch parameter λ and angular velocity $\dot{\psi}$. (b) The stretch parameter λ is plotted against dimensionless angular velocity $\dot{\psi}/\sqrt{5G/\rho_s R^2}$ for all measured multi-skip cases. The derived scaling (black line) predicts that λ increases exponentially with increasing $\dot{\psi}/\sqrt{5G/\rho_s R^2}$. Traditional skipping was not observed when $\dot{\psi}/\sqrt{5G/\rho_s R^2} \gtrsim 0.5$. The transition from type 1 to type 2 water walking (defined in figure 4.9) occurs when $\dot{\psi}/\sqrt{5G/\rho_s R^2} \approx 0.8$.

primarily occurs when $\dot{\psi}/\sqrt{5G/\rho_s R^2} \gtrsim 0.5$.

In figure 4.9(a) we explore the frequency of impact events f as a function of $\dot{\psi}$, looking at only water walking cases. For traditional skipping events, the time between impact events decreased dramatically with each impact and did not correlate with $\dot{\psi}$. Black markers indicate events where skips could be counted visually. Gray markers indicate events where skips were measured from accelerometer data. The observed water walking can be distinguished by one of two slopes, experiencing impact events once or twice per sphere rotation. In figure 4.9(b) a sphere is shown along with the length over which a single rotation occurred (vertical blue lines). Note that only a single cavity was formed; this type of water walking is identified as type 1 water walking. By contrast, the sphere shown in figure 4.9(c) impacts the free surface two times over a single sphere rotation, exhibiting what we will label type 2 water walking. Note that in figure 4.7(b), water walking type 2 only occurs at the smallest values of $G/\rho_w U_0^2$ and β_0 . We also see in figure 4.8(a) that type 2 water walking is only observed for higher values of $\dot{\psi}$.

Finally, we look for any correlations between number of skips N and distance traveled d in figure 4.10(a). There seems to be little correlation, which is supported by qualitative observations. For example, the largest value for distance recorded was $d = 164$ m; though

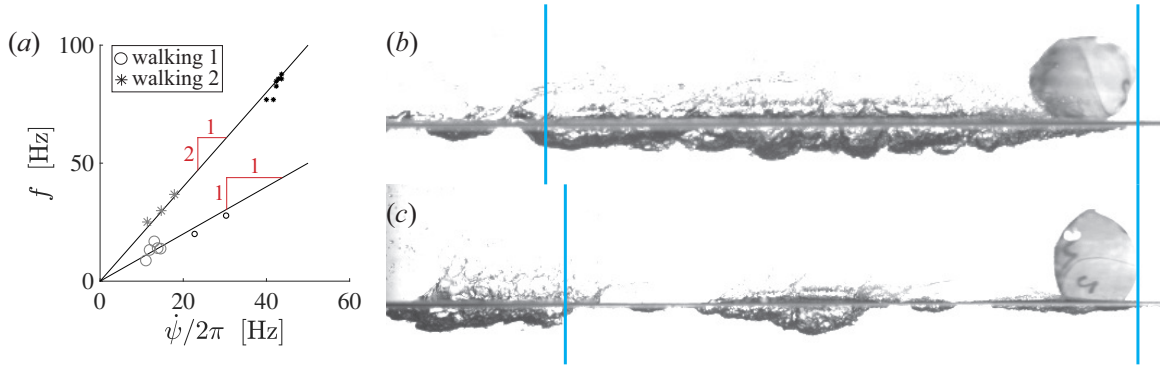


Fig. 4.9: (a) Impact events per second f are plotted against rotations per second $\dot{\psi}/2\pi$. For gray markers, f was measured from accelerometer data, where black markers indicate that f was measured from photographs. All water walking events fall on one of two slopes, indicating 1 or 2 impacts per sphere rotation. Water walking spheres that skip approximately one time per rotation, such as the case shown in (b), are denoted as type 1 water walking. Cases that skip approximately two times per rotation, such as the case shown in (c), are denoted as type 2 water walking. Vertical blue lines indicate the distance over which a single rotation occurred.

this sphere was difficult to see when it landed so far away, and may have skipped an extra time prior to entry, the ball clearly skipped less than 10 times, which is at the low end of N . On the other hand, the event with the greatest number of skips $N = 124$, traveled just under 90 m before entering the water. Even when only considering the traditional skipping events in the figure 4.10(b), there is not an observable trend between N and d . However, one clear conclusion from figure 4.10(a) is that when striving to maximize number of skips N , one should strive for a water walking type 2 skipping event.

4.6 Conclusion

In an effort to extend our knowledge of elastomeric spheres skipping a single time to multi-skip events, spheres of varying sizes and shear moduli G are propelled across a lake surface with a wide range of impact conditions (impact velocity U_0 and impact angle β_0). These skipping events are captured and quantified using high speed cameras and image processing; the results are compared with mathematically modeled multi-skip events. For traditional skipping, the model exhibits accurate estimation of impact velocity U_0 , impact angle β_0 and peak root mean squared acceleration a . The model also provides a reasonable

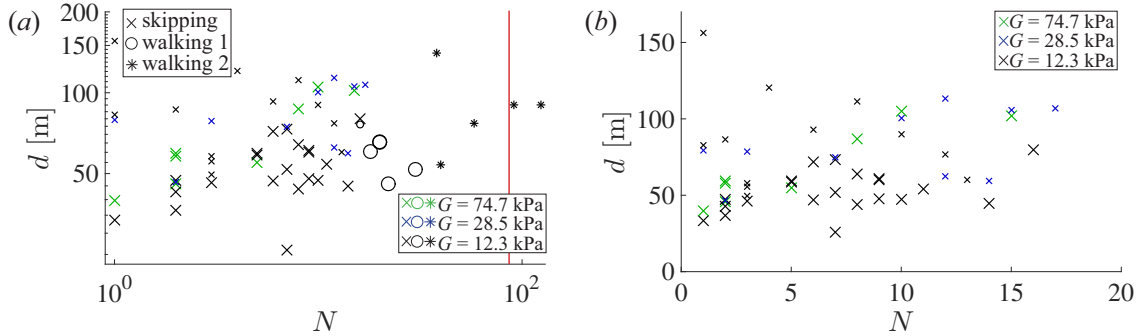


Fig. 4.10: (a) Distance to water entry d is presented as a function of number of skips N for all measured multi-skip events. Water walking events exhibit significantly higher values for N . The vertical red line marks the current world record for stone skipping of 88 skips, set by Kurt Steiner on 6 September 2013 [1]. (b) Distance to water entry d is plotted against N for only traditional skipping events.

prediction for number of skips N and distance travelled d .

This large-scale experimental effort led to the discovery of a new skipping mode for elastomeric spheres labeled “water walking,” which is characterized by a sphere with comparatively high angular velocity $\dot{\psi}$ maintaining a constant deformed disk-like posture. It also involves the sphere moving nearly parallel to the water surface while the tips of the major axis of the spheroid impact the water surface rapidly. Simulated skipping events with the same initial conditions as water walking predict comparable values for a , U_0 and β_0 , but underestimate N and d . However, the model does predict a transition to similar impact events with very low values of β_0 , which is characteristic of the transition to water walking. Water walking appears to require a threshold deformation which can be predicted by the dimensionless angular velocity term $\dot{\psi}/\sqrt{5G/\rho_s R^2}$. Our results show no observed correlation between number of skips N and the distance of the skipping event d . However, water walking events consistently produce values of N that are an order of magnitude higher than traditional skipping events.

4.7 Acknowledgements

R.C.H., J.B. and T.T.T. acknowledge funding from the Office of Naval Research, Navy Undersea Research Program (grant N0001414WX00811), monitored by Ms. Maria

Medeiros. J.B., S.H. and M.A.J. acknowledge funding from the Naval Undersea Warfare Center In-House Lab Independent Research program.

REFERENCES

- [1] *Guinness Book of World Records*. Stamford, CT: Guinness Media, 2017.
- [2] J. Belden, R. C. Hurd, M. A. Jandron, A. F. Bower, and T. T. Truscott. Elastic spheres can walk on water. *Nature Communications*, 7(10551), 2016.
- [3] Jesse Belden, Michael A Jandron, and Tadd T Truscott. Physics of elastic spheres skipping on water. *On the Physics of Sports*, 2013.
- [4] G Birkhoff, GD Birkhoff, WE Bleick, EH Handler, FD Murnaghan, and TL Smith. Ricochet off water. *AMP Memo*, 42, 1944.
- [5] Lydéric Bocquet. The physics of stone skipping. *American journal of physics*, 71(2):150–155, 2003.
- [6] William Bourne. *The Arte of Shooting in Great Ordnance*. Thomas Dawson, 1587.
- [7] Christophe Clanet, Fabien Hersen, and Lydéric Bocquet. Secrets of successful stone-skipping. *Nature*, 427(6969):29–29, 2004.
- [8] de Jonquières. *Acad. Sci., Paris*, 97(1278), 1883.
- [9] Howard Douglas. *A Treatise on Naval Gunnery*. J. Murray, 1855.
- [10] JW Glasheen, TA McMahon, et al. A hydrodynamic model of locomotion in the basilisk lizard. *Nature*, 380(6572):340–342, 1996.
- [11] IJ Hewitt, NJ Balmforth, and JN McElwaine. Continual skipping on water. *Journal of Fluid Mechanics*, 669:328–353, 2011.
- [12] W. Johnson. Ricochet of non-spinning projectiles, mainly from water; part i: Some historical contributions. *Int. J. Impact Eng.*, 21(1-2):15–24, 1998.

- [13] Shin-ichiro Nagahiro and Yoshinori Hayakawa. Theoretical and numerical approach to “magic angle” of stone skipping. *Physical review letters*, 94(17):174501, 2005.
- [14] Lionel Rosellini, Fabien Hersen, Christophe Clanet, and Lydéric Bocquet. Skipping stones. *Journal of Fluid Mechanics*, 543:137–146, 2005.
- [15] Tadd T Truscott, Michael M Wright, Ken R Langley, and Jesse Belden. Holy balls! balls that walk on water. *Physics of Fluids (1994-present)*, 24(9):091103, 2012.

CHAPTER 5

CONCLUSIONS

This dissertation investigates the ability of deformable elastomeric spheres to skip readily upon the water surface. This work is performed in light of the contributions from previous researchers whose findings provide insight into the skipping behavior of rigid spheres and disks. Investigation of this phenomenon is primarily experimental, with some accompanying analytical and numerical analysis. The purpose of this research was to gain an advanced understanding of the skipping dynamics and water entry characteristics of highly deformable elastomeric spheres. The primary **research objectives** were:

1. Understand the water entry characteristics of elastomeric bodies.
2. Investigate how elasticity affects object-water energy transfer.
3. Understand the physics of the water surface skipping of elastomeric bodies.
4. Define optimal material properties and impact conditions for skipping.
5. Understand how these principles transfer to successive skipping events.

In this chapter I will discuss how my research efforts described in Chapters 2, 3 and 4 have satisfied the research objectives (RO) described.

The free surface impact of deformable elastic spheres is first studied in the simplest sense, namely, perpendicular impact and entry (Chapter 2). Experimental data show that elastomeric spheres deform into an oblate shape upon impact, resulting in subsurface cavities that are wider and more shallow than those created by rigid spheres (RO1). After impact and deformation, elastomeric spheres oscillate between oblate and prolate shapes during water entry. The extent of the deformation experienced by the sphere upon impact can be predicted from a viscoelastic material model, though the model under predicts the deformation period, due to the added mass from the surrounding water. However, when

this deformation period is adjusted according to experimentally observed scaling, the model shows very good agreement with experimental results (RO2).

Water entry events are traditionally characterized by cavity characteristics, including the time to cavity pinch off. While non-dimensionalized pinch-off time scales with the dimensionless Froude number for water entry events, this trend did not hold for elastomeric spheres. However, when this scaling was adjusted to represent sphere deformation the experimentally measured results produce a convincing data collapse (RO1).

Elastomeric spheres were observed to lose velocity more quickly than rigid spheres during water entry due to an increased cross-sectional area. However, this difference in deceleration was observed to primarily occur over the first deformation period of the elastomeric sphere, and can be accounted for with a scaling law (RO2). Aside from this predictable deviation, elastomeric spheres decelerate similar to rigid spheres. Furthermore, force coefficients from elastomeric spheres entering the water show good agreement with force coefficients for rigid spheres when averaged over a single deformation cycle (RO1). When the aforementioned differences are accounted for according to the scalings noted, elastomeric spheres behave remarkably similar to rigid spheres (RO1).

I first investigated the skipping characteristics of deformable elastomeric spheres by analyzing a single impact event where a sphere strikes the water at an oblique impact angle (Chapter 3). In an oblique impact event, elastomeric spheres deform producing an increased cross-sectional area. The impacting face also effectively flattens, resulting in an effective attack angle, which is not present with a spherical shape (RO3). The impact event and resulting deformation produce a material wave in the sphere which can assume one of three observed modes, characterized by their material waves (RO3). When material waves interact with the cavity created upon impact, skipping efficiency is compromised (RO2).

The skipping of elastomeric spheres can be described using a model for rigid disk skipping if the sphere is modeled as a disk with a time varying diameter. The model provides a good estimation of exit conditions from impact conditions and accurately estimates sphere skipping and water entry (RO3). The model also provides insight into why elastomeric

spheres skip under conditions when rigid spheres do not. Spheres with a lower shear modulus skip more readily because of a large cross-sectional area generated at impact, as well as the formation of a favorable impact angle developed from sphere flattening along the wetted surface. Both of these behaviors contribute to increased lift upon impact and allow skipping at lower velocities than is possible for rigid spheres (RO3).

Whether an elastomeric sphere will skip or enter the water can be predicted from two dimensionless parameters; the first is a ratio of shear modulus to the hydrodynamic force at impact, and the second is the projectile impact angle, or the angle between the object trajectory and the water surface. Spheres are more likely to skip when shear modulus and impact angle are small and sphere velocity is large (RO4). These dimensionless terms not only predict successful skipping, but also predict deformation modes. The skip model, coupled with these predictive dimensionless parameters, can be used to successfully predict mode type and water entry for skipping events (RO4).

The findings for elastic sphere skipping are expanded to multiple skip events in the experimental study discussed in Chapter 4. The mathematical model for single impact skipping provides an accurate predictor of impact conditions over multiple skipping events in addition to providing an accurate estimation of the acceleration the sphere experiences upon impact. The model can also be used in series to estimate the distance and number of skips in a multiple-skip event from the impact conditions of the first skip and sphere material properties (RO5).

The study of multiple skip events reveals the existence of a new means of skipping for elastomeric spheres, which was previously unobserved (RO3). Relatively soft spheres impacting the water surface with relatively high impact velocities and low impact angles begin to generate appreciable angular velocity after several impact events. This angular velocity causes the sphere to maintain a deformed shape. The sphere continues to travel nearly parallel to the water surface, with the tips of the major axis of the spheroid dipping below the free surface with each rotation. The sphere appears to “walk” along the water surface with rapid and successive impact events, leading to significantly more impact events

than are observed with traditional multi-skip behavior (RO5).

Experimental results show that sphere angular velocity must be greater than half the angular wave speed in the material for the water walking to occur (RO5). Two types of water walking are observed, which are distinguished by the number of impact events per rotation, and can be predicted from the ratio of angular velocity to the angular wave speed. Higher energy water walking spheres (higher angular velocity), which exhibit two impacts per rotation, were observed to skip significantly more times (nearly an order of magnitude) than traditional skipping events. The maximum number of impact events has been shown to occur when the skipping sphere achieves high energy water walking (RO5). While faster impacts, softer spheres, and lower impact angles have proven to be favorable for single impact skipping, the same is true when seeking to maximize the distance of multi-skip events (RO5).

CURRICULUM VITAE

Randy Craig Hurd

randyhurd@gmail.com

Published journal articles

1. **Hurd, R. C.**, Belden, J., Holekamp, S., Jandron, M. A., Bower, A. F. and Truscott, T. T. Water walking: a new mode of free surface skipping. (in preparation)
2. **Hurd, R. C.**, Speirs, N., Belden, J., Pan, Z., Lovett, B., Robinson, W., Zamora, M., Sharker, S., Mansoor, M., Merritt, A. and Truscott, T. T. Shear joy of watching paint dry. *Physical Review Fluids*, 2, 090503, 2017.
3. Pan, Z., Kiyama, A., Tagawa, Y., Daily, D. J., Thomson, S., **Hurd, R. C.** and Truscott, T. T. Cavitation onset caused by acceleration. *Proceedings of the National Academy of Sciences*, 201702502, 2017.
4. **Hurd, R. C.**, Belden, J., Jandron, M. A., Bower, A. F., Fanning, D. T. and Truscott, T. T. Water entry of deformable spheres. *Journal of Fluid Mechanics*, vol. 824, pp. 912-930, 2017.
5. Belden, J., **Hurd, R. C.**, Jandron, M. A., Fanning, D. T., Bower, A. F. and Truscott, T. T. Elastic spheres can walk on water. *Nature Communications*, 7, 1055, 2016.
6. **Hurd, R. C.**, Fanning, T., Pan, Z., Mabey, C., Bodily, K., Hacking, K., Speirs, N. and Truscott, T. T. Matryoshka cavity. *Physics of Fluids*, 27, 091104, 2015.
7. **Hurd, R. C.**, Hacking, K. S., Damarjian, J. L., Wright, G. A. and Truscott, T. T., Underwater robots surface in Utah. *Technology Engineering Teacher*, 2015.

8. Truscott, T. T., Belden J., and **Hurd, R. C.** Water-skipping stones and spheres. *Physics Today*, 67 (12), 70-71, 2014.
9. Daily, D. J., Pendlebury, J., Langley, K., **Hurd, R. C.**, Thomson, S. and Truscott, T. T. Catastrophic cracking courtesy of quiescent cavitation. *Physics of Fluids*, 26, 091107, 2014.
10. Mazzeo, B. A., Patil, A. N., **Hurd, R. C.**, Klis, J. M., Truscott, T. T. and Guthrie, W. S. Air-coupled impact-echo delamination detection in concrete using spheres of ice for excitation. *Journal of Nondestructive Evaluation (JONE)*, 2013.

Published conference papers

1. **Hurd, R. C.**, Weiss, D. M., Graham, J. J. and Truscott, T. T. Future time perspective and problem-based learning in a senior thermo-fluids engineering lab. *ASEE Rocky Mountain Section Conference*, Provo, UT, Sept. 22-23, 2017.
2. Graham, J. J., **Hurd, R. C.** and Truscott, T. T. Adding a new dimension to a traditional conduction lab. *ASEE Rocky Mountain Section Conference*, Cedar City, UT, Sept. 30-Oct. 1, 2016.
3. Wright, G. A., **Hurd, R. C.**, Hacking, K. S. and Truscott, T. T. A remotely operated vehicle scaffolded activity is increasing student and teacher interest in STEM – a reporting on a three-year study funded by the Office of Naval Research. *122nd Annual Meeting of the American Society of Engineering Education*, Seattle, WA, June 14-17, 2015.
4. Jandron, M. A., **Hurd, R. C.**, Belden, J. C., Bower, A. F., Fennell, W. and Truscott, T. T. Modeling of Hyperelastic Water-Skipping Spheres using Abaqus/Explicit. *2014 SIMULIA Community Conference*.

5. Wright, G. A., **Hurd, R. C.**, Hacking, K. S. and Truscott, T. T. Using ROVs to teach a blended STEM curriculum. *121st Annual Meeting of the American Society of Engineering Education*, Indianapolis, IN, June 15-18, 2014.

Patents

1. **Hurd, R. C.**, Truscott, T. T., Pan, Z. and Merritt, A., Splash prevention apparatus.
Docket number: P16034.0. (provisional)

Awards

1. Milton Van Dyke Award - Gallery of Fluid Motion. **Hurd, R. C.**, Speirs, N., Belden, J., Pan, Z., Lovett, B., Robinson, W., Boyer, M., Sharker, S., Mansoor, M., Merritt, A. and Truscott, T. T. The shear joy of watching paint dry. *69th Annual Meeting of the American Physical Society Division of Fluid Dynamics*, Portland, OR. November 20-22, 2016.
2. Milton Van Dyke Award - Gallery of Fluid Motion. Fanning, T., Mabey, C., Bodily, K., Pan, Z., Hacking, K., **Hurd, R. C.** and Truscott, T. T., Matryoshka cavity. *67th Annual Meeting of the American Physical Society Division of Fluid Dynamics*, San Francisco, CA. November 23-25, 2014.